

Earth frozen orbits: design, injection and stability

Master of Science Thesis

J. Hoogland

December 16, 2015

Delft University of Technology



Cover image: artist impression of JASON-2, one of many satellites in a frozen orbit. (Credit: NASA/JPL)



DELFT UNIVERSITY OF TECHNOLOGY
FACULTY OF AEROSPACE ENGINEERING
CHAIR OF ASTRODYNAMICS AND SPACE MISSIONS

Earth frozen orbits: design, injection and stability

MASTER OF SCIENCE THESIS

IN PARTIAL FULFILLMENT FOR THE MASTER'S DEGREE IN AEROSPACE ENGINEERING

AUTHOR:

Jan Hoogland
1507168
jhoogland1@gmail.com

THESIS COMMITTEE:

prof.dr.ir. P.N.A.M. Visser (chair)
ir. R. Noomen (daily supervisor)
dr.ir. M. Snellen (external member)

December 16, 2015

In memory of Neeltje & Cor

Preface

In front of you lies my thesis entitled ‘Earth frozen orbits: design, injection and stability’, which reports on my M.Sc. research carried out at the Faculty of Aerospace Engineering at the Delft University of Technology. As the title suggests, the research is concerned with so-called ‘frozen orbits’, which are cleverly chosen orbits such that the effects of orbital perturbations are minimized.

Astrodynamics has always been one of my key interests: the motion of satellites, planets, moons, asteroids - all of them bound by mutual gravitational pull and all of them moving with respect to one other - shows some amazingly intricate patterns. Of course, I could not have done this research just by myself - I needed help, and I found help from many people, to who I owe my gratitude.

First of all, I’d like to express my gratitude towards my daily supervisor Ron Noomen. Ron, our meetings have been a pleasure, a weekly recurrence of a well-balanced mixture between fruitful discussions and general chit-chat about daily life. You’ve provided helpful and honest feedback, and you’ve answered and asked many questions, pushing me into the right direction. Remaining in the list of academia, a special thanks goes out to dr. Sofya Spiridonova, for helping me out with part of her algorithm which is used in this thesis.

Then, I’d like to thank my colleagues on the ninth floor for providing a pleasant working atmosphere, and for filling the student room with an atmosphere of healthy discussions on our topics, incomprehensible programming errors, bad jokes and daily life. In that same list a special mention goes towards my ‘chauffeur’ Henry, who facilitated my regular commute to Delft.

Lastly, I’d like to thank those closest to me, starting with my lovely girlfriend - thanks for your support, your love, and for putting up with my temper when I had no idea how to progress. Finally, my parents, who have sparked my interest in science and engineering, and who have allowed me to fully explore that interest - I cannot thank the both of you enough.

Jan Hoogland
Delft, January 12, 2016.

Abstract

A *frozen orbit* is an orbit chosen such that the effect of perturbations on (a combination of) the mean orbital elements is minimized. The concept first appeared in literature in 1978, and was applied that same year to the Seasat mission. This altimetry mission featured strict requirements on the accuracy of the altitude of the satellite above the sea surface. By designing an orbit for which the mean eccentricity and mean argument of periapsis remain static, the satellite's altitude will theoretically be constant, depending only on location of the sub-satellite point.

Classically, the theory behind frozen orbits is only based on the J_2 - and J_3 -term of the spherical harmonics gravity field model and clever manipulation of the Lagrange planetary equations. Through considerable analytical effort, it is possible to include all other zonal gravity field terms into the equation, but this approach is limited to perturbations that can be cast into the form of a disturbing potential. The aim of this thesis is to find a numerical method that overcomes this limit and to use that method to investigate the effects of including third-body gravity, atmospheric drag and solar radiation pressure on the mean orbital elements.

To do this, the frozen orbit problem is formulated as an optimization problem. Use is made of Differential Evolution (DE) and grid searching to simulate many trajectories and to find a set of injection parameters that results in a minimal variation in the mean eccentricity and mean argument of periapsis. The mean elements are reconstructed from the osculating elements by making use of the Eckstein-Ustinov theory and subsequent numerical averaging. In combination with Precise Orbit Determination (POD) data, this reconstruction is used to investigate the variations in the mean orbital elements of ERS-2 and TOPEX/Poseidon.

Subsequently, the numerical method is applied to various orbital dynamics models. When applied to zonal gravity fields, the new method is found to be in good agreement with analytical solutions. The influence of other perturbations on solutions found in zonal models is examined, and it is found that taking these perturbations into account during the optimization process does not lead to significant improvements with respect to the simple zonal case, nor does it lead to significant changes in the found injection conditions. For the assumed satellite characteristics, radiation pressure is found to be the most influential perturbation, causing fluctuations in the mean eccentricity of $\pm 3\%$.

Nomenclature

Latin capitals	Description	SI units
A	Reference surface area	m^2
A_D	Reference surface area (drag)	m^2
$A_{D\ast}$	Reference surface area (radiation pressure)	m^2
C_d	Drag coefficient	-
$C_{n,m}$	Gravity field cosine coefficient	-
C_R	Reflectivity coefficient	-
$F_{l,m,p}$	Kaula's inclination function	-
G	Gravitational constant	$\text{m}^3 \text{kg}^{-1} \text{s}^{-2}$
$G_{l,p,q}$	Kaula's eccentricity function	-
G_2	Parameter in Eckstein-Ustinov equations	-
J_l	Zonal spherical harmonics coefficients	-
$J_{l,m}$	Sectorial & tesseral spherical harmonics coefficients	-
K	Overall weight factor for objective function	-
L_\odot	Total solar luminosity	$\text{kg m}^2 \text{s}^{-3} (\text{W})$
M	Mass of planet/moon	kg
M	Mean anomaly	rad
M_0	Mean anomaly at epoch	rad
N	Number of elements or orbits	-
P	Orbital period	s
P_l	Legendre functions	-
$P_{l,m}$	Associated Legendre polynomials	-
R	Distance between satellite and the Sun	m
R_E	Earth radius	m
$S_{n,m}$	Gravity field sine coefficient	-
$S_{l,m,p,q}$	Kaula's S-function	-
U	Gravitational potential	$\text{kg m}^2 \text{s}^{-2} (\text{J})$
\tilde{V}	Disturbing potential	$\text{kg m}^2 \text{s}^{-2} (\text{J})$
\mathbf{v}	Velocity vector	m s^{-1}

Latin capitals	Description	SI units
$V_{x,y,z}$	Velocity vector components	m s^{-1}
W	Solar constant near Earth	$\text{kg s}^{-3} (\text{W m}^{-2})$
\mathbf{Y}	Satellite state vector	multiple
$\dot{\mathbf{Y}}$	Satellite state vector rate of change	multiple
Latin lowercase	Description	SI units
a	Osculating semi-major axis	m
\bar{a}	Mean semi-major axis	m
a_n	Arbitrary orbital element	-
\mathbf{a}_{3rd}	Third-body gravitational acceleration vector	m s^{-2}
\mathbf{a}_D	Atmospheric drag acceleration vector	m s^{-2}
\mathbf{a}_p	Perturbation acceleration vector	m s^{-2}
c	Speed of light	m s^{-1}
c	Summation index in Kaula's inclination function	-
c_r	Crossover probability	-
d	Summation index in Kaula's eccentricity function	-
e	Osculating eccentricity	-
e	Osculating eccentricity	-
\bar{e}	Mean eccentricity	-
f	Weight coefficient (Differential Evolution)	-
h	Singularity-free (equinoctial) orbital element	-
i	Osculating	rad
\bar{i}	Mean inclination	rad
k	Parameter in Kaula's inclination function	-
k_α	Weight factors of arbitrary orbital element	-
l	Gravity field degree	-
l	Singularity-free (equinoctial) orbital element	-
m	Gravity field order	-
m	Mass of satellite	kg
n	Mean motion	rad s^{-1}
n_0	Mean motion at epoch	rad s^{-1}
p	Parameter in Kaula's inclination function	-
p'	Parameter in Kaula's inclination function	-
q	Parameter in Kaula's eccentricity function	-
r	Radial distance to satellite	m
\mathbf{r}	Position vector to satellite	m
r_a	Radial distance to apocenter	m
r_d	Distance between main body and third body	m
\mathbf{r}_d	Position vector from main body to third body	m
r_p	Radial distance to pericenter	m
r_{sd}	Distance between satellite and third body	m
s	Summation index in Kaula's inclination function	-
\mathbf{r}_{sd}	Position vector from satellite to third body	m
$\ddot{\mathbf{r}}$	Acceleration vector	m s^{-2}

Latin lowercase	Description	SI units
s	Position vector to mass element	m
t	Time	s
t	Summation index in Kaula's inclination function	-
x, y, z	Position vector components	m
Greek	Description	SI units
α	Arbitrary orbital element	multiple
α_{avg}	Averaged arbitrary orbital element	multiple
β	Parameter in Eckstein-Ustinov equations	-
β_0	Parameter in Eckstein-Ustinov equations	-
$\Delta\bar{\alpha}$	Total variation in mean orbital elements α	multiple
θ	True anomaly	rad
θ	Longitude in Earth co-rotating frame	rad
θ_0	True anomaly at epoch	rad
$\theta_{l,m}$	Gravity field model parameter	rad
θ_{GMST}	Gravity field model parameter	rad
λ	Singularity-free (equinoctial) orbital element	-
λ'	Parameter in Eckstein-Ustinov equations	-
μ	Gravitational parameter (GM)	$\text{m}^3 \text{s}^{-2}$
μ_d	Gravitational parameter (GM_d) of third body	$\text{m}^3 \text{s}^{-2}$
ρ	Atmospheric density	kg m^{-3}
φ	Latitude (in Earth co-rotating frame)	rad
ψ_{lmpq}	Kaula's phase angle	rad
ω	Osculating argument of periapsis	rad
$\bar{\omega}$	Mean argument of periapsis	rad
Ω	Osculating right ascension of the ascending node	rad
$\bar{\Omega}$	Mean right ascension of the ascending node	rad

Acronyms

Abbreviation	Description
DE	Differential Evolution
DORIS	Doppler Orbitography and Radio-positioning Integrated by Satellites
EO	Earth Observation
EU	Eckstein-Ustinov
ERS	European Remote-sensing Satellite
ESA	European Space Agency
GPS	Global Positioning System
GS	Grid Search
JD	Julian date
LEO	Low Earth Orbit
LRO	Lunar Reconnaissance Orbiter
MJD	Modified Julian Day
NASA	National Aeronautics and Space Administration
PaGMO	Parallel Global Multi-objective Optimization
POD	Precise Orbit Determination
RK	Runge-Kutta
SFU	Solar Flux Unit
SLR	Satellite Laser Ranging
TOPEX	Topography Experiment
T/P	TOPEX/Poseidon
Tudat	TU Delft Astrodynamics Toolbox
UTC	Universal Time Coordinated

Table of contents

Preface	v
Abstract	vii
Nomenclature	ix
Table of contents	xiii
1 Introduction	1
2 Mission heritage	3
2.1 Seasat	3
2.2 ERS-1 and ERS-2	4
2.3 TOPEX/Poseidon	6
3 Orbital dynamics	9
3.1 Two-body problem	9
Satellite position	10
3.2 Irregular gravity field	11
3.3 Atmospheric drag	14
3.4 Third-body attraction	16
3.5 Radiation pressure	17
3.6 Smaller perturbations	18
4 Frozen orbits	19
4.1 $J_2 - J_3$ analysis	19
4.2 Kaula's potential	21
4.3 Actual satellite behavior	24
ERS-2	24
TOPEX/Poseidon	26
5 Methodology	29
5.1 Numerical integration	30

5.2 Osculating to mean elements	33
5.3 Numerical averaging	36
5.4 Objective function	36
5.5 Optimization	37
5.6 Software	38
6 Verification	41
6.1 Eckstein-Ustinov transformation	41
6.2 Global verification	43
7 Results	47
7.1 Assumptions	47
7.2 Zonal geopotential	49
Up to degree 3	49
Up to degree 10	51
Up to degree 25	53
7.3 Influence of other perturbations	54
Inclusion of other perturbations	57
7.4 Complete set of perturbations	59
8 Conclusions and recommendations	65
8.1 Conclusions	65
8.2 Recommendations	66
Bibliography	69

Introduction

Perhaps the biggest challenge in space engineering is optimizing the design of a satellite mission. At total prices in the range of tens to hundreds of millions of dollars for a stereotype mission, every aspect of a satellite's design, manufacturing, planning and logistics is carefully evaluated. In the last decades, the space industry has had to deal with ever-increasing cost effectiveness of its missions: the world wants more science/functionality per dollar. This opens up room for spending time on optimizing every aspect of a mission. The *frozen orbit* is a typical result of optimizing a mission's outcome, driven by more stringent requirements on science instruments aboard satellites.

A frozen orbit is defined as "*an orbit chosen such that one or more mean orbital element(s) do(es) not (or minimally) change under the influence of orbital perturbations*". Technically, any combination of orbital elements can be used in this definition, but in literature the term almost always refers to an orbit where the eccentricity and the argument of periapsis remain stable, as in this case the altitude of a satellite is a constant depending only on the geographical location of the sub-satellite point. This is an important advantage for Earth Observation missions. [1, 2, 3]

The concept was first proposed for the Seasat mission (1979), an altimeter satellite destined to measure sea level heights. To accommodate the precision of the altimeter, the strategy of freezing the argument of periapsis and eccentricity was brought to life and successfully applied on this mission. [4]. Many more missions were to follow, such as the ERS missions, Envisat and TOPEX/Poseidon, to name the most important ones. [5, 6]

The stability of frozen orbits, the advantage of a constant altitude over the geographical location of the sub-satellite point, and the reduced propellant mass required for orbit maintenance are key players in driving a mission design towards selecting a frozen orbit. But to design one, the secular variations caused by orbital perturbations such as the irregular Earth's gravity field, the gravitational attraction of the Moon and the Sun, solar radiation pressure and atmospheric drag have to be zero. The modeling of all these perturbations is not straightforward, and their effects on the mean orbital elements are diverse, which may lead one to believe that by no means they can be completely nullified in the long run. Indeed, they cannot - but it is possible to get close.

Research

Much work has been done on the topic of frozen orbits, of course starting with the elementary analysis for the Seasat mission. [4] As time progressed, more detailed perturbation models were analyzed and more intricate methods were found to refine the bounds for frozen orbit conditions.

Examples include a higher-order solution for the simple zonal problem [7], the inclusion of higher-degree zonal terms [8], to methods making use of higher-order astrodynamics which are beyond the scope of this work. Almost all efforts limit themselves to Earth's zonal gravitational potential. This work aims at including all relevant perturbations in the search for a frozen orbit and the subsequent analysis of the outcome of this search. In order to achieve this, three goals have been established:

- Providing an analysis on the actual behavior of satellites that fly in a frozen orbit.
- Setting up a numerical method to find frozen orbit conditions in a complex dynamics model including **tesseral** gravitational potentials, **third-body** attraction, aerodynamic **drag** and solar **radiation pressure**.
- Subsequent evaluation of the method by simulating the behavior of satellites inserted into an orbit found by this numerical method.

Structure

Following this short introduction, Chapter 2 aims at providing an overview of relevant characteristics of missions that have flown a frozen orbit. An overview of techniques to model orbital dynamics is then presented in Chapter 3. Next, Chapter 4 deals with analytical efforts on finding frozen orbit conditions, and an analysis on the behavior of satellites in frozen orbits. After this, the methodology behind the devised numerical method to find these conditions is presented in Chapter 5, followed by verification of that methodology in Chapter 6. The newly explained and verified methodology is applied to several orbital dynamics models, and the results can be found in Chapter 7. Concluding remarks and recommendations in Chapter 8.

Mission heritage

Throughout the past decades, many missions have flown in a frozen orbit configuration. Most notable examples, which are discussed in this chapter, include the altimetry mission Seasat (the first to make use of the concept), the European Remote-sensing Satellites ERS-1 and ERS-2, and the US/French TOPEX-Poseidon (T/P) mission. [9, 10, 11] An overview of the mission goals and the orbit design of these missions will be presented in this chapter, together with some basic aspects of other missions that have made use of the concept.

2.1 Seasat

Seasat (or Seasat-A / Seasat-1) was the first satellite specifically designed for oceanographic observations through remote sensing. Developed by NASA/JPL in the early 1970's, Seasat was launched on the 26th of June, 1978, from Vandenberg AFB.



Figure 2.1: Artist impression of Seasat in orbit. [12]

The mission goals were threefold: Seasat was to demonstrate techniques to monitor Earth's ocean-

graphic phenomena, as well as to provide timely oceanographic data to the scientific community, and lastly it was to demonstrate the key features of this full-time space-based ocean monitoring system. Seasat operated in orbit for 110 days, after which the satellite failed due to a major short-circuit in the satellite's electrical systems. Despite the early failure, the mission gathered more oceanographic data than any other land-based mission before. [9]

Seasat was the first satellite to make use of the concept of a frozen orbit. The high accuracy required for the altimetry instruments on the satellite asked for an effective solution to ensure the satellite's altitude to be constant every time it passed over a certain area of Earth. During such a pass, a constant illumination angle is desired for some instruments. In order to achieve this, Seasat was placed in a Sun-synchronous frozen orbit. In a Sun-synchronous orbit, the J_2 -effect is used to maintain a constant orientation of the satellite's orbit with respect to the Sun. Seasat's frozen orbit was designed primarily by making use of the J_2 and J_3 perturbations (Section 4.1), but corrections were made by subsequently investigating the effect of all zonal terms up to order 21, though it is not stated how exactly this was done. This subsequent investigation lead to an initial design value of 0.0008 for the eccentricity. [4] The resulting orbit is given by the following mean orbital elements:

semi-major axis, \bar{a}	7168.3	[km]
eccentricity, \bar{e}	≈ 0.0008	[\cdot]
inclination, \bar{i}	108.0	[degrees]
argument of periapsis, $\bar{\omega}$	90.0	[degrees]
orbital period, P	100.7	[min]
ground track repeat cycle	17.0	[days]

Table 2.1: Mean orbital elements for Seasat-A. [4, 13]

2.2 ERS-1 and ERS-2

The European Remote Sensing satellites (ERS) were the first two Earth observation satellites to be designed and built by ESA. The two satellites were designed to "provide measurements of the Earth's atmosphere, ocean, land and ice, to support Earth science research and to provide monitoring capabilities for climatic and environmental changes, as well as changes in land use". Launched in 1991, ERS-1 operated for nine years before failing in 2000, far exceeding its three-year lifespan. ERS-2, launched in 1995, operated until 2011 despite the fact that all gyroscopes had failed in 2001. Its lifetime was increased several times, as at certain times it was the only satellite in orbit to carry specific instruments. Both satellites have gathered enormous amounts of data, resulting in many scientific publications. [5]



Figure 2.2: Artist impression of ERS-2 in orbit. [14]

The same requirements that shaped the final orbit of Seasat were of effect during the design process of the ERS orbits. The focus of the ERS spacecraft was to observe coastal regions, the oceans and ice-covered regions of the Earth: this implies that global coverage is required. The need for a near-polar (highly inclined) orbit is clear. In addition, the instruments on board ERS (especially the altimeter) asked for a constant altitude over the Earth's reference geoid, as well as a constant local solar time during consecutive passes. The frozen (and at the same time Sun-synchronous) orbit is the ideal candidate. ERS-1 and ERS-2 flew in identical orbits, where ERS-2 was trailing behind at a 32-minute delay. [10] The target orbit for the ERS-2 satellite is specified by the following mean orbital elements:

semi-major axis, \bar{a}	7153.1439	[km]
eccentricity, \bar{e}	≈ 0.001166	[\cdot]
inclination, \bar{i}	98.52146	[degrees]
argument of periapsis, $\bar{\omega}$	90.0	[degrees]
orbital period, P	100.5	[min]
ground track repeat cycle	3 / 35 / 176	[days]

Table 2.2: Mean orbital elements for ERS-2. [13, 15]

Apart from the scientific data, all position data for the ERS satellites have been made publicly available. These position data have been gathered by making use of Doppler tracking and Satellite Laser Ranging (SLR) (Section 4.3) when the satellite was visible above ground stations and have subsequently been processed to achieve orbit solutions with to an accuracy of a few centimeters root-mean-squared in radial direction.

2.3 TOPEX/Poseidon

TOPEX/Poseidon (T/P) was a US/French joint satellite mission, launched by an Ariane-4 from Kourou in August 1992.

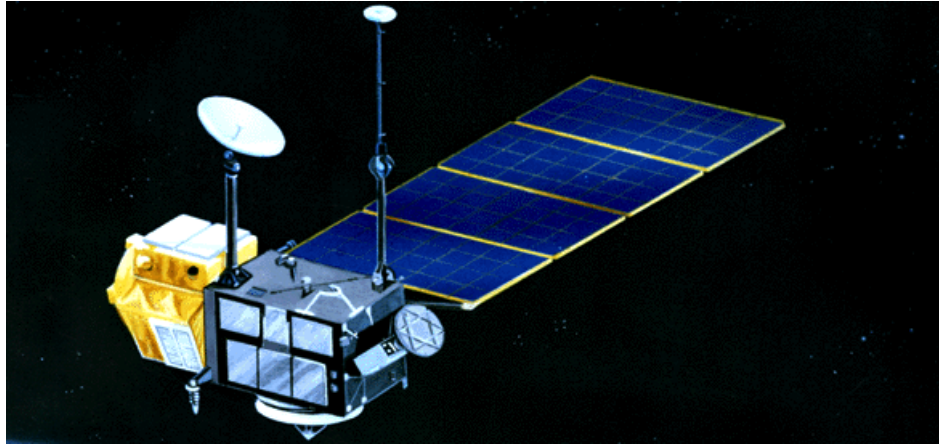


Figure 2.3: Artist impression of TOPEX/Poseidon in orbit. [16]

T/P the overall objective to obtain high-accuracy (compared to ERS) global sea level measurements. Such data are of vital importance in understanding ocean-atmosphere interaction and the prediction of climate change. The satellite was designed for a five-year mission, but it surpassed all expectations by remaining fully functional up until October 2005, when a failed momentum wheel caused the satellite to transmit useless data. Satellite operations ceased in January 2006 after a 14-year long mission. [11]

Unlike Seasat and the ERS satellites, T/P was not intended to provide global coverage - the main focus was on determining sea level height of the unfrozen parts of the oceans. This meant that there was no need to place T/P in a polar orbit; instead, a lower inclination could be chosen, which increases the frequency of observations (no time spent over the poles) and is slightly more favorable in terms of launch cost. Also, the increased accuracy of the instruments aboard T/P allowed for a higher altitude of the satellite, where it is less influenced by gravitational perturbations and atmospheric drag. Because of the altimeter aboard, a constant altitude above the Earth's geoid is favorable, hence the need for a frozen orbit. [6] However, as the inclination of T/P was close to the critical inclination, the stability of the frozen orbit was reduced (shown in Section 4.3), as higher-degree gravity field coefficients start to dominate the long-term orbital motion when the effect of the J_2 term cancels out. T/P's target orbit is specified by the mean orbital elements:

semi-major axis, \bar{a}	7714.43	[km]
eccentricity, \bar{e}	≈ 0.000095	[‐]
inclination, \bar{i}	66.04	[degrees]
argument of periapsis, $\bar{\omega}$	90.0	[degrees]
orbital period, P	112	[min]
ground track repeat cycle	9.9156 (127 revs/cycle)	[days]

Table 2.3: Mean orbital elements for TOPEX/Poseidon. [6]

The unprecedented number of Precise Orbit Determination (POD) instruments on T/P allowed for accurate orbit determination. Position data for the satellite have been gathered using SLR, Doppler Orbitography (DORIS) and Global Positioning System (GPS) observations, and combined with the satellite's own radar altimeter data, the post-processed data has errors in the order of several centimeters root-mean-squared in radial direction. [17, 18]

Other missions

Apart from the three missions discussed in this chapter, many more have flown in a frozen configuration. Some of these missions are the successors to the missions treated in this chapter - Envisat, for example, flies in the same orbit as the ERS satellites and has even carried out a tandem mission together with ERS-2. The successors of T/P, Jason-1 and Jason-2, are also in the same orbit as their predecessor. More recent mission that have flown or are flying in a frozen configuration include:

- Deimos-1, a relatively light (91 kg) Spanish EO satellite, flying in a near-polar frozen orbit at an altitude of roughly 663 km [19]
- Deimos-2, the successor to Deimos-1, flying in a near-polar frozen orbit at an altitude of roughly 620 km [20]
- Sentinel-1, a radar observation satellites in a near-polar frozen orbit at an altitude of roughly 693 km [21]

A more exotic example of a mission that has flown in a frozen configuration is the Lunar Reconnaissance Orbiter (LRO), which was inserted into a lunar frozen orbit during its commissioning phase. These reasoning behind this was that it would allow for careful instrument calibration procedures during a time where maneuvers would be absent. [22] For a low-altitude lunar mission, the requirement of flying in frozen conditions is much more serious as the lunar gravity field can produce large altitude variations over time. This can potentially lead to impacting the lunar surface.

Orbital dynamics

This chapter deals with the basics of modeling the motion of a satellite in orbit. The starting point will be a discussion on the most fundamental properties of satellite orbits, as illustrated by the well-known two-body problem. Subsequently, an analysis of the most important perturbing accelerations is provided, accompanied by analytical and numerical methods to model their effects. The chapter is concluded by a quantitative comparison and evaluation of those effects.

3.1 Two-body problem

The prime textbook example for introductory astrodynamics is the two-body problem, as the equations of motion for this problem have a closed-form, analytical solution. Let us consider two point-mass bodies in free space, attracted to one another only by mutual gravitational pull, as depicted in Figure 3.1.

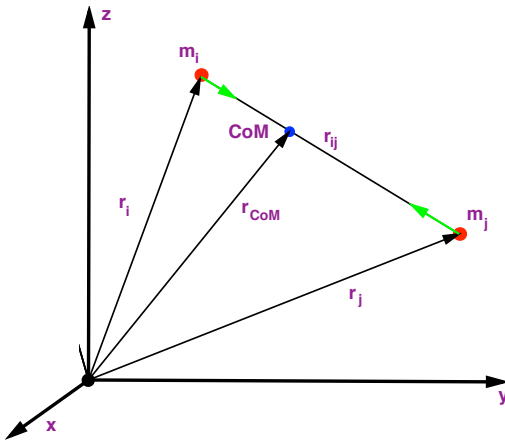


Figure 3.1: Sketch of the two-body problem.

In this situation, the equation of motion for body i with respect to body j can be written as: [1, 2, 23, 24]

$$\ddot{\mathbf{r}} = -\frac{\mu}{r^3} \mathbf{r} \quad (3.1)$$

where \mathbf{r} denotes the position vector from body i to j and μ is the gravitational parameter, defined as $\mu = G(m_i + m_j)$. Here, m_i and m_j denote the masses of bodies i and j , respectively, and G is the universal gravitational constant, carrying a value of $6.673\,84 \times 10^{-11} \text{ m}^3 \text{ kg}^{-1} \text{ s}^{-2}$. When modeling the orbit of a satellite around the Earth, the gravitational pull of the satellite on the Earth is clearly negligible. As a result, the gravitational parameter may be changed into $\mu = GM$, where M is Earth's mass. Note that this equation of motion, in this simple form, only holds in an inertial reference frame (a non-rotating reference frame with a non-accelerating origin). [1, 2, 23, 24]

Through the laws of conservation of energy and angular momentum, the solution to Equation (3.1) can be obtained. The solution is usually written as an equation that links the radial distance (r) between the satellite and Earth's center, to an angular component (θ). The result, known as the *orbit equation*, reads [1, 2, 23, 24]

$$r = \frac{a(1 - e^2)}{1 + e \cos \theta} \quad (3.2)$$

where a is known as the *semi-major axis*, e denotes the *eccentricity* and the angular variable θ is called the *true anomaly*. [23] These parameters are key in defining the shape of the orbit and the position of the satellite therein. From the form of the equation, it is apparent that it complies with the mathematical description of conic sections, hence we can conclude that in a two-body system, a satellite orbits in a two-dimensional plane and the orbit takes the shape of a conic section. Specifically, the eccentricity determines by what conic section the orbit shape is represented: for $0 < e < 1$, the orbit is an ellipse - the most important orbit shape for gravitationally bound satellites.

Satellite position

To describe the state of a satellite - its position and velocity - a minimum of six parameters is required in a Cartesian coordinate system. The state is often written as a vector, the so-called *state vector*, which takes the form

$$\mathbf{Y} = (x, y, z, V_x, V_y, V_z) \quad (3.3)$$

This representation is practical for numerical evaluation of Equation (3.1), as numerical integration in Cartesian coordinates is straightforward. However, the shape and size of the orbit cannot be determined intuitively from these six parameters. A historical set of parameters is usually used for this, named *Kepler elements*. A Keplerian state vector takes the form of

$$\mathbf{Y} = (a, e, i, \omega, \Omega, \theta_0) \quad (3.4)$$

where the first three and final symbol have been discussed earlier. The new elements are known as the *argument of pericenter* (ω) and the *right ascension of the ascending node* (Ω). The former is defined as the angular separation between the pericenter and the ascending node (point where the satellite passes the equatorial plane). The latter is defined as the angular separation between an inertially fixed reference direction (marked with symbol Υ) and the ascending node. The third one, θ_0 , is the angular separation between satellite and the periapsis at a certain epoch t_0 .

It is intuitively easy to imagine the shape and orientation of an orbit using Kepler elements, as they remain constant over time. All position information is stored in the true anomaly. However, this constancy is caused directly by the earlier assumption of treating the orbited body (Earth,

or the Moon, or any massive body) as a point mass. This means that only one force acts on the satellite, the so-called *central gravity*. Any additional forces that may act on the satellite are known as *orbital perturbations*, and these forces introduce variations in the six orbital elements. These varying orbital elements are referred to as *osculating elements*, and by definition these osculating elements are the Kepler elements that *the satellite would have had if no perturbations were present from the epoch of that state vector*.

The additional forces can be cast into the earlier equation of motion, after which it becomes considerably more difficult to solve in a closed form. Adding up all perturbing accelerations in a perturbing acceleration vector denoted as \mathbf{a}_p , the resulting equation reads [1, 2, 23, 24]

$$\ddot{\mathbf{r}} = -\frac{\mu}{r^3} \mathbf{r} + \mathbf{a}_p \quad (3.5)$$

The modeling of orbital perturbations will be the topic for the next sections.

3.2 Irregular gravity field

Earth's gravity field does not fit the description of a simple point mass gravitational potential - only perfectly spherical planets with a spherically symmetric mass distribution can be modeled in this way. Most planets are flattened by their own rotation, making them bulge outward near the equator. In addition, the density distribution inside the planet may vary significantly from location to location. [1, 2, 23, 24] These facts complicate the computation of the resulting force vector on a satellite orbiting the planet.

In order to compute the gravitational force of an arbitrary mass distribution on a satellite orbiting that distribution, the potential around such a distribution must be computed. This can be done by summing up contributions of small mass elements to the potential: [25]

$$U = G \iiint \frac{\rho(\mathbf{s}) d^3 \mathbf{s}}{|\mathbf{r} - \mathbf{s}|} \quad (3.6)$$

In this equation, $\rho(\mathbf{r})$ stands for the density at point \mathbf{s} inside the Earth and the term in the denominator is the satellite's distance from point \mathbf{s} , as shown in Figure 3.2. [25]

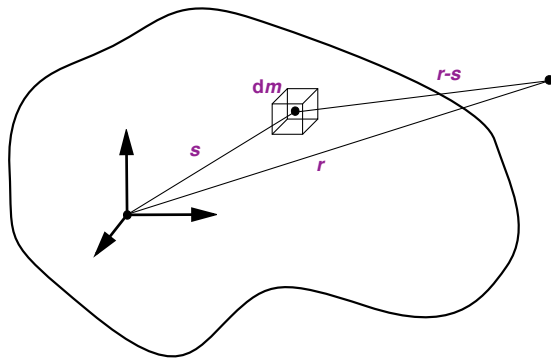


Figure 3.2: Contribution of small mass elements to determine the potential around a mass distribution.

The force resulting from the potential is easily computed through the well-known relation

$$\ddot{\mathbf{r}} = -\nabla U \quad (3.7)$$

Unfortuantely, it is very impractical and usually impossible to solve Equation (3.6). However, with considerable analytical effort is is possible to rewrite Equation (3.6) in terms of spherical harmonics, a set of special angular functions, through which the gravitational potential of most arbitrary density profiles can be modeled. In terms of spherical harmonics, the Earth's potential can be written as [1, 2, 23, 24, 25]

$$U = -\frac{\mu}{r} \left[1 + \sum_{l=2}^{\infty} \sum_{m=0}^l \left(\frac{R_E}{r} \right)^l P_{l,m}(\sin \varphi) [C_{l,m} \cos(m\theta) + S_{l,m} \sin(m\theta)] \right] \quad (3.8)$$

In this expression, R_E denotes the Earth's equatorial radius and r is the position vector magnitude, for which $r > R_E$ must hold. The angles φ and θ are used for the latitude and longitude in an Earth-rotating reference frame, respectively. The *cosine gravity coefficients* $C_{l,m}$ and *sine gravity coefficients* $S_{l,m}$ are model parameters, whose values have been determined from measured data from gravity field mapping missions. $P_{l,m}$ denotes the *associated Legendre polynomials* of degree l and order m .

Equation (3.8) can be split up into a **zonal** part and a **tesseral** part, where the zonal terms are only a function of latitude:

$$U = -\frac{\mu}{r} \left[1 - \sum_{l=2}^{\infty} J_l \left(\frac{R_E}{r} \right)^l P_l(\sin \varphi) + \dots \right. \\ \left. \sum_{l=2}^{\infty} \sum_{m=2}^l J_{l,m} \left(\frac{R_E}{r} \right)^n P_{l,m}(\sin \varphi) [\cos m(\theta - \theta_{l,m})] \right] \quad (3.9)$$

where the constant $\theta_{l,m}$ is used as an offset to fix the potential to a specific longitude. In addition, the following notations were introduced: [2, 3, 24, 25]

$$\begin{aligned} C_{l,m} &= J_{l,m} \cos m\theta_{l,m} \\ S_{l,m} &= J_{l,m} \sin m\theta_{l,m} \\ J_l &= J_{l,0} = -C_{l,0} \end{aligned}$$

Effects

The irregular gravity field has profound effects on the behavior of orbital elements of a satellite trajectory. In terms of magnitude, the first zonal gravity field term J_2 is about a thousand times larger than the other terms, and thus its effect is most profound. Clearly, the orbital elements no longer remain static as was the case for the ideal two-body problem, as shown in Figure 3.3.

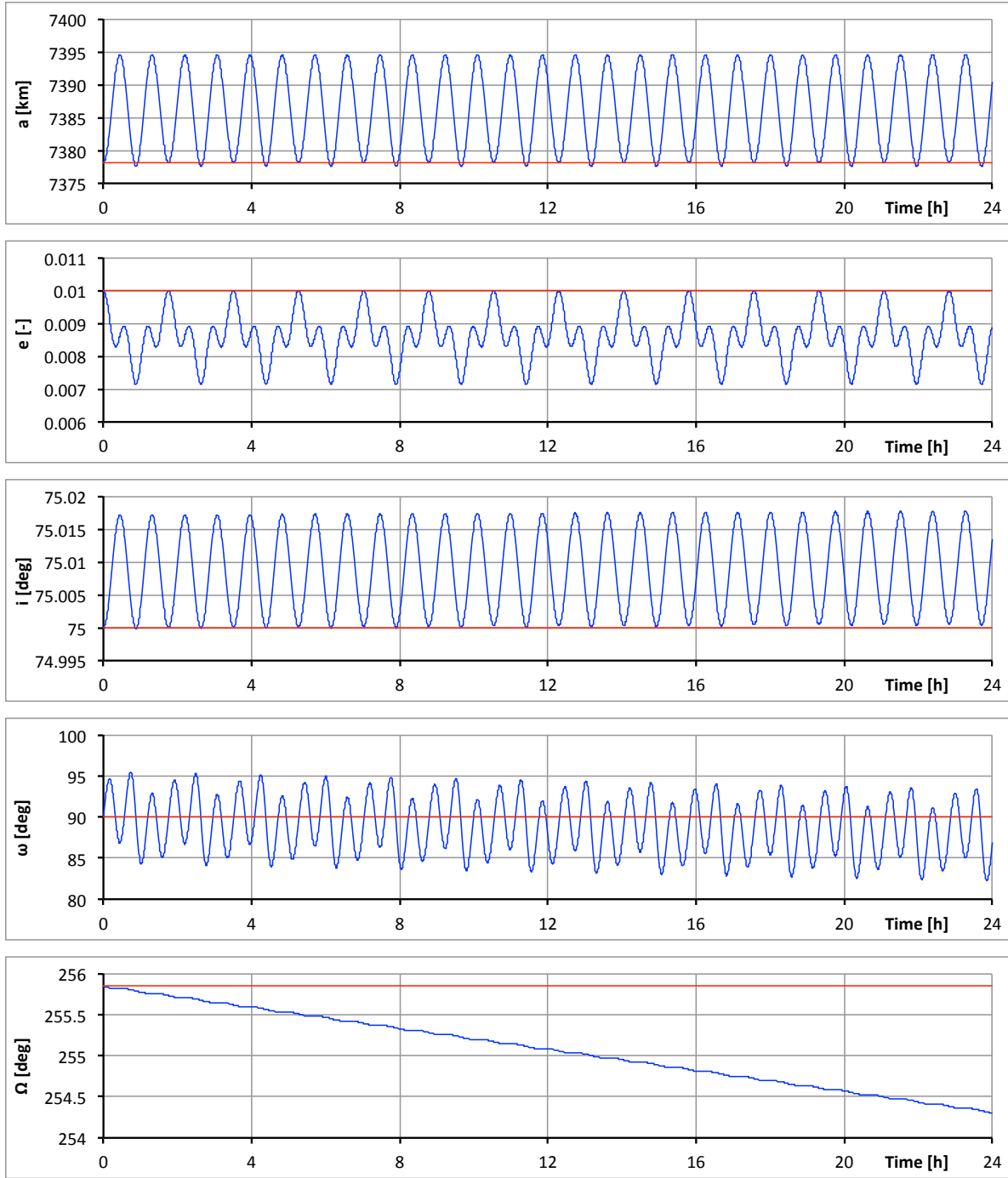


Figure 3.3: Osculating elements in a J_2 gravity field model, for a satellite released at an inclination of $i = 75$ degrees, and an altitude of $h = 1000$ km. The red line visualizes the orbital element values of the Kepler orbit.

From Figure 3.3, the effect of the biggest orbital perturbation becomes apparent. *Short-period* effects, which are characterized by having a period of (less than) one orbital period, are visible in all five otherwise static Kepler elements. Clearly for the right ascension of the ascending node, a *secular* effect has the most dominant effect. Such a secular effect is visible in the behavior of the argument of periapsis, too. These secular effects, due to J_2 , are two well-known effects known as the *precession of the ascending node* and the *precession of the argument of periapsis*.[1, 2, 23, 24, 25] As the degree and order of the gravity field model increase, so does the complexity of the behavior of the orbital elements. Each additional term causes its own distinctive behavior of the osculating elements, and adds its own periodic and secular effects.

3.3 Atmospheric drag

Earth's atmosphere extends further than usually anticipated: even at an altitude of 1000 km, satellites experience atmospheric drag. Even though the density at these altitudes is low, the high velocity of a satellite still causes notable drag. When assuming that the incident flow is not disturbed by the satellite itself (free molecular flow), the drag experienced by a satellite may be expressed as an acceleration:

$$\mathbf{a}_D = -\frac{1}{2} C_d \frac{\rho A}{m} |\mathbf{V}| \mathbf{V} \quad (3.10)$$

where C_d is the drag coefficient, ρ is the local density, A is the reference cross-sectional area and m is the satellite mass. The velocity used in this equation is not the absolute velocity but rather the velocity with respect to the atmosphere, which may be assumed static or co-rotating with the Earth.

Modeling the effects of drag on a satellite proves challenging - a precise approach would require detailed information about the local properties of the atmosphere such as density, composition and the velocity of high-altitude winds. In addition, the behavior of the atmosphere at satellite altitude is highly dynamic: the lower layers of the atmosphere expand when radiated by the Sun, greatly increasing the density in the upper layers of the atmosphere. This expansion can cause the density at 1000 km altitude to increase up to three orders of magnitude. [3] In addition, the attitude and geometry of the satellite needs to be known exactly in order to continuously update the cross-sectional surface area. At the expense of accuracy, it is possible to assume a static (not-rotating) atmosphere, a constant surface area, and the density may be retrieved from a high-altitude density model or from using an exponential model for the atmosphere.

A well-known atmosphere model, which is used throughout the aerospace sector, is the NRL-MSIS-E-00 model (US Naval Research Laboratory Mass Spectrometer and Incoherent Scatter radar - including Exosphere 2000). This empirical model is based on measurements of instruments of several satellite missions operating in LEO. It is possible to retrieve numerous atmosphere characteristics from this model, such as local density, composition and temperature. These quantities depend on many variables which need to be fed into the model, such as satellite position, altitude, local solar time and incoming solar flux intensity. [26] In this model the incoming solar flux input is in terms of the emitted solar radiation at 10.7 cm wavelength, known as the F10.7 index. This value follows the Sun's 11-year cycle in terms of magnitude, as shown in Figure 3.4.

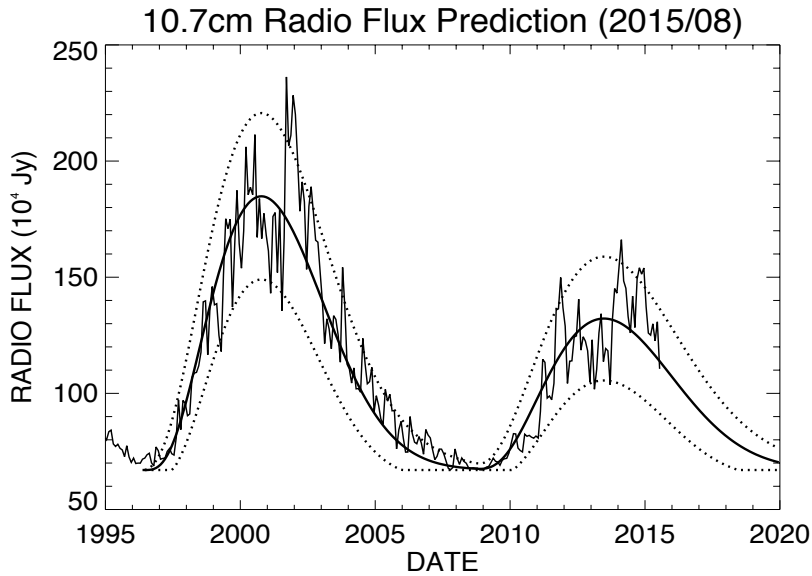


Figure 3.4: Solar radiation F10.7 index against time. [27]

Effects

Drag is a non-conservative force, which means that the energy of the orbiting satellite is directly affected: the semi-major axis shrinks over time. Satellites in an eccentric orbit experience an effect called **circularization**: the higher drag at periapsis slows the satellite down, lowering the apoapsis until the orbit becomes circular. As such, the orbital elements which are most affected by drag are the eccentricity and the semi-major axis. [3] The effects of drag on the trajectory of a satellite in a relatively low near-circular orbit are shown in Figure 3.5.

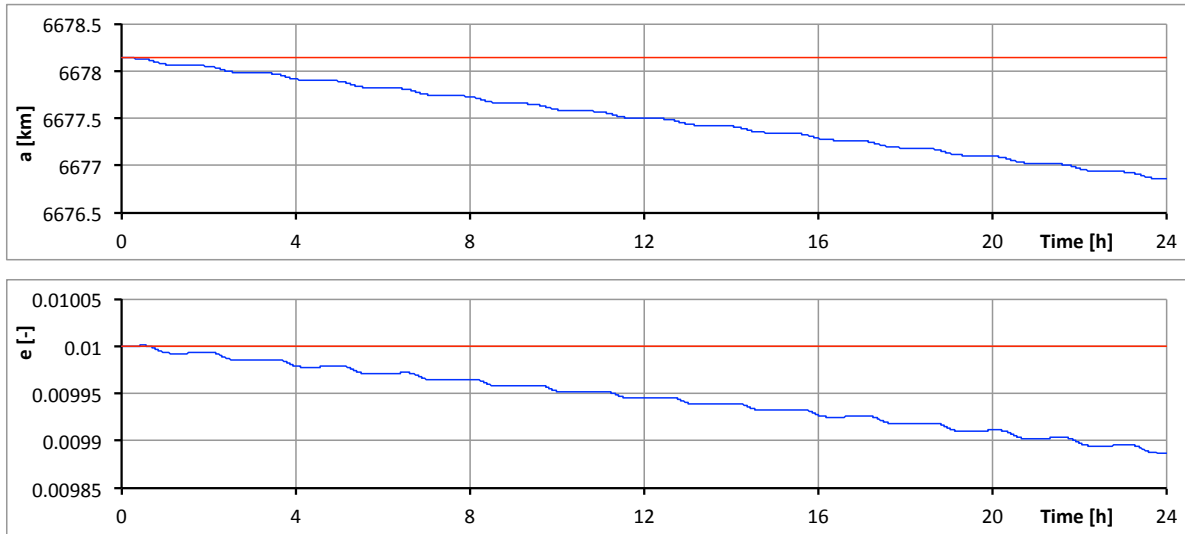


Figure 3.5: Effect of drag on the osculating orbital elements e and a for a satellite released at an altitude of 300 km at eccentricity 0.01. The red line denotes the Kepler orbit.

3.4 Third-body attraction

Earth-orbiting satellites are also attracted by the gravitational pull of the Moon, the Sun and, in theory, by all other bodies in the Solar system. In an Earth-centered fixed reference frame, the geometry of such a third-body perturbation can be visualized as in Figure 3.6.

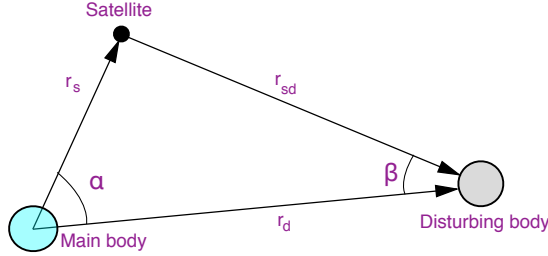


Figure 3.6: Geometry of the third-body effect.

The force due to a single perturbing gravitational potential can be written as [23]

$$\mathbf{f}_{3rd} = \mu_d \left(\frac{\mathbf{r}_{sd}}{r_{sd}^3} - \frac{\mathbf{r}_d}{r_d^3} \right) \quad (3.11)$$

where μ_d is the gravitational parameter of the disturbing body ($\mu_d = GM_d$). The second term on the right-hand side of Equation (3.11) is a correction to account for the fact that the disturbing mass center is not an inertial reference frame.

Effects

The effects of third-body attraction due to the Moon and Sun are mostly periodic in nature. [28] The change in osculating elements is smaller than the J_2 -effect. When monitoring the changes for a whole year though, there are some secular effects on the (one-day) averaged orbital elements, which are depicted in Figure 3.7.

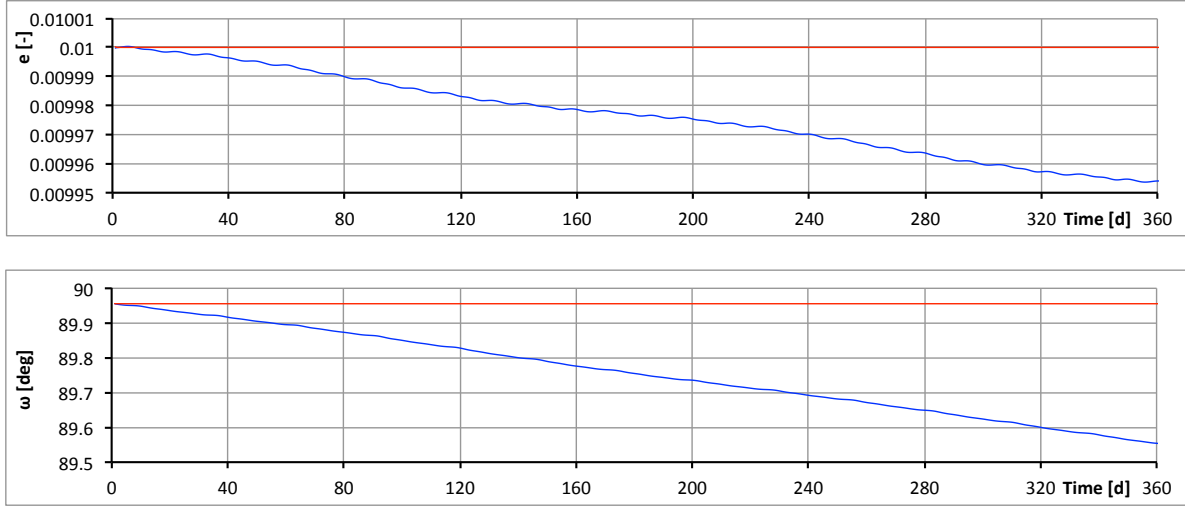


Figure 3.7: Averaged osculating elements in a central gravity field and including third-body attraction, for a satellite released at an inclination of $i = 75$ degrees, and an altitude of $h = 1000$ km. The red line denotes the Kepler orbit.

3.5 Radiation pressure

Despite lacking mass, photons originating from the Sun carry momentum, which can be transferred to a spacecraft upon impact. The combined effect of a large number of photons can result in a perturbing force that can measurably perturb the satellite's orbit. From the definitions of the photon momentum, the inverse-square law and Newton's second law, the solar radiation force can be expressed in terms of the total solar luminosity L_{\odot} :

$$a_{rad} = -C_R \frac{L_{\odot}}{4\pi c R^2} \frac{A}{m} \hat{\mathbf{r}}_{s\odot} \quad (3.12)$$

where C_R is the reflection coefficient, R is the distance between the satellite and the center of the Sun, A is the spacecraft surface area perpendicular to the direction of R and c is the speed of light. The vector $\hat{\mathbf{r}}_{s\odot}$ points from the satellite towards the center of the Sun. For most satellites, C_R takes a value between 1.1 - 1.5, depending on the material used. For Earth-bound satellites, usually the constant $W = L/(4\pi R^2)$ is usually used - this so-called solar constant carries a value of $1.367 \times 10^3 \text{ W m}^{-2}$. [3]

Though it is relatively simple to model radiation pressure, it is not so simple to model the effect of eclipses. Naturally, the force exerted by radiation pressure is to be zero once the satellite is eclipsed by another body. In order to model this, Equation (3.12) can be multiplied by a factor between 0 and 1, the so-called illumination constant, which depends on whether the satellite is in full sunlight (1) or in full eclipse (0). This constant can be computed by considering a model of two overlapping celestial disks, one for the Sun (the occulted body) and one for Earth (the occulting body), together with the geometry of the satellite-Earth-Sun system. [25]

Effects

The effect of radiation pressure are mostly periodic. [28] However, there are some secular effects that can build up over a longer time span. The long-term effect of radiation pressure on the crucial elements e and ω , as plotted for a whole year, can be found in Figure 3.8.

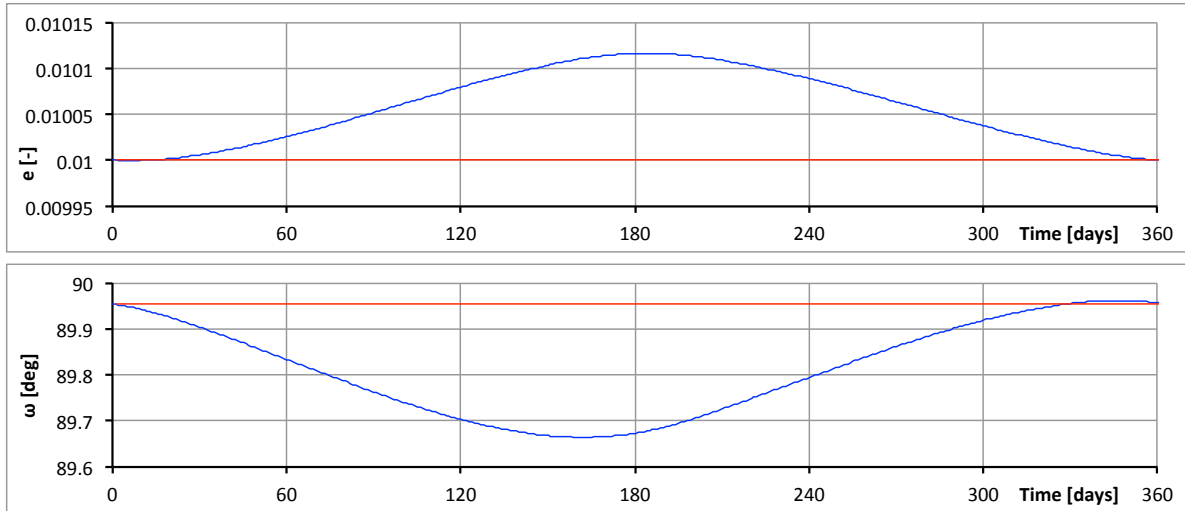


Figure 3.8: Averaged osculating elements in a central gravity field and including solar radiation pressure, for a satellite released at an inclination of $i = 75$ degrees, and an altitude of $h = 1000$ km. The red line denotes the Kepler orbit.

In this particular case, the effect cancels out after a year, which makes sense in a model where no other perturbations are present. The orientation of the orbit with respect to the Sun will remain the same, and any accumulated effects in one half of the trajectory will be canceled out during the other half. However, when more gravity field terms are included, the secular effect in Ω due to J_2 will certainly affect the behavior of the other elements under radiation pressure. For a Sun-synchronous frozen orbit, this effect may eventually accumulate and decrease the stability. [29]

3.6 Smaller perturbations

Apart from the main perturbing forces, caused by the non-spherically symmetric gravity field, the higher atmosphere, the radiation pressure and other gravitational bodies, there are some minor perturbing forces caused by other mechanisms. Their effects are usually small, but a qualitative description is provided for completeness.

Electromagnetic forces, caused by charge build-up in the upper atmosphere, can lead to attraction or repulsion of the satellite, depending on the total charge it carries. More importantly, it can deflect the satellite's orbit through a Lorentz force, in combination with the Earth's magnetic field. Modeling this acceleration is not straightforward as ionization in the upper atmosphere is a complicated process which is hard to model.

Relativistic precession is caused by Albert Einstein's theory of general relativity, which stated that the gravitational field is described by the so-called Schwarzschild metric, for which the Newtonian gravity field is a very good approximation. However, the additional effects from the theory of relativity perturb the standard Keplerian motion. One of the more profound (yet still very small) effects is a gradual rotation in the line connecting the apses of an orbit (the major axis) around the main focus of the ellipse, in the direction of motion of the satellite.

Many smaller perturbations exist, such as the component of the radiation pressure perpendicular to the vector pointing from the satellite to the Sun due to the satellite's relative velocity (*Poynting-Robertson drag*), the change in mass distribution of the Earth (*tidal effects*), the interaction with electric and magnetic fields in the vicinity of the spacecraft (*electromagnetic perturbations*) and even the *speed of gravity* itself.

In this chapter, it has been made clear that the most influential perturbations are due to Earth's gravity field, atmospheric drag, third-body gravitational attraction and radiation pressure. All of these perturbations have significant influences long-term or secular effects on the mean argument of periapsis and eccentricity, and are therefore taken into account for the remainder of this work. The smaller perturbations are neglected.

Frozen orbits

The concept of a frozen orbit is defined as an orbit chosen such that *one or more mean orbital elements do not (or minimally) change under the influence of orbital perturbations.* [3] Though the definition may apply to each (set of) orbital element(s), classically, the concept focuses on minimizing variations in the argument of periaxis (ω) and the eccentricity (e). Such orbits prove vital for altimetry missions, as in this way the altitude above the surface is a constant depending on the geographical location of the sub-satellite point. A first-order analysis on the right conditions for a frozen orbit consider only the J_2 and J_3 terms of the gravitational field, based on the Lagrange planetary equations. (Section 4.1) A similar effort, based on Kaula's disturbing potential, is also discussed in Section 4.2. The chapter is concluded with a study of the behavior of two well-known satellites that were placed in frozen orbits, ERS-2 and T/P, in Section 4.3.

4.1 J_2 - J_3 analysis

The first approach in finding the right conditions for an e, ω -frozen orbit is to introduce the well-known *Lagrange planetary equations* (LPE's). This set of six equations describes the time-evolution of the six orbital elements under the influence of a *disturbing potential* function \tilde{V} . The LPE's are listed below: [3, 30]

$$\frac{da}{dt} = \frac{2}{na} \frac{\partial \tilde{V}}{\partial M} \quad (4.1a)$$

$$\frac{de}{dt} = \frac{1-e^2}{na^2 e} \frac{\partial \tilde{V}}{\partial M} - \frac{\sqrt{1-e^2}}{na^2 e} \frac{\partial \tilde{V}}{\partial \omega} \quad (4.1b)$$

$$\frac{di}{dt} = \frac{\cos i}{na^2 \sqrt{1-e^2} \sin i} \frac{\partial \tilde{V}}{\partial \omega} - \frac{1}{na^2 \sqrt{1-e^2} \sin i} \frac{\partial \tilde{V}}{\partial \Omega} \quad (4.1c)$$

$$\frac{d\omega}{dt} = -\frac{\cos i}{na^2 \sqrt{1-e^2} \sin i} \frac{\partial \tilde{V}}{\partial i} + \frac{\sqrt{1-e^2}}{na^2 e} \frac{\partial \tilde{V}}{\partial e} \quad (4.1d)$$

$$\frac{d\Omega}{dt} = \frac{1}{na^2 \sqrt{1-e^2} \sin i} \frac{\partial \tilde{V}}{\partial i} \quad (4.1e)$$

$$\frac{dM}{dt} = n - \frac{1-e^2}{na^2 e} \frac{\partial \tilde{V}}{\partial e} - \frac{2}{na} \frac{\partial \tilde{V}}{\partial a} \quad (4.1f)$$

These equations form one of the backbones in analytical analyses on the trajectory of perturbed satellites. Nowhere in the derivation it is assumed that the perturbing force has to be small, so these equations are generally valid. A backside of the LPE's is that they are poorly defined in the case that $e = 0$ or $\sin i = 0$, leading to singularities. In addition, the reliance on formulating the perturbation as a potential function limits their use to perturbations that can indeed be formulated in such a manner. To overcome this limitation, it is possible to express the LPE's in terms of radial, along-track and cross-track accelerations. The corresponding expressions are referred to as the Gauss' form of the LPE's, though they will not be used in the remainder of this work. [3]

Starting with the LPE's, it is necessary to obtain an expression for the disturbing potential. Such an expression is obtained from the spherical harmonics equation (Equation (3.9)), and for this particular case all tesseral terms are ignored and summation terms are only included up to $l = 3$. Then, the disturbing potential has to be doubly-averaged over the mean anomaly to remove the short-period and long-period variations. This allows for a final expression to be in terms of mean orbital elements, as opposed to the LPE's themselves. [3] Subsequently, the latitude φ can be expressed in terms of orbital elements through spherical geometry, and the LPE's for eccentricity and argument of periapsis (Equations (4.1b) and (4.1d)) can be written as [4, 31]

$$\frac{d\bar{e}}{dt} = \frac{-3\bar{n}J_3R_E^3 \sin \bar{i}}{2\bar{a}^3(1-\bar{e}^2)^2} \left(1 - \frac{5}{4} \sin^2 \bar{i}\right) \cos \bar{\omega} \quad (4.2a)$$

$$\frac{d\bar{\omega}}{dt} = \frac{3\bar{n}J_2R_E^2}{\bar{a}^2(1-\bar{e}^2)^2} \left(1 - \frac{5}{4} \sin^2 \bar{i}\right) \left[1 + \frac{J_3R_E}{2J_2\bar{a}(1-\bar{e}^2)} \left(\frac{\sin^2 \bar{i} - \bar{e} \cos^2 \bar{i}}{\sin \bar{i}}\right) \frac{\sin \bar{\omega}}{\bar{e}}\right] \quad (4.2b)$$

To achieve a frozen orbit, these two equations have to be set to zero. The first approach would be to nullify the term $(1 - \frac{5}{4} \sin^2 i)$, for which one obtains the so-called critical inclinations: $i = 63.4349$ or 116.5651 degrees. To escape the inclination requirement, the argument of periapsis can be set to $\omega = 90$ to nullify the right-hand side of Equation (4.2a). The most straightforward approach now is to nullify the right-hand side of Equation (4.2b), which yields an expression valid for arbitrary inclination: [31, 4]

$$\left[1 + \frac{J_3R_E}{2J_2\bar{a}(1-\bar{e}^2)} \left(\frac{\sin^2 \bar{i} - \bar{e} \cos^2 \bar{i}}{\sin \bar{i}}\right) \frac{1}{\bar{e}}\right] = 0 \quad (4.3)$$

The previous result may be rewritten in terms of the inclination:

$$\bar{e} = -\frac{J_3R_E}{2J_2\bar{a}(1-\bar{e}^2)} \left(\frac{\sin^2 \bar{i} - \bar{e} \cos^2 \bar{i}}{\sin \bar{i}}\right) \quad (4.4)$$

Assuming e is negligible (order of J_2) it can be shown that

$$\bar{e} \approx -\frac{J_3R_E}{2J_2\bar{a}} \sin \bar{i} \quad (4.5)$$

This simple equation binds together the eccentricity, inclination and semi-major axis in order to obtain a frozen orbit. Though one of the back-bones of the design process, it is important to note that several assumptions along the way can threaten its accuracy. For example, the behavior around the critical inclination is ill-defined. In addition, the assumption of $e \approx 0$ on the r.h.s. is selective, considering that it is actually the parameter that is solved for in the end - plus, this assumption

would fail for low inclinations as the $\sin \bar{i}$ term would give rise to a singularity. What's more, this equation is of course solely based on the first two zonal terms of the gravitational potential. Though the J_2 -effect indeed overpowers all others by around three orders of magnitude, its counterpart J_3 , which is equally important in this analysis, does not. [4, 31]

A more accurate approach needs to consider all (or in any case more) zonal terms. It is of course possible to repeat the steps in this section for extra zonal terms in Equation (3.9), but the expressions will become tedious and will have to be solved numerically. However, there is a method which goes to great lengths to find an analytical solution for the problem by making use of an expression for the perturbing potential in Kepler elements, known as Kaula's potential.

4.2 Kaula's potential

It is possible to express the Earth's gravitational potential (Equation (3.8)) directly in terms of orbital elements:

$$U = -\frac{\mu}{r} + \frac{\mu}{a} \sum_{l=2}^{\infty} \sum_{m=0}^l \sum_{p=0}^l \sum_{q=-\infty}^{\infty} \left(\frac{R_E}{a} \right)^l F_{l,m,p}(i) G_{l,p,q}(e) S_{l,m,p,q}(\omega, \Omega, M, \theta_{GMST}) \quad (4.6)$$

where the S function contains the gravitational coefficients.

$$S_{l,m,p,q}(\omega, \Omega, M, \theta_{GMST}) = \begin{cases} C_{l,m} \cos \psi_{nmpq} + S_{l,m} \sin \psi_{lmpq} & \text{if } (l-m) \text{ even} \\ -S_{l,m} \cos \psi_{lmpq} + C_{l,m} \sin \psi_{lmpq} & \text{if } (l-m) \text{ odd} \end{cases} \quad (4.7)$$

and the phase angle ψ_{lmpq} is introduced as

$$\psi_{lmpq} = (l - 2p)\omega + (l - 2p + q)M + m(\Omega - \theta_{GMST}) \quad (4.8)$$

The function $F_{l,m,p}(i)$, known as the inclination function, is a finite series of trigonometric functions of the inclination. The function $G_{l,p,q}(e)$, known as the eccentricity function, is an infinite power series of the eccentricity. [30] The derivation of these functions is tedious, but their final form is presented for completeness. The inclination function can be written as

$$F_{l,m,p}(i) = \sum_{t=0}^{\min(p,k)} \left[\frac{(2l-2t)!}{t!(l-t)!(l-m-2t)!2^{2l-2t}} \sin^{l-m-2t}(i) \dots \right. \\ \dots \times \sum_{s=0}^m \binom{m}{s} \cos^s(i) \sum_c \binom{l-m-2t+s}{c} \binom{m-2}{p-t-c} (-1)^{c-k} \left. \right] \quad (4.9)$$

The form of Kaula's eccentricity function depends on which variations are being studied. For long-period and secular variations (the main focus in this work), for which $(l - 2p + q) = 0$, it can be written as [30]

$$G_{l,p,(2p-l)}(e) = \frac{1}{(1-e^2)^{l-\frac{1}{2}}} \sum_{d=0}^{p'-1} \binom{l-1}{2d+l-2p'} \binom{2d+l-2p'}{d} \left(\frac{e}{2} \right)^{2d+l-2p'} \quad (4.10)$$

where

$$\begin{aligned} p' &= p && \text{for } p \leq l/2 \\ p' &= l - p && \text{for } p \geq l/2 \end{aligned}$$

Kaula's formulation for the gravitational potential can be used to obtain an expression for the frozen eccentricity for all zonal terms of the gravity field. In work by Rosborough and Ocampo [8], Kaula's potential function is first set up for secular variations for which $l = 2p$ and $q = 0$, and consequently it is set up for long-period variations, for which $2p - l = q$. [8] The resulting potential functions are then inserted into the Lagrange equations relevant to the frozen orbit problem (Equations (4.1b) and (4.1d)). After a tedious derivation, for which the details will be skipped, it is possible to obtain an expression for the frozen mean eccentricity: [8]

$$\bar{e} = \pm \frac{2 \sum_{p=1}^{\infty} \left(\frac{R_E}{\bar{a}} \right)^{2p+1} F_{(2p+1)0p} C_{(2p+1)0} \sin \bar{i}}{\sum_{p=1}^{\infty} \left(\frac{R_E}{\bar{a}} \right)^{2p} \left[F'_{(2p)0p} \cos \bar{i} - p(2p+1) F_{(2p)0p} \sin \bar{i} \right] C_{(2p)0}} \quad (4.11)$$

This expression is generally valid in zonal geopotential models to an arbitrary degree. The \pm sign depends on the signs of the coefficients and should be chosen such that the final outcome is positive. For arbitrary inclinations (apart from the critical inclination) this equation can be used to plot contour lines of the frozen mean eccentricity as function of semi-major axis and inclination, as shown in Figure 4.1.

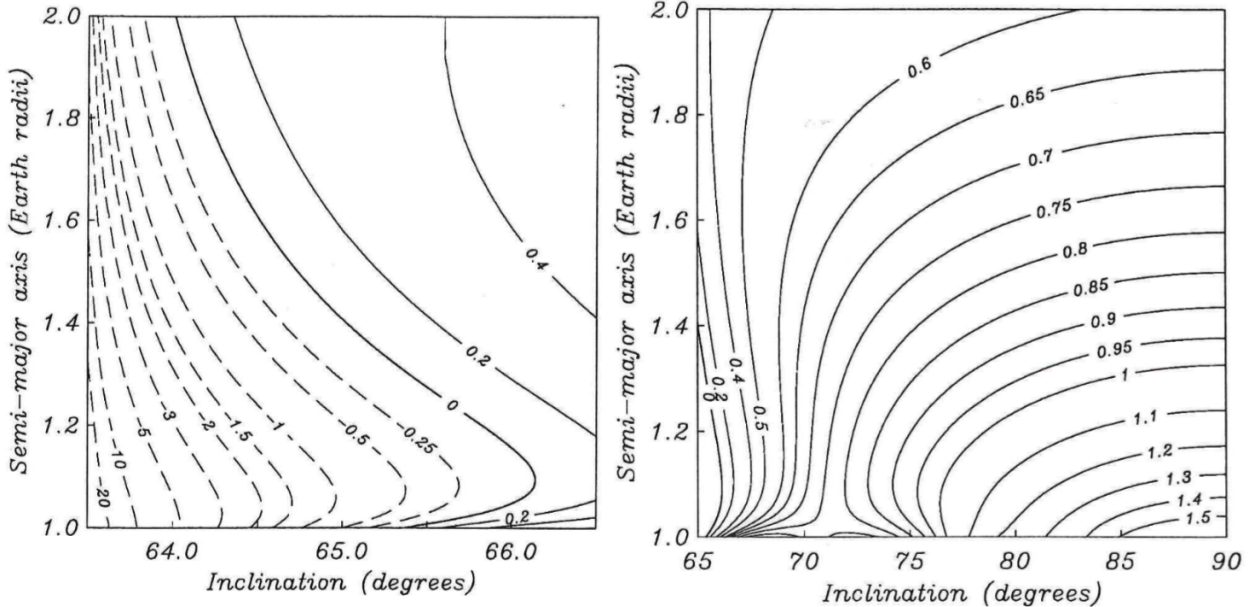


Figure 4.1: Frozen mean eccentricity contour plot as function of mean semi-major axis and mean inclination, computed for all zonal coefficients complete up to order 50. Eccentricity values are to be multiplied by 10^{-3} . Dashed lines indicate that $\bar{\omega}$ should be 270 degrees. [8]

In addition, Equation (4.11) can be used to plot the effect of adding higher order zonal terms when compared to the simple $J_2 - J_3$ solution. A comparison between this simple model and a model complete up to degree 12 is shown in Figure 4.2.

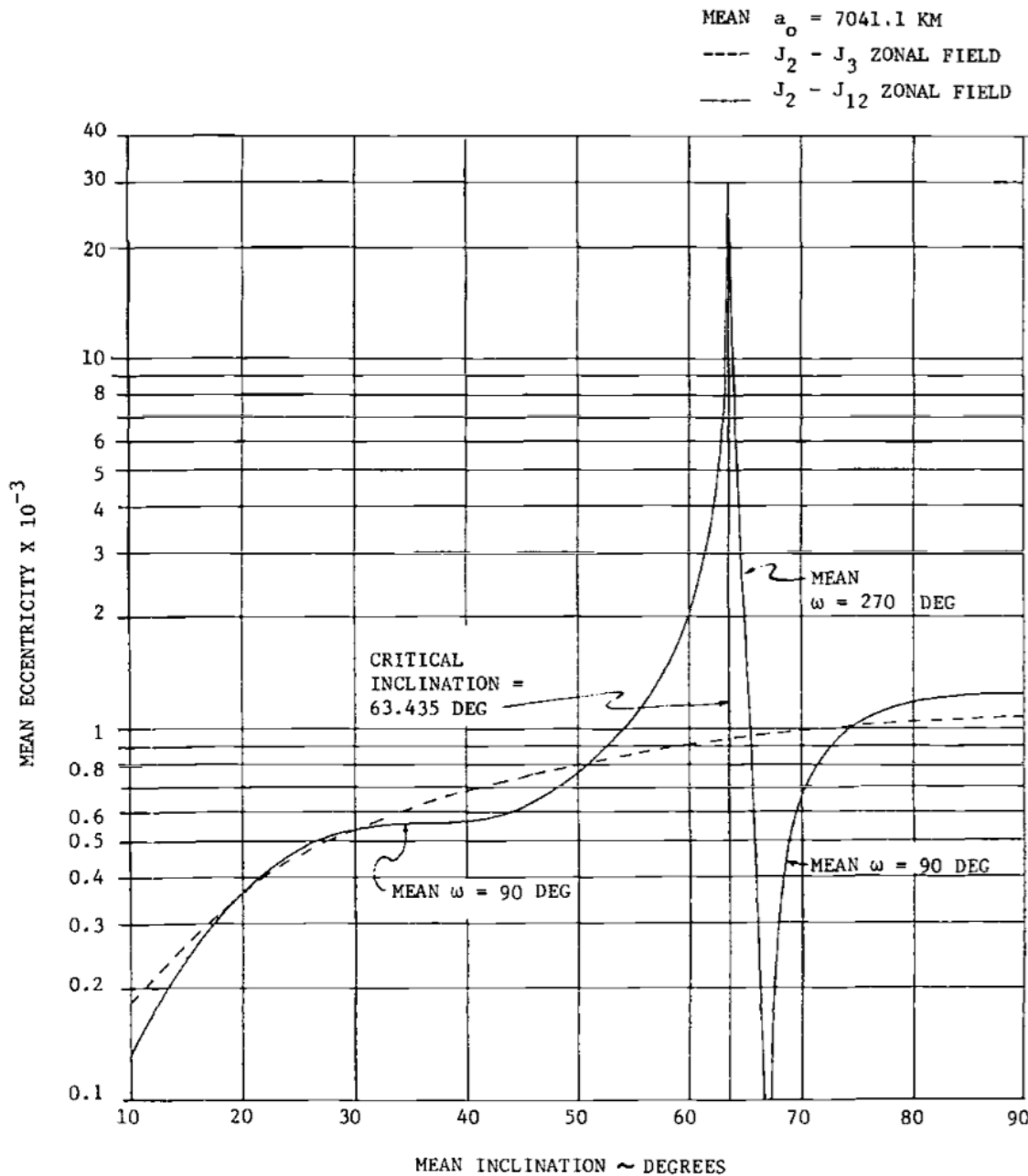


Figure 4.2: Frozen mean eccentricity as function of the mean inclination for a fixed mean semi-major axis, using Equation (4.11). [2]

It is emphasized that in the simplest case of only taking into account C_{20} and C_{30} , the result of the basic analysis in Section 4.1 is obtained again: [8]

$$\bar{e} = \mp \frac{J_3 R_E}{2 J_2 \bar{a}} \sin \bar{i} \quad (4.12)$$

4.3 Actual satellite behavior

For a frozen orbit, usually the behavior of the mean argument of periapsis and the mean eccentricity is of particular interest. In an idealized case, these two parameters should condense into a static point when their behavior is plotted over a certain time interval. Under the influence of other perturbations this will never be the case, but it is of course insightful to inspect the actual behavior of satellites that fly in a frozen orbit. In this section, two well-known missions are selected for a closer inspection: the ERS-2 satellite and the US-French TOPEX/Poseidon. Both fly in frozen orbits, but their mean inclinations, mean eccentricities and mean semi-major axes differ significantly from each other. By choosing these two, insight can be gained in two different orbital regions.

The orbit solutions (obtained from [32] and [33]) used are in .SP3 format, which is one of the more common file types for storing precise orbits. To actually isolate the mean orbital elements from these files, the following processing steps had to be carried out:

- **Transformation** from Earth-corotating (WGS84) reference frame to Earth-centered inertial (ECI) reference frame.
- **Transformation** from Cartesian coordinates to osculating Kepler elements.
- **Transformation** from osculating Kepler elements to mean Kepler elements (see Section 5.2).
- **Averaging** of the reconstructed mean elements to further filter out periodic effects (see Section 5.3).

The latter three points are also part of the methodology to find frozen orbits, which is elaborated upon further in this work. The first transformation is required as the .SP3 format usually contains data in the WGS84 (Earth co-rotating) reference frame, and thus has to be transformed to an inertial reference frame.

The last step (averaging of the reconstructed mean elements) is an important part of filtering out unwanted long-period variations in the mean elements which are of no interest in the search for a frozen orbit which is to remain stable in the long run. In this section, two averaging intervals will be used for investigating the behavior of ERS-2 and T/P. Either averaging takes place of one-orbit intervals, or over one-day intervals.

ERS-2

The behavior of \bar{e} and $\bar{\omega}$, for reconstructed mean elements averaged over one-orbit intervals, is shown in Figure 4.3. From this figure, it becomes apparent that a repeating pattern with a period of roughly one day dominates the motion in terms of \bar{e} and $\bar{\omega}$. This daily ‘wobble’ pattern persists in all three days that were included in the plot (and in all days that were not included in the plot, too). This wobble is undesirable, as an optimization specifically targeted at minimizing the variation in these parameters will suffer from the overshadowing effect of these long-period variations. As such, from Figure 4.3 the need to switch to a lengthier averaging interval becomes imperative.

Results of the same procedure as earlier, but now for one-day averaged orbital elements, and plotting the data for an entire year, are shown in Figure 4.4. Again, the dots here denote the combination of \bar{e} and $\bar{\omega}$, but now averaged over an entire day.

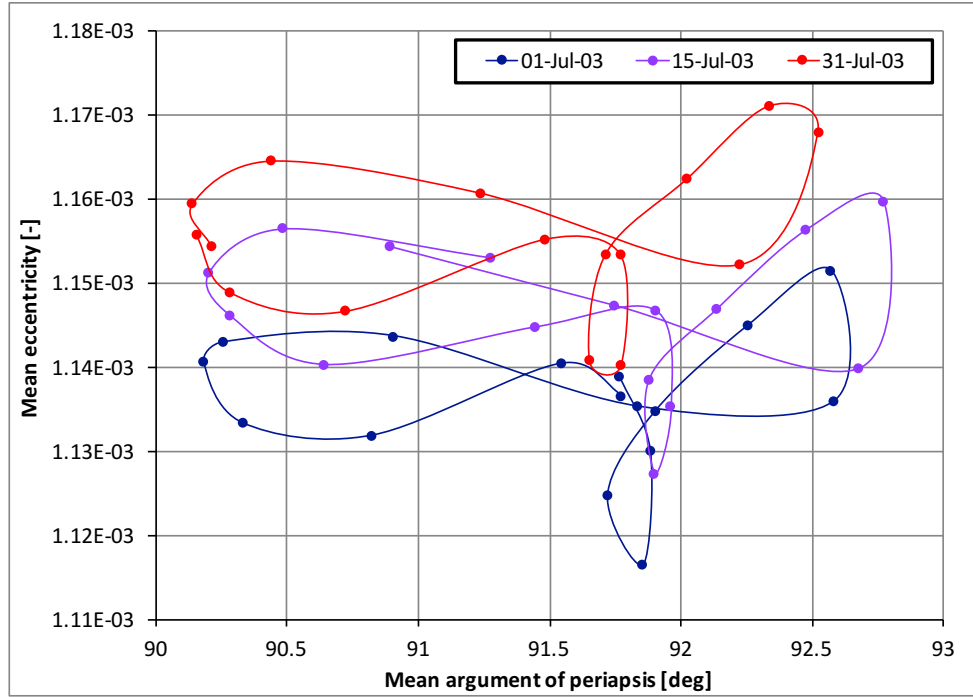


Figure 4.3: Behavior of \bar{e} and $\bar{\omega}$ on three days in July 2003, showing a daily repeating pattern in the mean elements. Each marker represents the mean elements for one complete revolution.

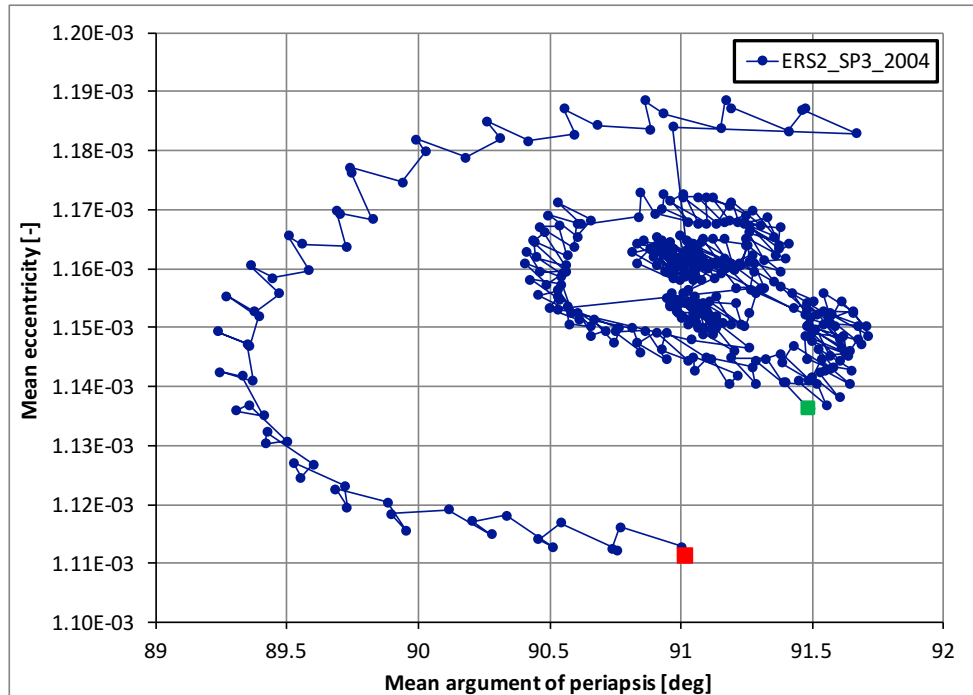


Figure 4.4: Behavior of \bar{e} and $\bar{\omega}$ for ERS-2 throughout 2004. Each marker represents the reconstructed mean and subsequently one-day averaged \bar{e} and $\bar{\omega}$. The green and red marker depict the start and end time, respectively.

Clearly, the increased averaging interval has filtered out the daily pattern that earlier showed up in Figure 4.3. The new pattern in Figure 4.4 actually looks a lot more like what one expects for a frozen orbit, as the variations \bar{e} and $\bar{\omega}$ now have roughly the same magnitude as the daily variations in case of one-orbit averaging. In Figure 4.4, there is a clear distinction between an inner pattern and an outer pattern in the zoomed figure, likely due to a planned maneuver, as the accuracy of the orbit solutions is degraded in the time span where this jump happens. [32] Other sudden jumps can also be observed, all of them likely due to maneuvers. The ‘inner ring’ and ‘outer ring’ in Figure 4.4 show a zigzagging pattern, which requires some explanation. This pattern is caused by the numerical averaging over one-day periods by sampling the one-orbit averages that appeared in earlier results. As the number of complete revolutions per day varies (13 or 14 per day for ERS-2), the sampling is slightly inconsistent which results in the observed pattern.

At a mean altitude of roughly 780 km, ERS-2 endured significant atmospheric drag. This drag is being compensated for by regular reboosts which are clearly visible in Figure 4.5 where the mean semi-major axis of ERS-2 is plotted over 2004. In addition to the predictable behavior caused by drag & reboosts, two very clear sudden drops are visible. The dates corresponding to these spikes can be linked to two orbital debris avoidance maneuvers that were carried out in 2004, and these maneuvers directly affect the quality of the precise orbit solutions. [34]

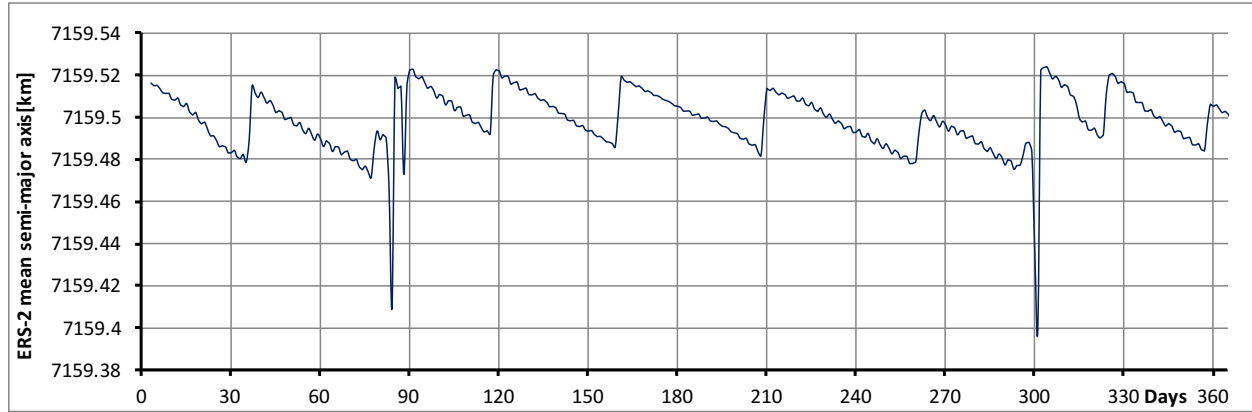


Figure 4.5: Daily-averaged reconstructed mean altitude of ERS-2 throughout 2004.

TOPEX/Poseidon

The behavior of \bar{e} and $\bar{\omega}$ for T/P is quite different than that of ERS-2. This comes to no surprise, as T/P is in a completely different target orbit: higher mean altitude (1330 km), lower mean inclination (66.04 degrees) and very small mean eccentricity (0.000095). T/P’s orbit is near the critical inclination, where the long-term effects of the J_2 perturbation cancel out, and as such, the other perturbations have a more significant effect on the orbital elements. As in the last section on ERS-2, first the behavior is investigated for one-orbit averaging of the orbital elements, after reconstructing the mean elements from the osculating elements. The result of this investigation is shown in Figure 4.6 for the orbital elements \bar{e} and $\bar{\omega}$.

Clearly, a daily wobble, as observed for ERS-2, is present in the behavior of T/P as well. If the re-constructed mean elements are averaged over one-day periods, the secular effects become more clear, as shown in Figure 4.7.

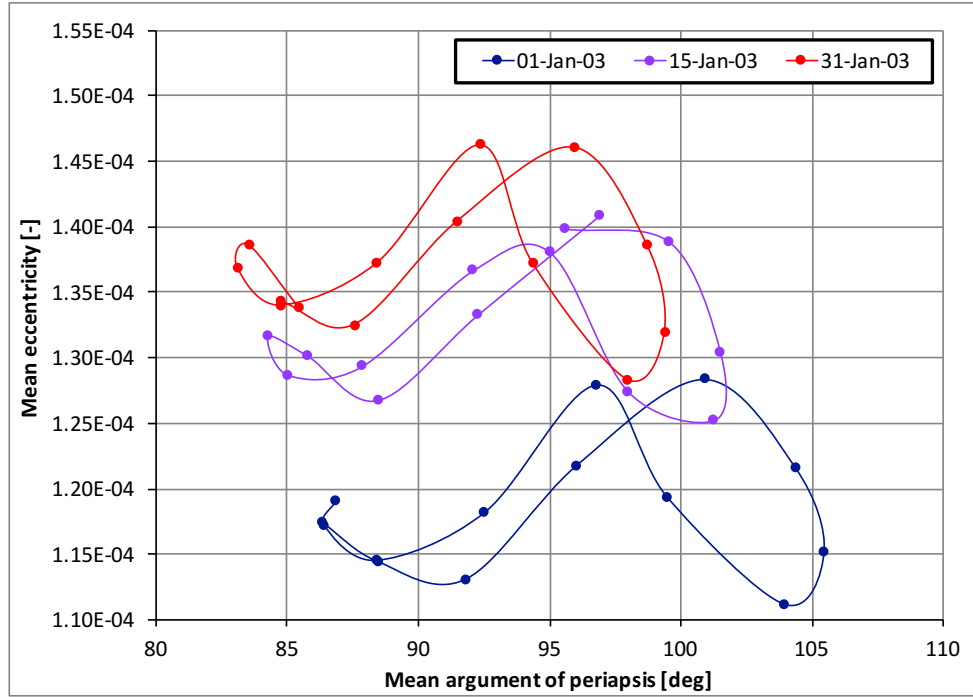


Figure 4.6: Behavior of \bar{e} and $\bar{\omega}$ on three days in January 2003, showing a daily repeating pattern in the mean elements. Each marker represents the mean elements for one complete revolution.

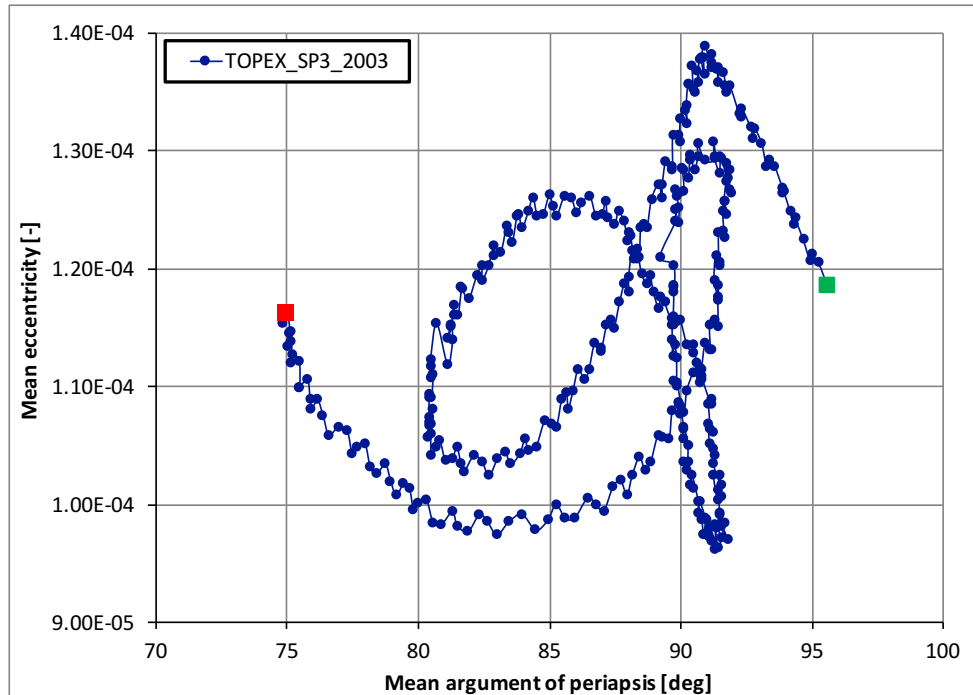


Figure 4.7: Behavior of \bar{e} and $\bar{\omega}$ for T/P throughout 2003. Each marker represents the reconstructed mean and subsequently one-day averaged \bar{e} and $\bar{\omega}$. The green and red marker depict the start and end time, respectively.

A clear difference between the behavior of ERS-2 and that of T/P is that for T/P there is more variation in the argument of periapsis, which swivels over an interval of more than 20 degrees in one year. One cause for this can be found in the very definition of the argument of periapsis - it marks the point in the orbit of closest approach to the orbited body, but in a near-circular orbit this point is ill-defined, which could explain some of the variation that is observed in Figure 4.7. Another cause lies in the algorithm that is used to convert osculating elements to mean elements (Section 5.2) in which it is assumed that the eccentricity has roughly the same order of magnitude as the J_2 coefficient, which is a more accurate assumption for ERS-2 than it is for T/P. In addition, as already mentioned, as T/P orbits close to the critical inclination, the frozen orbit may be less stable by itself as well. The zigzagging pattern, earlier observed for ERS-2, is visible here as well.

Being much less affected by drag than the lower orbiting ERS-2, the altitude of T/P is expected to be more stable and as a consequence show less reboosts. The plotted reconstructed mean semi-major axis, averaged over one-day periods, confirms this idea, as seen in Figure 4.8. It is noted that the reconstructed mean semi-major axis matches the target semi-major axis for T/P within centimeter accuracy (Section 2.3).

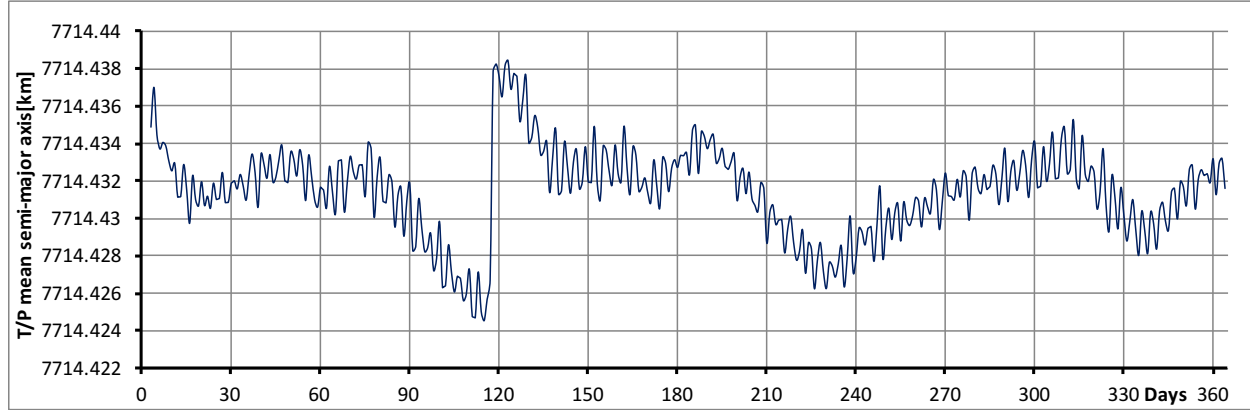


Figure 4.8: Daily-averaged reconstructed semi-major axis of T/P throughout 2004.

Methodology

One of the main goals of this work is to devise a numerical recipe for finding frozen orbit conditions. In order to do this, several techniques will have to be discussed and joined together. These techniques are numerical integration of the equations of motion for a satellite, reconstruction of mean elements from osculating elements, numerical averaging and numerical optimization.

The basis of the simulation will be a simulation to predict the trajectory of an hypothetical satellite through numerical integration (Section 5.1). From there on, the osculating predicted state history is transformed from osculating elements to mean elements through an algorithm based on the Eckstein-Ustinov theory (Section 5.2) and subsequent numerical averaging (Section 5.3). The reconstructed mean elements will serve as input for the objective function (Section 5.4), which lies at the heart of this work. The optimization problem will be solved using two optimization methods: grid searching and Differential Evolution (Section 5.5). A flowchart of the complete methodology can be found in Figure 5.1.

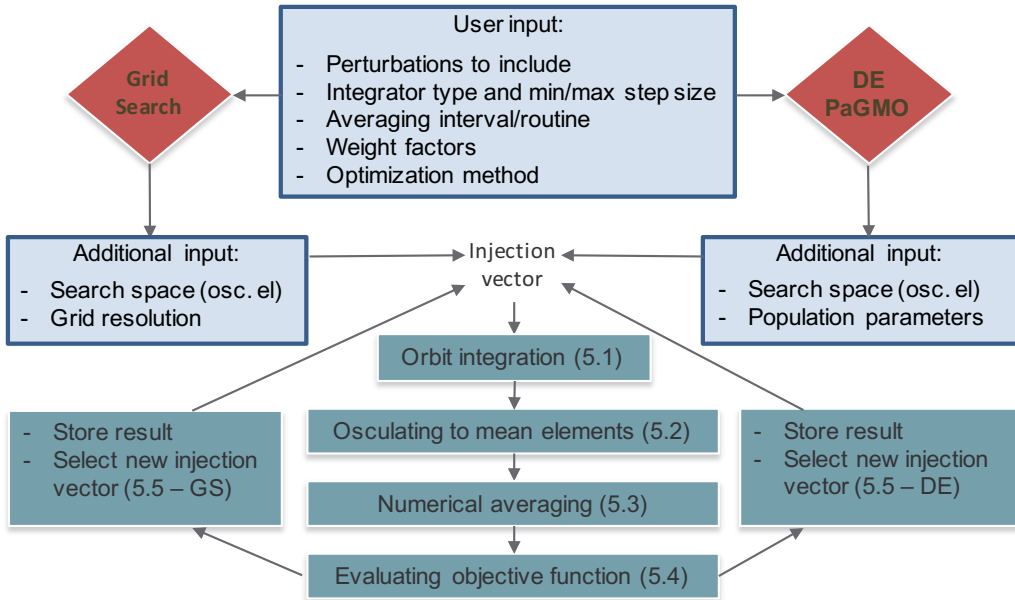


Figure 5.1: Flowchart of the procedure to identify frozen orbit conditions.

5.1 Numerical integration

The general equation for the two-body problem, Equation (3.1), can be written as a system of two ordinary first-order differential equations. In terms of state vectors, it may be written as

$$\mathbf{Y} = \begin{pmatrix} x \\ y \\ z \\ V_x \\ V_y \\ V_z \end{pmatrix} \rightarrow \dot{\mathbf{Y}} = \begin{pmatrix} V_x \\ V_y \\ V_z \\ a_x \\ a_y \\ a_z \end{pmatrix} = \begin{pmatrix} V_x \\ V_y \\ V_z \\ -\frac{\mu}{r^3}x \\ -\frac{\mu}{r^3}y \\ -\frac{\mu}{r^3}z \end{pmatrix} = \mathbf{f}(t, \mathbf{Y}) \quad (5.1)$$

where accelerations in the respective unit vector directions are denoted by a_x , a_y and a_z . Any other acceleration, such as those caused by perturbations, can easily be added to these components if transformed to the correct reference frame. In order to solve Equation (5.1) numerically, use can be made of several numerical integration methods. Within the field of astrodynamics, the (embedded) Runge-Kutta (RK) methods are well-known and frequently applied. [35]

Runge-Kutta methods

All methods in the RK family are based on the same general principle: multiple derivative evaluations along the integration time step from t_0 to $t_0 + \Delta t$. These derivative evaluations are then summed up in a weighted fashion, such that an accurate representation of the change in state \mathbf{Y} along the integration interval can be obtained. The number of derivative evaluations along the integration step is called the *order* of the RK method. [36] As an example, the well-known fourth-order RK method (abbreviated RK4) relies on four derivative evaluations along the integration timestep, as depicted in Figure 5.2.

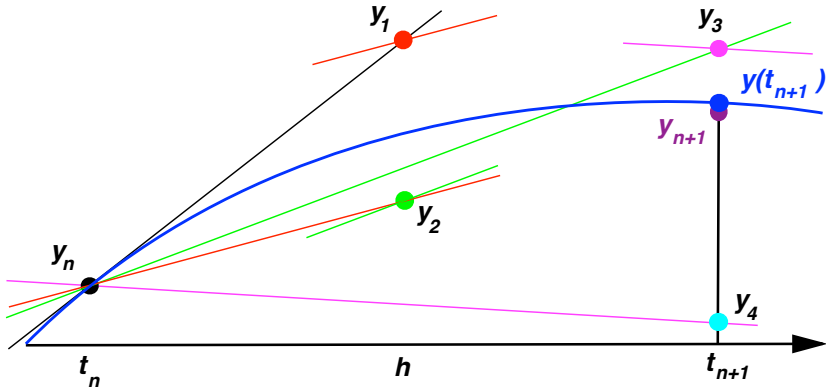


Figure 5.2: Representation of the RK4 method for a single-variable function.

In terms of accuracy, the RK4 method is comparable to that of a fourth-order Taylor approximation, but computation of the second, third and fourth order derivatives is not required, which makes it a computationally inexpensive method. The local truncation error (error due to one integration step) is bound by [25, 36, 37]

$$\varepsilon_{RK4} = (\Delta t)^5$$

where (Δt) is the step size. The classical RK4 method can be generalized to contain more slope evaluations within the integration interval. Adding more of these evaluations increases the accuracy of the method but logically increases computation time. Well-known higher-order RK methods are for example the fifth, eighth and thirteenth-order methods (RK5, RK8 and RK13).

A widely used adaptation of the RK methods comes in the form of *embedded methods*. For such methods, the outcome after each integration time step using an n^{th} order method is compared to the outcome of the same method in an $(n-1)^{th}$ method. It is then possible to impose a limit on the magnitude of the difference between these two methods, and to use this difference as a means of step size control. If a preset tolerance is not met, the integration step may be redone with a smaller step size. Embedded methods are usually denoted as **RKp(q)s**, where **p** denotes the primary order, **q** denotes the secondary order and **s** denotes the number of derivative evaluations per integration step. [25, 36]

Integrator selection

To investigate the stability and computation time of the numerical integration methods, a number of methods have been tested. The tested routines include the standard RK4 and RK8 method, as well as the embedded methods RK4(5), RK7(8) and RK8(7) (the latter one is known as Dormand-Prince). These methods are readily available in the software discussed further on in this chapter (Section 5.6).

The test deals with propagating the position of a satellite in Earth orbit, where all perturbations are assumed to be zero. In such a case, it is expected that the first five orbital elements remain static, eg. the orbit will be purely Keplerian. As the semi-major axis is directly related to the total orbital energy, it is expected to remain constant, as the total energy in a conservative force field should not change over time. As such, a test like this will yield some insight in the performance of a certain method. For this test, a point-mass satellite was inserted into a near-circular orbit ($e = 0.01$) at an altitude of 1000 km, with an inclination of 75 degrees. The position was subsequently propagated for 31 days, whilst the semi-major axis difference with respect to the original state vector was monitored. The completion time of the computation was also recorded. The results of this test are shown in Figure 5.3.

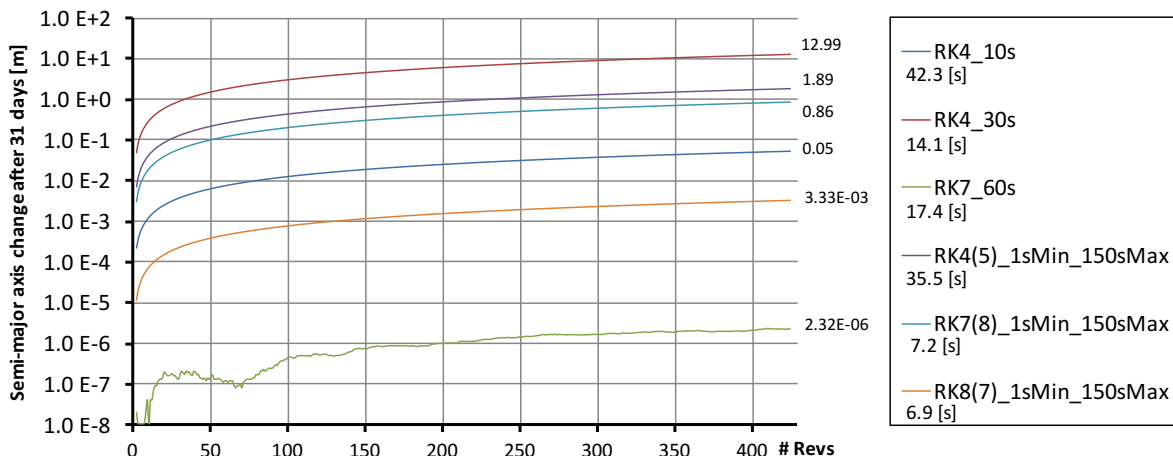


Figure 5.3: Performance of several RK methods for a near-circular low Earth orbit.

Clearly, the error for the RK8 method with a fixed step size at 60 seconds is the most accurate, but is more than twice as slow as its embedded companions RK7(8) and RK8(7). Though these later two methods are many orders of magnitude more inaccurate, their errors after quite an extensive integration period of 31 days can be called reasonable at least. It has to be noted, though, that even the least accurate of the methods, the RK4 method with a fixed step size of 30 seconds, boasts an accuracy that can be considered acceptable. But, considering all results, it is noted that the more accurate RK8(7) method is faster and therefore the integrator of choice for an orbit propagation *in this model for the dynamics*.

However, the choice for a variable step size integration method does not leave one free to just increase the maximum allowed step size provided that the tolerance criteria have been met. It should be noted that as the modeling environment becomes more complex, the reasoning behind the integrator selection in a simple central gravity field model no longer holds in its entirety. The use of a spherical harmonics gravity field leads to periodic effects in the orbital parameters, as shown earlier in Section 3.2. [28] These periodic effects have to be taken into account, as they are at the base of the secular effects that is vital to maintaining a frozen orbit. In addition, the other force models may induce errors when the maximum allowable step size is too large. It is therefore proposed to *fine-tune* the step size before each run with a new dynamics model, such that the step size can be maximized whilst still confined to within a certain error bound at the end of the integration interval.

5.2 Osculating to mean elements

Osculating orbital elements can be computed from a set of mean elements with relative ease by making use of the Lagrange equations (Equation (4.2)). Using the Lagrange equations to transform osculating elements to mean elements is more difficult. The inverse problem requires the use of an iterative procedure, which is explained in this section.

To convert osculating elements into mean elements, use is made of the Eckstein-Ustinov theory, which is based on the LPE's, but in a modified form in order to avoid problems due to singularities. Use is made of the following singularity-free elements: [38, 39]

$$\begin{aligned} a &= a \\ h &= e \cos \omega \\ l &= e \sin \omega \\ i &= i \\ \Omega &= \Omega \\ \lambda &= \omega + M \end{aligned} \tag{5.2}$$

where h and l are the x - and y -component of the eccentricity vector, respectively. It is possible to rewrite the LPE's in terms of these elements, after which they take the following form: [38, 40]

$$\frac{da}{dt} = \frac{2}{na} \frac{\partial \tilde{V}}{\partial \lambda} \tag{5.3a}$$

$$\frac{dh}{dt} = \frac{\sqrt{1-h^2-l^2}}{na^2} \left(\frac{\partial \tilde{V}}{\partial l} - \frac{h}{1+\sqrt{1-h^2-l^2}} \frac{\partial \tilde{V}}{\partial \lambda} \right) - \frac{l \cot i}{na^2 \sqrt{1-h^2-l^2}} \frac{\partial \tilde{V}}{\partial i} \tag{5.3b}$$

$$\frac{dl}{dt} = \frac{\sqrt{1-h^2-l^2}}{na^2} \left(\frac{\partial \tilde{V}}{\partial h} + \frac{l}{1+\sqrt{1-h^2-l^2}} \frac{\partial \tilde{V}}{\partial \lambda} \right) - \frac{h \cot i}{na^2 \sqrt{1-h^2-l^2}} \frac{\partial \tilde{V}}{\partial i} \tag{5.3c}$$

$$\frac{di}{dt} = \frac{\cot i}{na^2 \sqrt{1-h^2-l^2}} \left(l \frac{\partial \tilde{V}}{\partial h} - h \frac{\partial \tilde{V}}{\partial l} + \frac{\partial \tilde{V}}{\partial \lambda} \right) - \frac{\csc i}{na^2 \sqrt{1-h^2-l^2}} \frac{\partial \tilde{V}}{\partial \Omega} \tag{5.3d}$$

$$\frac{d\Omega}{dt} = \frac{\csc i}{na^2 \sqrt{1-h^2-l^2}} \frac{\partial \tilde{V}}{\partial i} \tag{5.3e}$$

$$\frac{d\lambda}{dt} = n - \frac{2}{na} \frac{\partial \tilde{V}}{\partial a} + \frac{\sqrt{1-h^2-l^2}}{1+\sqrt{1-h^2-l^2}} \frac{1}{na^2} \left(h \frac{\partial \tilde{V}}{\partial h} + l \frac{\partial \tilde{V}}{\partial l} \right) - \frac{\cot i}{na^2 \sqrt{1-h^2-l^2}} \frac{\partial \tilde{V}}{\partial i} \tag{5.3f}$$

It is emphasized that in Equation (5.3) the eccentricity no longer appears in any of the denominators, making the Eckstein-Ustinov theory valid for zero eccentricity. In addition, in these equations the short-periodic and long-periodic variations are developed to the second order. [38, 40] The complete expressions, for transforming mean elements to

$$\begin{aligned}
\Delta a &= -\frac{3\bar{a}}{2\lambda'} G_2 \left[\left(2 - \frac{7}{2}\bar{\beta}^2 \right) \bar{l} \cos \bar{\lambda} + \left(2 - \frac{5}{2}\bar{\beta}^2 \right) \bar{h} \sin \bar{\lambda} + \bar{\beta}^2 \cos 2\bar{\lambda} + \dots \right. \\
&\quad \dots \frac{7}{2}\bar{\beta}^2 (\bar{l}_0 \cos 3\bar{\lambda} + \bar{h} \sin 3\bar{\lambda}) \left. \right] + \frac{3\bar{a}}{4} G_2^2 \bar{\beta}^2 [7(2 - 3\bar{\beta}^2) \cos 3\bar{\lambda} + \bar{\beta}^2 \cos 4\bar{\lambda}] \\
\Delta h &= -\frac{3\bar{a}}{2\lambda'} G_2 \left[\left(1 - \frac{7}{4}\bar{\beta}^2 \right) \sin \bar{\lambda} + (1 - 3\beta_0^2) \bar{l} \sin 2\bar{\lambda} + \left(-\frac{3}{2} + 2\bar{\beta}^2 \right) \bar{h} \cos 2\bar{\lambda} + \dots \right. \\
&\quad \dots \frac{7}{12}\bar{\beta}^2 \sin 3\bar{\lambda} + \frac{17}{8}\bar{\beta}^2 (\bar{l} \sin 4\bar{\lambda} - \bar{h} \cos 4\bar{\lambda}) \left. \right] \\
\Delta l &= -\frac{3\bar{a}}{2\lambda'} G_2 \left[\left(1 - \frac{5}{4}\bar{\beta}^2 \right) \cos \bar{\lambda} + \frac{1}{2}(3 - 5\beta_0^2) \bar{l} \cos 2\bar{\lambda} + \left(2 - \frac{3}{2}\bar{\beta}^2 \right) \bar{h} \sin 2\bar{\lambda} + \dots \right. \\
&\quad \dots \frac{7}{12}\bar{\beta}^2 \cos 3\bar{\lambda} + \frac{17}{8}\bar{\beta}^2 (\bar{l} \sin 4\bar{\lambda} + \bar{h} \cos 4\bar{\lambda}) \left. \right] \\
\Delta i &= -\frac{3\bar{a}}{4\lambda'} G_2 \bar{\beta} \sqrt{1 - \bar{\beta}^2} \left[-\bar{l} \cos \bar{\lambda} + \bar{h} \cos \bar{\lambda} + \cos 2\bar{\lambda} + \frac{7}{3}(\bar{l} \cos 3\bar{\lambda} + \bar{h} \sin 3\bar{\lambda}) \right] \\
\Delta \Omega &= \frac{3\bar{a}}{2\lambda'} G_2 \bar{\beta} \sqrt{1 - \bar{\beta}^2} \left[\frac{7}{2}\bar{l} \sin \bar{\lambda} - \frac{5}{2}\bar{h} \cos \bar{\lambda} - \frac{1}{2} \sin 2\bar{\lambda} - \frac{7}{6}\bar{l} \sin 3\bar{\lambda} + \frac{7}{6}\bar{h} \cos 3\lambda_0 \right] \\
\Delta \lambda &= -\frac{3}{2\lambda'} G_2 \left[\left(10 - \frac{119}{8}\bar{\beta}^2 \right) \bar{l} \sin \bar{\lambda} + \left(\frac{85}{8}\bar{\beta}^2 - 9 \right) \bar{h} \cos \bar{\lambda} + \left(2\bar{\beta}^2 - \frac{1}{2} \right) \sin 2\bar{\lambda} + \dots \right. \\
&\quad \dots \left(-\frac{7}{6} + \frac{119}{24}\bar{\beta}^2 \right) (\bar{l} \sin 3\bar{\lambda} - \bar{h} \cos 3\bar{\lambda}) - \left(3 - \frac{21}{4}\bar{\beta}^2 \right) \bar{l} \sin \bar{\lambda} + \left(3 - \frac{15}{4}\bar{\beta}^2 \right) \bar{h} \cos \bar{\lambda} - \dots \\
&\quad \dots \frac{3}{4}\bar{\beta}^2 \sin 2\bar{\lambda} - \frac{21}{12}\bar{\beta}^2 (\bar{l} \sin 3\bar{\lambda} - \bar{h} \cos 3\bar{\lambda}) \left. \right]
\end{aligned} \tag{5.4}$$

where $G_2 = J_2(R_E/a)^2$, and

$$\lambda' = 1 - \frac{3}{2}G_2(3 - 4\beta), \quad \beta = \sin \bar{i}$$

after computation of the Δ -terms, the new elements can be computed as [38, 39]

$$\begin{aligned}
a &= \bar{a} + \Delta a \\
e &= \sqrt{l^2 + h^2} \quad \text{where } l = \bar{l} + \Delta l \quad \text{and } h = \bar{h} + \Delta h \\
i &= \bar{i} + \Delta i \\
\omega &= \text{atan2}(h, l) \\
\Omega &= \bar{\Omega} + \Delta \Omega \\
M &= \bar{\lambda} + \Delta \lambda - \omega
\end{aligned} \tag{5.5}$$

Whereas the expressions in Equation (5.4) deal with the transformation from mean elements to osculating elements, the inverse transformation is less straightforward. Numerical integration produces state vectors with osculating elements, and in order to transform these to mean elements, an iterative procedure is needed. [38, 39]

The iterative procedure commences by using the osculating elements as input for the right-hand side of Equation (5.4), after which the computed differences are added to the original input, constructing

a new set of elements, as in Equation (5.5). This new set is subsequently compared to the original set of osculating elements, both transformed to Cartesian coordinates. The transformation to Cartesian coordinates is necessary, as otherwise the inverse transformation overshoots and never reaches convergence. The difference between the original osculating state vector and the newly computed state vector is subsequently applied as a correction to the original input. [38, 39] This correction factor is multiplied with an attenuation factor to avoid overshoot. The entire process is repeated until the input of the transformation is such that the output matches the initial osculating elements. A schematic of the procedure is shown in Figure 5.4.

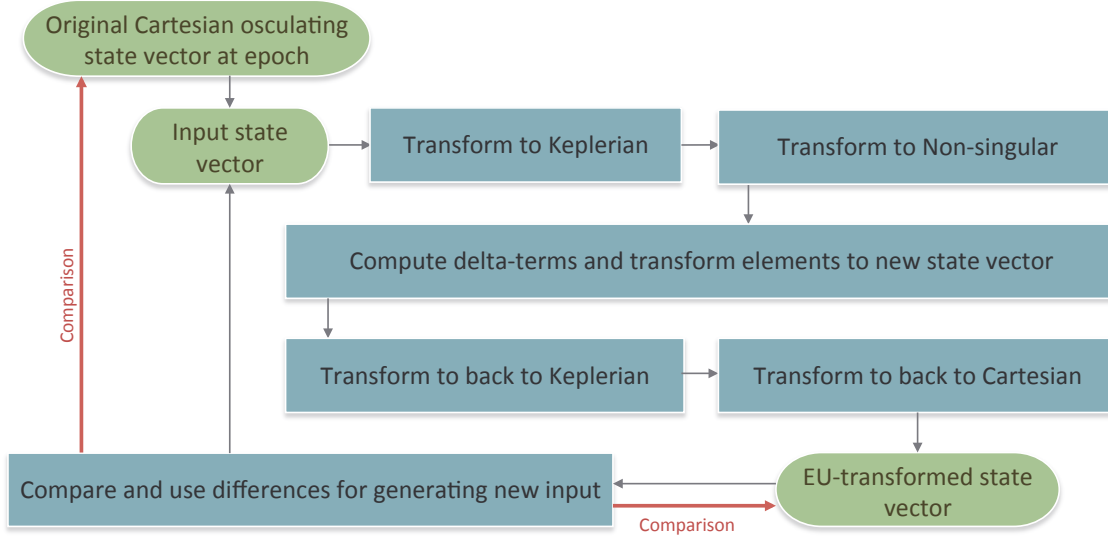


Figure 5.4: Iterative inverse Eckstein-Ustinov procedure.

This EU-reconstruction of mean elements is necessary as straightforward numerical averaging of osculating elements is *not* an accurate way of transforming osculating to mean elements. To illustrate this statement, the behavior of the osculating eccentricity of T/P in Figure 5.5 may be compared to its targeted design value of 0.000095. It is clear that simple numerical averaging alone would lead to biased values of the mean elements.

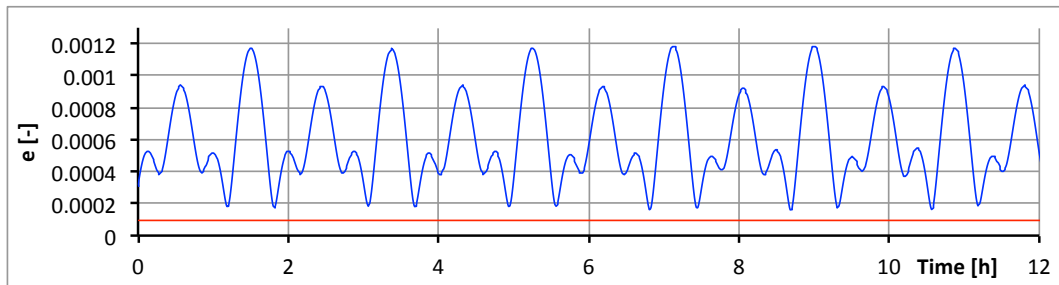


Figure 5.5: Osculating eccentricity of T/P as retrieved from POD data (blue) and the known mean eccentricity (red).

5.3 Numerical averaging

In order to gain insight in long-term behavior of satellites, it can be useful to shrink state vectors to more compact data sets by applying numerical averaging. In the C++ toolbox developed for this research, numerical averaging is applied in addition to the mean elements re-construction algorithm (Section 5.2). The combination of both numerical averaging and Eckstein-Ustinov's algorithm can provide accurate mean orbital elements for each revolution, as will be shown in Section 6.1.

When iterating through a state history, and using a fixed step size, the average of any element α is easily computed as [36]

$$\bar{\alpha}_{avg} = \frac{1}{N} \sum_{n=1}^N \alpha_n \quad (5.6)$$

where N denotes the number of elements and $\bar{\alpha}$ denotes the averaged element. When using a variable step size integration method, the average can be computed by a discretizing the definition of the function average, which is well-known from elementary calculus: [36]

$$\bar{\alpha}_{avg} = \frac{1}{t_2 - t_1} \int_{t_1}^{t_2} \alpha(t) dt \approx \frac{1}{t(n=N-1) - t(n=1)} \sum_{n=1}^{N-1} \alpha_n \Delta t \quad (5.7)$$

Care must be taken when determining the average of angular variables, such as the inclination, argument of periapsis, right ascension of the ascending node and the true/mean anomaly. If an angular variable changes from 2π to 0, straightforward numerical averaging can result in an average around π , whilst the true average lies around 0 or 2π . This can be solved by transforming the angles into unit vectors in x and y after which the averaged angle can be computed from the averaged vector spun up by x and y .

5.4 Objective function

The objective function, which lies at the very heart of this work, is to be a representation of the secular variation in mean orbital elements over a longer period of time. These changes in the orbital elements are what needs to be minimized to satisfy the definition of a frozen orbit. The proposed approach is to compare the reconstructed mean orbital elements of one orbit with those of the previous orbit, as in this way it is possible to quantify the secular variations. For N orbits, such an objective function would take the form of

$$F(\Delta\bar{a}, \Delta\bar{e}, \Delta\bar{i}, \Delta\bar{\omega}, \Delta\bar{\Omega}) = \frac{K}{N} \sum_{n=1}^{N-1} (k_a \cdot (\Delta\bar{a})_n + k_e \cdot (\Delta\bar{e})_n + k_i \cdot (\Delta\bar{i})_n + k_\omega \cdot (\Delta\bar{\omega})_n + k_\Omega \cdot (\Delta\bar{\Omega})_n) \quad (5.8)$$

where n is an orbit counter. k_α is a weight factor corresponding to orbital element α , and these weight factors are required to for normalizing the differences between orbital elements and their typical changes over one orbital period. K is an overall weight factor for cosmetic reasons. The delta-terms are defined as the difference between reconstructed mean orbital elements (as explained in Sections 5.2 and 5.3) for two consecutive orbits. So, for an arbitrary orbital element α :

$$(\Delta\bar{\alpha})_n = \text{abs}(\bar{\alpha}_n - \bar{\alpha}_{n+1}) \quad (5.9)$$

During the investigation of the behavior of ERS-2 and T/P in Section 4.3 it was noted that consequent averaging over the time it takes to complete one revolution does not fully cover the daily variation in the orbital elements. Therefore, to adapt to the routine of averaging over one-day time spans, N and n in Equation (5.8) can be changed into total number of days and day counter, respectively. This way, the daily variation will not cause a significantly large offset in the objective function value, as supported by the findings in Section 4.3.

As mentioned earlier in the report, the behavior of \bar{e} and $\bar{\omega}$ is particularly applicable. To specifically target an optimization for frozen orbits in terms of these two elements the weight factors k_a , k_i and k_Ω can be set to zero.

5.5 Optimization

The final element in the methodology is the optimization method that is to be used to minimize the objective function. Over the years, many of such methods have been devised, from very simple analytical approaches to complicated numerical algorithms. Two methods that have been extensively used in this work are the grid search and Differential Evolution (DE).

A **grid search** is one of the most straightforward optimization methods: each variable in the search space is divided into equidistant points, after which all possible combinations are evaluated. Subsequent analysis of the objective function values can be used to determine the global optimum, and can aid in determining the local optima. This method is also referred to as a 'brute-force' or 'exhaustive' search method. The main parameter that defines the grid search is the number of evaluations per control variable - increasing this number 'tightens' the grid and generally minimizes the error in determining the global minimum, at the expense of computational cost. The grid search is a very robust and simple method. It is also deterministic in the sense that (for a realistic number of function calls) whatever optimum it finds is generally in the vicinity of the real optimum. More advantages are that the objective function need not be differentiable and that the results are usually easy to plot and to interpret. A very significant drawback is the fact that the required number of objective function evaluations increases exponentially with the number of search variables, increasing the computation time to impossible lengths for multi-variable problems. [41]

Differential Evolution (DE) is an optimization algorithm based on genetic evolution found in nature ('survival of the fittest'). In this method, possible solutions to the objective function are called *individuals* - basically a vector with parameters. At the beginning of the optimization process, a set of random vectors is generated, and each of these vectors is evaluated in terms of their fitness level. Subsequently, the rules of evolution govern the optimization process: fitter individuals/vectors are more likely to produce offspring, while less fitter individuals/vectors die out, and occasional mutations can possibly benefit the population. In DE, the production of offspring is done by adding the weighted difference between two random vectors to a base vector, creating a mutant population which is then crossed with the original population. The mutant vectors are only accepted in the new generation if they have a better fitness level. [42] This process is repeated for a certain number of generations, or until a convergence criterion has been met. The process is explained in Figure 5.6. The DE algorithm will be the optimization method of choice for this work as it doesn't require a differentiable objective function and has a legacy of use in astrodynamics problems. [43]

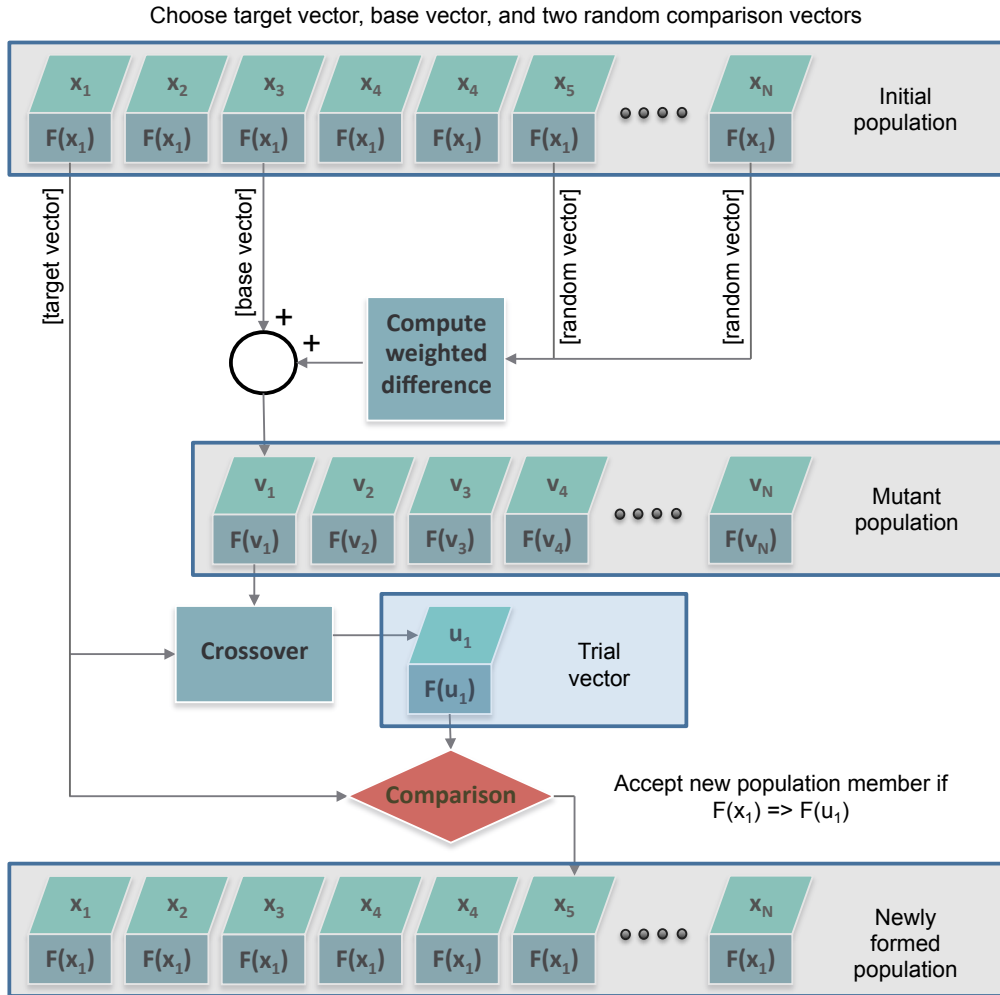


Figure 5.6: Flowchart explaining the basics of a Differential Evolution-based algorithm.

5.6 Software

A variety of software is required to model and solve an astrodynamics problem. Some software packages were reviewed in the literature survey which preceded this work, after which a selection was made on which to use. Only the used software is shortly discussed in this section.

The **TU Delft Astrodynamics Toolbox (Tudat)** is a set of C++ libraries providing users with the capability of simulating and solving various complex astrodynamics problems. The software was conceived in 2010 and the libraries remain in active development by staff and students of the Astrodynamics & Space Missions chair at the TU Delft. Tudat has no user interface, instead, users write their own C++ code that directly uses the libraries of C++. All of the source code is open-source, so modifications can be made if deemed necessary. The libraries are extensive and come with routines that can be directly applied to the problem addressed in this work. [44] Some routines that will be used from Tudat are:

- Numerical integrators → Runge-Kutta 4th order fixed-step (RK4)
- Numerical integrators → Runge-Kutta Dormand-Prince (RK8(7))
- Acceleration models → Central gravitational acceleration
- Acceleration models → Spherical harmonics gravitational acceleration
- Acceleration models → Third-body gravitational attraction
- Acceleration models → Cannonball aerodynamic drag acceleration
- Acceleration models → Cannonball solar radiation pressure acceleration
- Conversion routines → Conversion of Kepler elements to Cartesian coordinates and vice versa
- Input & output routines → Writing and handling of state vectors and state histories
- External → SPICE Interface & Reference frame transformations

Routines that were specifically developed during this work are:

- Eckstein-Ustinov transformation of osculating to mean Kepler elements and vice versa
- Numerical averaging of orbital elements
- Shadow function for radiation pressure
- Wrapper¹ for NRL-MSISE-00 atmosphere model

Tudat makes use of three external software libraries: **Eigen**, **Boost** and **SPICE**. The first adds extensive linear algebra functionality to the C++ language and the second one is a powerful set of libraries that provides support for more advanced tasks and structures, such as functions and unit testing.

The **SPICE** toolkit (Spacecraft Planet Instrument C-matrix Events) is a set of C libraries provided by NASA, which are extensively used for retrieving ephemerides, planetary body characteristics and transformations between reference frames. SPICE has been incorporated in Tudat as a wrapper, and the function calls for SPICE can be directly made in Tudat. The SPICE libraries contain *kernel files* which hold information on the relative positions and rotational states of bodies in the solar system. These libraries are of crucial importance to the simulations performed in this work, as they allow for:

- Retrieval of and transformation between Earth-centered co-rotating (ECR) and inertial (ECI) coordinates for the spherical harmonics gravitational acceleration.
- Retrieval of the relative positions of the Moon and the Sun for third-body gravitational accelerations.

The **Parallel Global Multi-Optimization toolbox (PaGMO)** is a bundle of global and local optimization algorithms written in C++. PaGMO was developed by the Advanced Concepts Team (ACT) of the European Space Agency (ESA). The software comes with an extensive library of global and local optimization methods, such as DE, GA, ant colony methods, simplex methods, particle swarm methods. In addition, the software is shipped with example problems to test the algorithms on. PaGMO's framework is designed to handle single- or multi-objective, continuous or integer, box-constrained or non-linear constrained, stochastic or deterministic optimization problems - covering

¹Developed by J. R. Hess

just about any optimization problem. The software has proven to be effective in some of the most difficult optimization problems in astrodynamics such as multiple flyby-trajectories with deep-space maneuvers and is used by ESA in editions of the Global Trajectory Optimization Competition (GTOC). [45, 46]

The simulation routine, the Eckstein-Ustinov routine, the averaging routines and the objective function evaluation are all paired and written as a PaGMO problem class, making PaGMoO the outer shell of the developed software.

Verification

In this chapter, the newly developed routines in the previous chapter are verified. The Eckstein-Ustinov algorithm, which lies at the core of the methodology presented in the previous chapter, is evaluated by reconstructing the known mean elements of T/P from osculating POD position solutions. The whole methodology presented in the previous chapter is verified by running the routine for a simple model and subsequent analysis of the known analytical solution of that simple model.

Routines that are part of Tudat, and have been extensively tested by staff and students of the TU Delft, will be accepted directly as verified methods. This includes numerical integration methods and perturbations methods.

6.1 Eckstein-Ustinov transformation

The transformation from osculating elements to mean elements, as described in Section 5.2, forms an integral part of the methodology introduced in Chapter 5. In order to verify the proper functioning and performance of the method, an osculating state vector from TOPEX/Poseidon was retrieved from POD SP3-files, dating 2 January 2002. [33] This state vector was transformed from a co-rotating reference frame to an Earth-centered inertial frame and subsequently propagated for one day. Included models are a gravity field model complete up to order and degree 60 and third-body accelerations due to the Moon and the Sun (the same models as in [38], to allow for further verification). Finally, the resulting osculating state histories are transformed back to mean elements through the Eckstein-Ustinov algorithm. The results for the altitude, eccentricity and argument of periapsis are shown in Figures 6.1 to 6.3. The reference values for TOPEX/Poseidon, as given in Section 2.3, are $\bar{h} = 1336.293$ km, $\bar{e} = 0.000095$, and $\bar{\omega} = 90.0$ degrees.

From the three graphs, it can be concluded that indeed the Eckstein-Ustinov routine provides good results, especially for the semi-major axis and the eccentricity. Further numerical averaging of one-orbit intervals produces well matching mean elements - within less than 1 meter in the semi-major axis, and 10^{-6} for the eccentricity. The mean argument of periapsis is not re-constructed so accurately, but for such low values of the eccentricity this is understandable. In addition, the frozen orbit of TOPEX/Poseidon is situated near the critical inclination, where the effects of smaller perturbations take over as J_2 cancels out, thus making the orbit less stable. A more stable example would be ERS-2, for which position data is also available, and these data have been converted to mean elements earlier in this work (Section 4.3). The reconstructed mean eccentricity and mean

argument of periapsis match with the known values for ERS-2, further strengthening the confidence in the combination of Eckstein-Ustinov and numerical averaging.

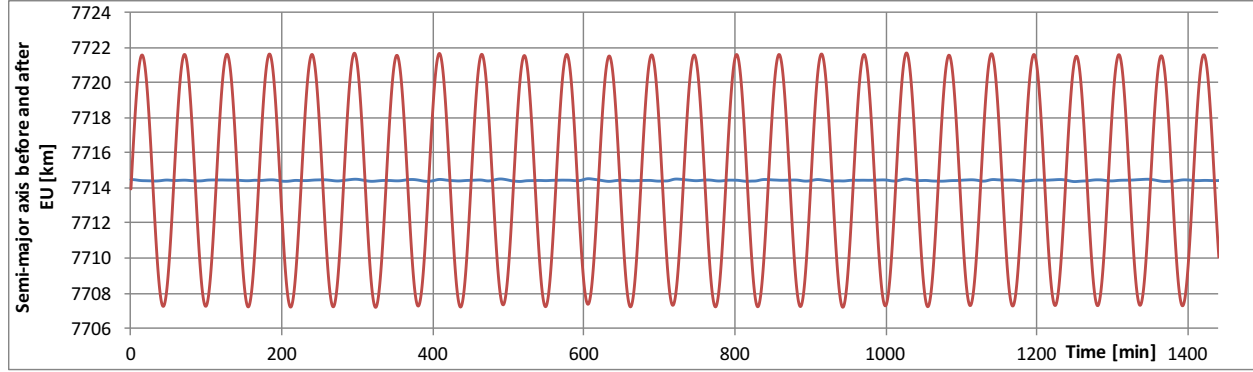


Figure 6.1: Eckstein-Ustinov reconstructed mean semi-major axis of T/P (blue) compared to the osculating element(red).

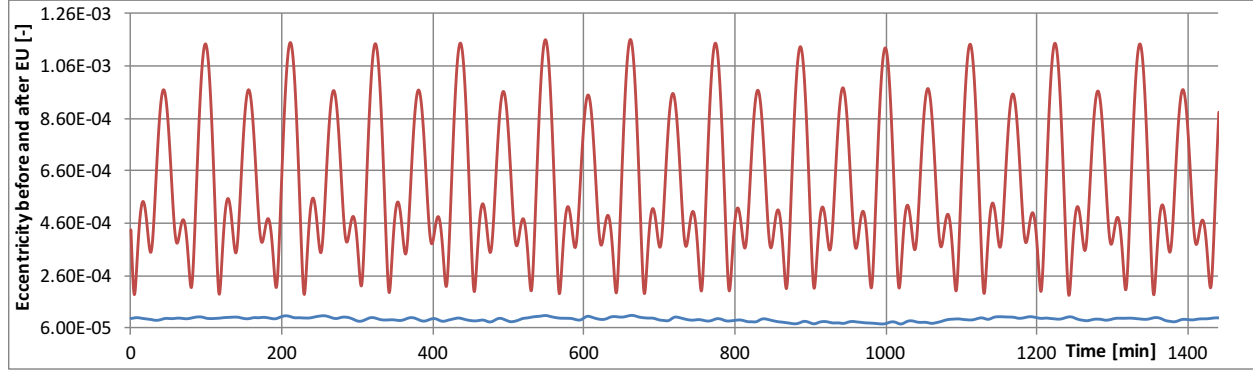


Figure 6.2: Eckstein-Ustinov reconstructed mean eccentricity of T/P (blue) compared to the osculating element (red).

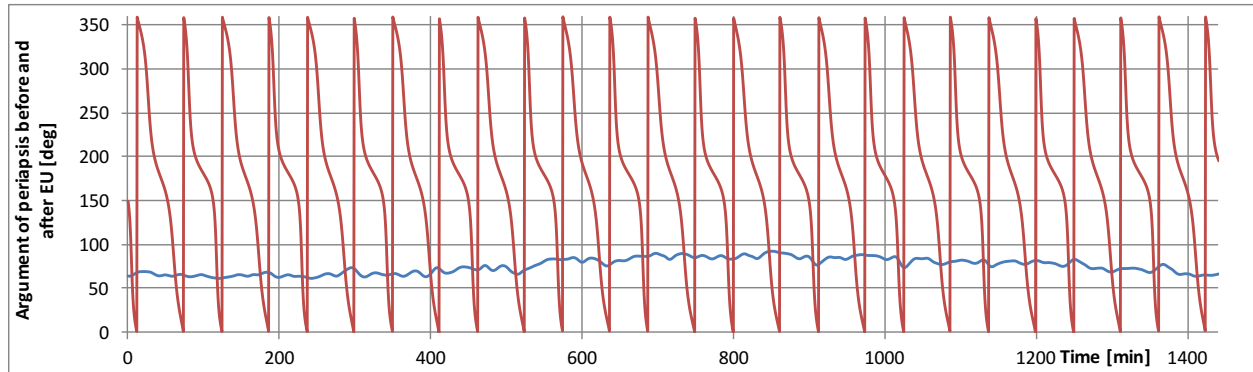


Figure 6.3: Eckstein-Ustinov reconstructed mean argument of periapsis of T/P (blue) compared to the osculating element (red).

6.2 Global verification

In order to test whether the combination of numerical propagation, Eckstein-Ustinov transformation from osculating to mean elements, numerical averaging and optimization methods can find the injection conditions for an actual frozen orbit, a global verification method is required. To verify all the used methods in Chapter 5 at once, an optimization problem is established in a simple dynamics model where only J_2 and J_3 are included. Recall from Chapter 4 that the eccentricity, semi-major axis and inclination are bound by the relation

$$\bar{e} = -\frac{J_3 R_E}{2 J_2 \bar{a}} \sin \bar{i} \quad (6.1)$$

With this in mind, a search space is set up for the osculating elements during injection. For this test it is assumed that the orbital elements a , i , Ω and θ are known at the moment of insertion, thus limiting the search space to ω and e . All in all, the parameters for this grid search are set to:¹

$a =$	$R_E + 1000.0$	[km]	$k_a =$	0.0
$e =$	$[0.0 : 0.0002 : 0.005]$	[-]	$k_e =$	1.0
$i =$	98.549	[deg]	$k_i =$	0.0
$\omega =$	$[0.0 : 0.1 : 6.2]$	[rad]	$k_\omega =$	1.0
$\Omega =$	255.842	[deg]	$k_\Omega =$	0.0
$\theta =$	179.91	[deg]	$K =$	10.0

Assuming that the fixed osculating elements a and i are equal to the mean elements (which they are not, but it is a starting point) Equation (6.1) yields a frozen mean eccentricity of $\bar{e} = 9.99804 \cdot 10^{-3}$. The search space for the osculating eccentricity is built around this value with a good margin, as the difference between osculating and mean eccentricity can be large (Figure 5.5). The results of the grid search, and a subsequent DE run, are shown in Figures 6.4 and 6.5, respectively.

¹The notation $[0 : 1 : 10]$ corresponds to the interval from 0 to 10 being sampled in steps of 1.

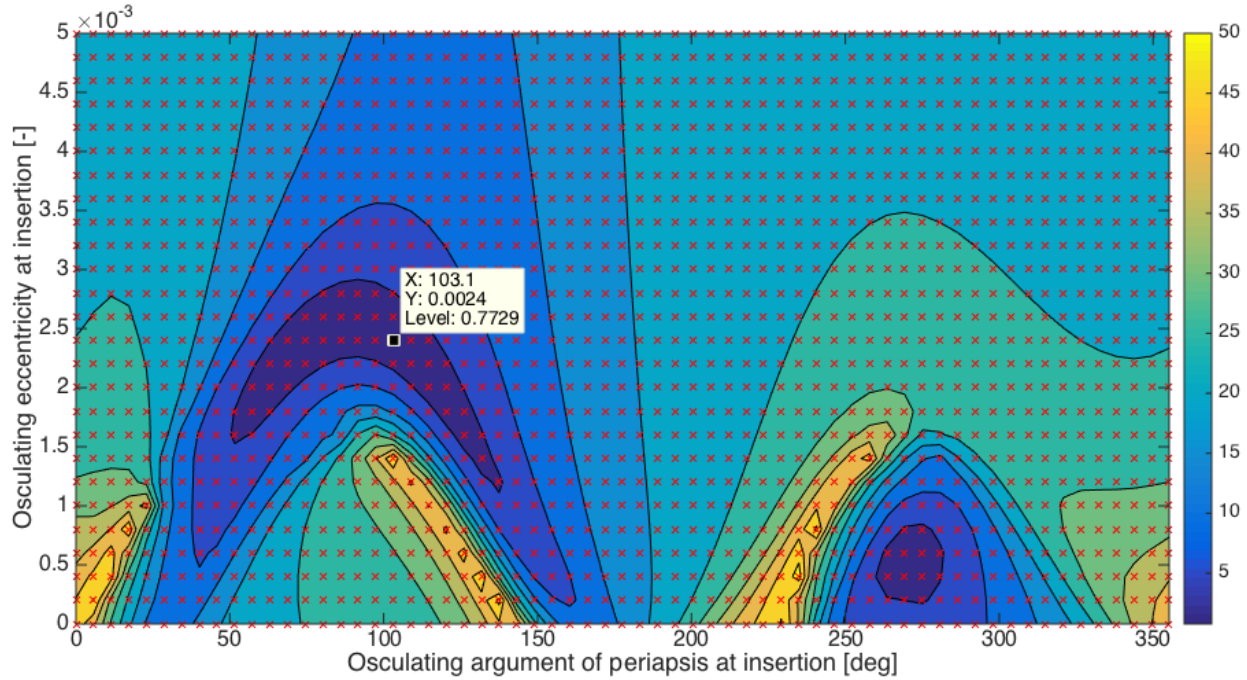


Figure 6.4: Grid search in a search space spun up by osculating elements e and ω in a J_2-J_3 model.

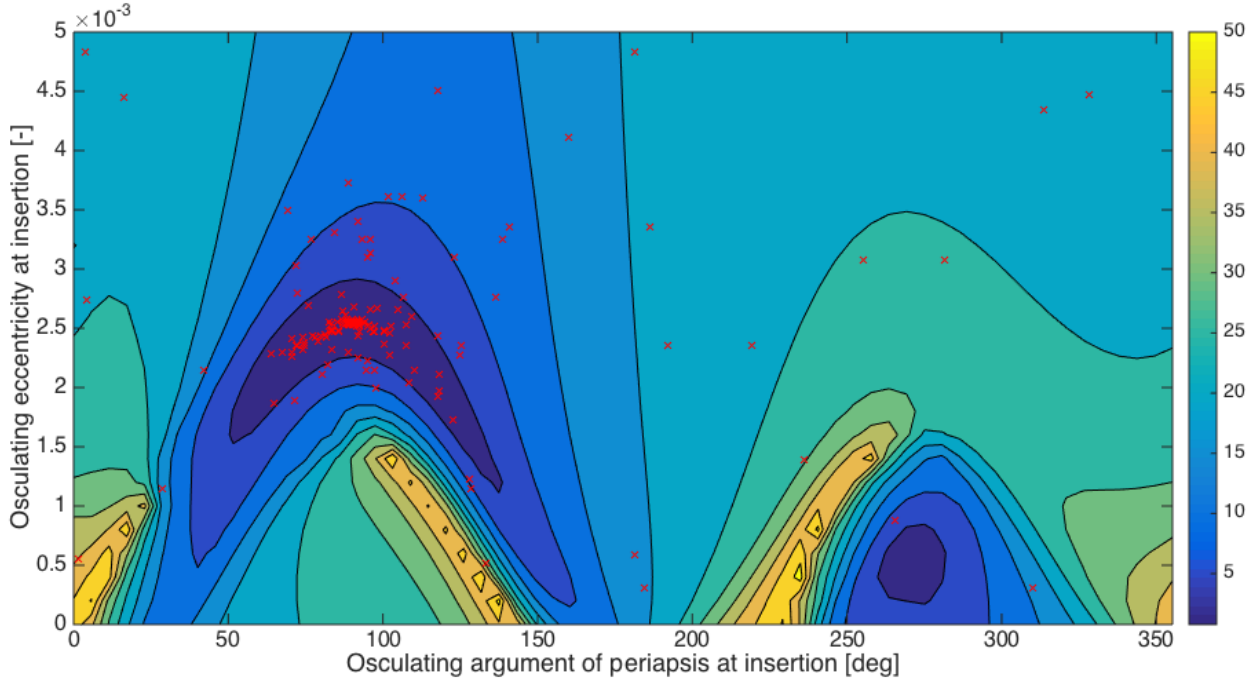


Figure 6.5: Grid search in a search space spun up by osculating elements e and ω in a J_2-J_3 model, overlaid with points which were evaluated by a DE algorithm.

Clearly, the grid search provides a good overview of the search space in this two-dimensional problem. The lowest possible objective function is found for $e = 0.0024$ and $\omega = 103.1$ degrees. However, the grid search is not meant to find a converged solution - that is where DE kicks in, which identifies the optimum at the point $e = 0.0026689$ and $\omega = 89.31$ degrees. This osculating eccentricity does not correspond at all to the expected mean frozen eccentricity, but evidently the injection conditions have to be transformed to mean elements first. This is done by propagating the osculating injection state vector for two years in the same dynamics model in which it was found, after which the found osculating state history is transformed to mean elements and subsequently averaged. The results are shown in Figure 6.6.

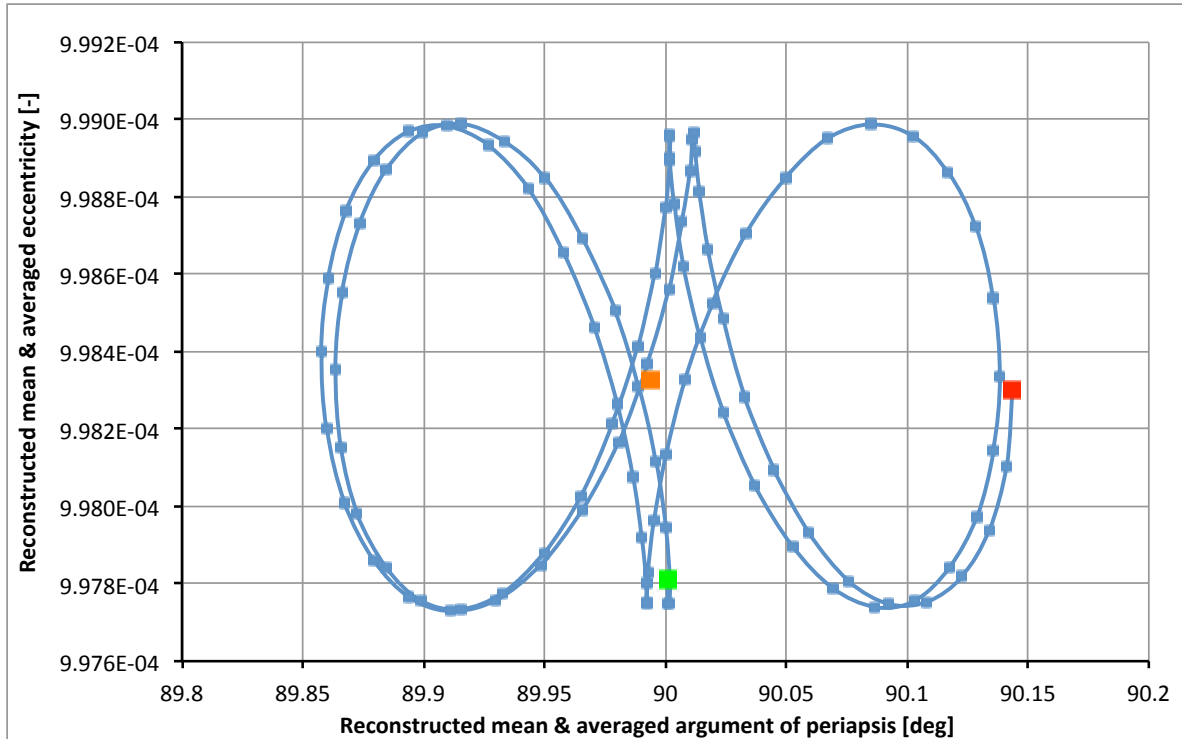


Figure 6.6: Mean elements ω and e resulting from numerical propagation of the DE optimum in a J_2 - J_3 model. Start, end and average value are marked with green, red and orange points, respectively. Between consecutive markers is a 1-week interval.

The behavior of \bar{e} and $\bar{\omega}$ corresponds well with what is expected for a frozen orbit: the variations in both are small and seem to fall into a repetitive pattern. For the two-year averages of the mean elements, it is found that $\bar{e}_a = 9.98329 \cdot 10^{-4}$ and $\bar{\omega}_a = 89.993$ degrees. The mean argument of periapsis is right on target with the analytical solution, but the eccentricity is a bit off, which is likely caused by the earlier assumption that the osculating semi-major is equal to the mean elements, which it is not, as shown in Figure 6.7.

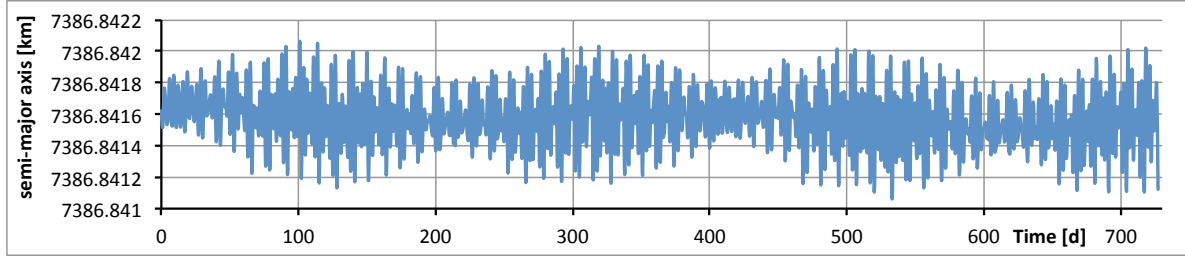


Figure 6.7: Behavior of the mean semi-major axis.

For the averaged value over the two-year propagation period, it is found that $\bar{a}_{num} = 7386.8416$ km. This reasoning for a also applies for the inclination, for which it is found that $\bar{i}_{num} = 98.6462$ degrees. After this necessary iteration, it can be found that $\bar{e}_a = 9.98398 \cdot 10^{-4}$, which closely matches the two-year average mean eccentricity found by the numerical method ($\bar{e}_{num} = 9.98329 \cdot 10^{-4}$). This result provides a complete verification of all the steps in the new method.

In this verification, optimization was performed by using the standard PagMO DE algorithm with a weight coefficient $f = 0.8$, a crossover probability $c_r = 0.9$. The population size was 20 (10 times the number of free variables [47]) and 100 generations were evaluated. Convergence was reached quickly within 40 generations - significantly quicker than the more challenging problems evaluated in the next chapter.

Results

In Chapter 5, the reasoning and methodology behind a numerical method for finding frozen orbits were discussed, and the performance of that method was subsequently investigated in Chapter 6. In this chapter, this numerical recipe is used to find frozen conditions for a hypothetical mission, for which the details and assumptions are first listed in Section 7.1. From here, the method is used in models of increasing complexity, starting with zonal geopotentials of increasing degree in Section 7.2, after which the stability of the found orbit is assessed over a period of two years. Subsequently, the effect of other perturbations (tesseral terms, drag, third-body gravity and radiation pressure) on that stability are investigated in Section 7.3, and an attempt is made to incorporate these other perturbations in the design process. Finally, the method is used to design a frozen orbit in a realistic set of orbital dynamics models, including all the relevant perturbations, in Section 7.4.

7.1 Assumptions

The results presented in this chapter are based on the hypothetical launch of an ‘ERS-2-type’ satellite in a frozen orbit. The physical characteristics of this satellite, which are assumed to remain constant throughout each simulation, are chosen to be identical to the actual design values for ERS-2. The satellite surface area is estimated from physical dimensions and typical satellite attitude (eg. solar arrays always pointing towards the Sun, and the satellite flying in a fixed orientation with respect to the ground). The physical characteristics are chosen as shown in Table 7.1.

mass (m)	fixed	2516.0	[kg]
surface area (drag) (S_D)	fixed	25.0	[m ²]
surface area (radiation pressure) (S_R)	fixed	35.0	[m ²]
drag coefficient (C_D)	fixed	2.2	[\cdot]
reflection coefficient (C_R)	fixed	0.23	[\cdot]

Table 7.1: Details for the ‘ERS-2’ type satellite used in this chapter.

With the physical parameters defined, a search space has to be defined for the optimization. There are seven important injection parameters: six state indices (Kepler elements) and the time of insertion. During the optimization process, three of those parameters are assumed to be variable: the semi-major axis, the eccentricity and the argument of periapsis (all of them osculating). The others are assumed constant, and together the constant and variable injection parameters are shown in Table 7.2.

semi-major axis (a)	free	$[R_E + 980.0 : R_E + 1020.0]$	[km]
eccentricity (e)	free	$[0.0 : 0.008]$	[\cdot]
argument of periapsis (ω)	free	$[0.0 : 359.99]$	[deg]
inclination (i)	fixed	86.0	[deg]
R.A.A.N. (Ω)	fixed	270.0	[deg]
true anomaly (θ)	fixed	180.0 (at apoapsis)	[deg]
time of injection (t)	fixed	2457998.0 (1 Sep 2017, noon UTC)	[JD]

Table 7.2: Search space of osculating elements and time at injection. [48]

Run-time of the integration routine for each objective function evaluation is 10.05 days (to ensure that at least the differences in orbital elements over 10 consecutive days are included). In some cases, the integration period is increased to improve the quality of the results. The **maximum allowed step size** is determined both automatically by the relative and absolute tolerance of the variable step size RK8(7) integrator (being 10^{-10} and 10^{-12} , respectively), as well as manually by the complexity of the model. The maximum step size is chosen such that at the end of a 10.05 day integration run, the Cartesian position error does not exceed 25 m with respect to a very short step size (3 s) integration run.

For all optimization runs, a population of 30 individuals (10 times the number of decision variables [47]) is initialized randomly within the search space. This population is evolved over the course of 250 generations. The whole process is repeated until a total of three runs has been completed, which satisfy the following convergence criteria:

- The objective function value must not have decreased in the final 50 generations of the optimization routine.
- The final objective function value at the end of each run must be within a 5% range of the other runs.
- The final spread in final injection parameters must be significantly less than what a modern launch vehicle can achieve in terms of injection accuracy.

After each run, the first two criteria are easily verified, but for the third one a general idea about launcher injection accuracy is required. In this work, the injection conditions will be compared with the injection accuracy of an Arianespace-built Soyuz ST launch vehicle. The 1σ -values for this launcher, for a typical scenario of a satellite in a circular orbit at mean altitude of 1000 km, are shown in Table 7.3

Parameter	1σ -value
a [km]	3.3
e [\cdot]	0.00066
i [deg]	0.033
Ω [deg]	0.05

Table 7.3: Injection accuracy for a Arianespace-built Soyuz launcher. [48]

7.2 Zonal geopotential

Up to degree 3

The starting problem will be a simple one - for this problem, a model is considered that only takes into account the first two zonal coefficients of the spherical harmonics expansion. This problem is identical to the verification problem in Chapter 6, but in this case the semi-major axis at injection is free (yet bounded), hence the search space becomes three-dimensional. The evolution of the objective function as optimized by DE is shown in Figure 7.1.

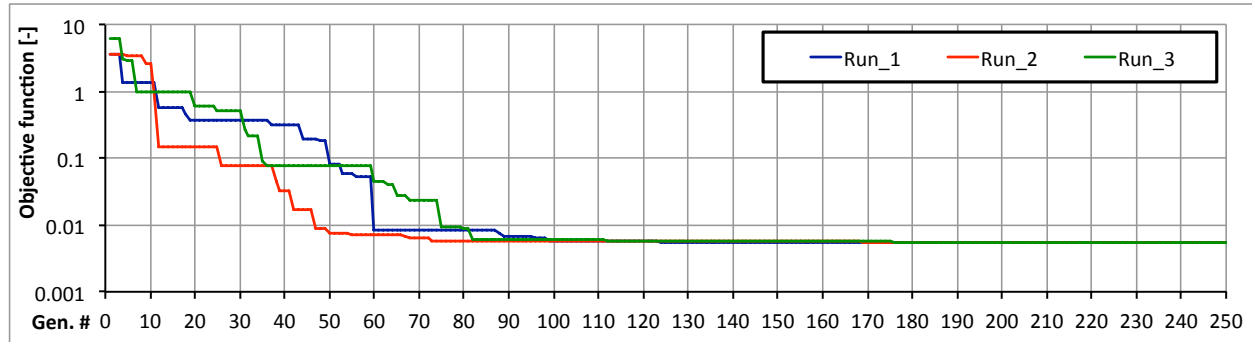


Figure 7.1: Objective function value for J_3 zonal geopotential.

As apparent from Figure 7.1, the objective function drops to an apparent minimum over the course of the optimization process. Throughout the first generations, relatively large jumps bring the objective function value closer to the apparent minimum, and in the later generations the solution is fine-tuned, leading to static behavior of the objective function value in the last 70 generations. This means that the first convergence criterion is met. The resulting initial conditions are shown in Table 7.4.

J₃	Run 1	Run 2	Run 3	Resulting mean el.
F [-]	0.005493	0.005480	0.005410	
a [km]	7380.979	7381.096	7380.705	$\bar{a} = 7389.543$
e [-]	0.002605428	0.002605327	0.002605590	$\bar{e} = 0.00100723$
ω [deg]	89.98480	90.00728	89.97279	$\bar{\omega} = 90.011$

Table 7.4: Optimized injection elements and resulting mean elements in a zonal geopotential of degree 3.

From Table 7.4, it becomes apparent that the second convergence criterion has been met as well, as the objective function values are within a 3% range of each other. The third criterion is also easily satisfied when compared with the injection accuracy presented in Table 7.3. In fact, the found injection conditions are much more precisely defined than what any launcher to date has achieved. This begs the question of what the influence of injection errors will be on the final stability of the frozen orbit, and this question is answered later in this chapter.

With the injection conditions in Table 7.4 (of course, using the best result, highlighted in green) it is possible to evaluate the stability of the found frozen orbit over a longer term than the original 10-day integration interval used in the optimization process. In order to do this, the injection state vector is numerically propagated and the resulting osculating elements are transformed to mean elements through EU, just as in the optimization process. Figure 7.2 shows the resulting behavior of \bar{e} and $\bar{\omega}$ over a period of two years.

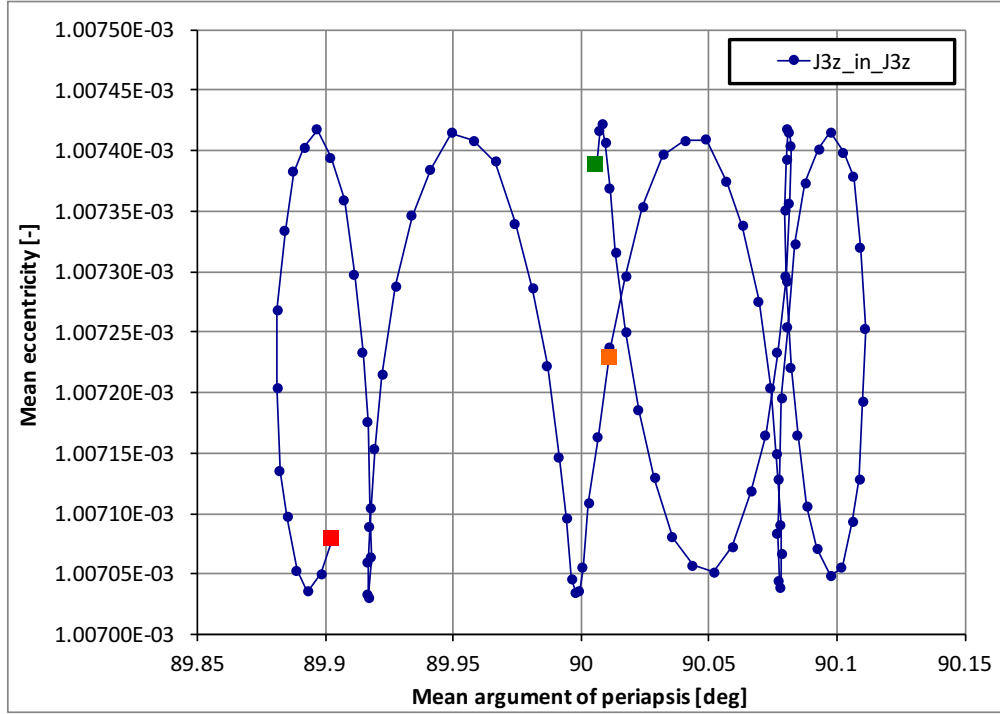


Figure 7.2: Evolution of \bar{e} and $\bar{\omega}$ found by propagating the J_3 -optimal injection conditions in the same J_3 geopotential, for a period of two years. Green, red and orange marks depict the start, end and averaged value, and the time between two marks is 1 week.

The mean values for \bar{e} and $\bar{\omega}$ during the complete two-year integration period in Figure 7.2 are $\bar{e} = 0.0010072$ and $\bar{\omega} = 90.011$ degrees. This result corresponds well to the analytic solution that can be obtained by Equation (4.5). It is noted that the variation of \bar{e} and $\bar{\omega}$ in Figure 7.2 is small: the total variation in \bar{e} does not exceed $\Delta\bar{e} = 5 \cdot 10^{-7}$ and the total variation in $\bar{\omega}$ is limited to less than $\Delta\bar{\omega} = 0.25$ degrees. The variation in the semi-major axis is limited to within a 2-meter interval, and carries a mean value of 7389.543 km (not plotted). Despite the small variations, a librating motion can still be observed, which bears similarities with the simpler problem evaluated in Chapter 6. Logically, the variation in the elements right after the injection is smallest, as the optimization is only concerned with the first ten days.

However, when propagated in more realistic geopotential models, it becomes apparent that the solution found in the simple third-degree geopotential model falls short. In Figure 7.3 the injection parameters from the third-degree zonal geopotentials models are propagated in a 10-degree and 25-degree zonal models, clearly showing a much more significant variations in the evolution of \bar{e} and $\bar{\omega}$. This increased variation illustrates the need for finding a optimal solution in a more sophisticated model. The motion of \bar{e} and $\bar{\omega}$ librates around the actual frozen values in the counter-clockwise

direction, and as such the simple optimized solution exhibits *quasi-frozen* in the more realistic models. It is expected that the new solution should be in the center of the librating motion found for \bar{e} and $\bar{\omega}$ in Figure 7.3.

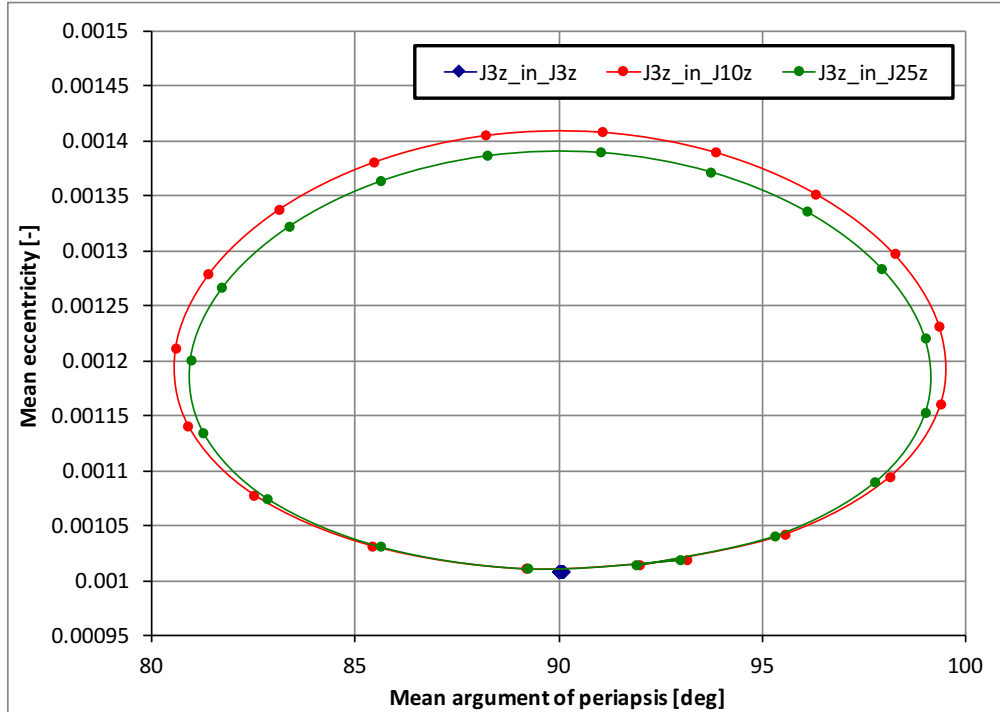


Figure 7.3: Evolution of \bar{e} and $\bar{\omega}$ found by propagating the J_3 -optimal injection conditions in higher degree zonal geopotentials, for a period of 19 weeks (equal to the period of the librating motion). Green, red and orange marks depict the start, end and averaged value, and the time between two marks is 1 week.

Up to degree 10

Now, a more complex model zonal geopotential model is used to find optimal injection conditions. Subsequently, the stability is assessed over a longer period in the same manner as in the last paragraph. From the evolution of the objective function, as shown in Figure 7.4, it is clear that the first convergence criterion has been met.

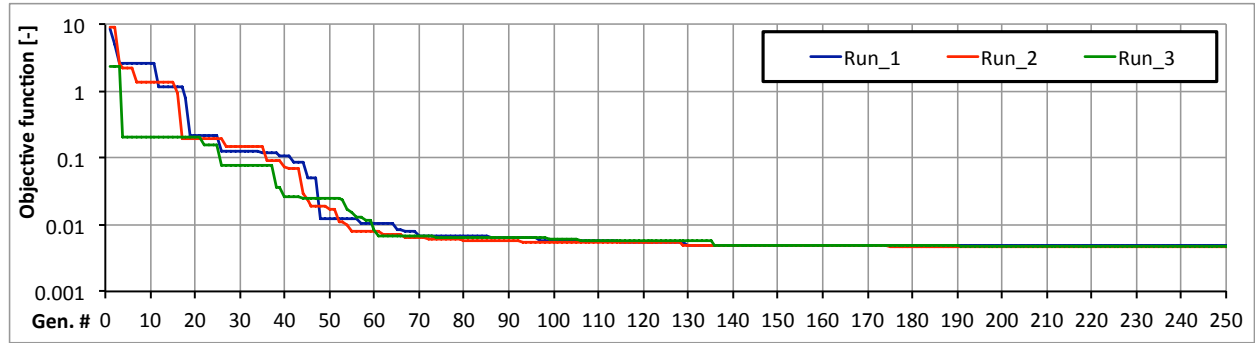


Figure 7.4: Objective function value for J_{10} zonal geopotential model.

The resulting initial conditions are shown in Table 7.5. From that table, it can be seen that the second and third convergence criterion have been met as well for this optimization run, as the objective function values are within a 5% range, and the injection parameters range within the launcher 1 σ value.

J₁₀	Run 1	Run 2	Run 3	Resulting mean el.
<i>F</i> [-]	0.004840	0.004679	0.004757	
<i>a</i> [km]	7358.196	7358.685	7358.779	$\bar{a} = 7367.100$
<i>e</i> [-]	0.002821422	0.002820874	0.002821088	$\bar{e} = 0.001214977$
ω [deg]	89.96955	89.97526	89.97875	$\bar{\omega} = 90.011$

Table 7.5: Optimized injection elements and resulting mean elements in a zonal geopotential of degree 10.

Subsequent long-term numerical propagation of the best injection conditions from Table 7.5 leads to an almost identical pattern as shown in Figure 7.2. The total variation in $\bar{\omega}$ remains nearly the same, whereas the variation in \bar{e} has become 10 times larger with respect to the J_3 -case at $\Delta\bar{e} = 5 \cdot 10^{-6}$. The average mean eccentricity has increased with about 20%, leading \bar{e} and $\bar{\omega}$ now to carry the following values: $\bar{e} = 0.0012150$ and $\bar{\omega} = 90.011$ degrees. The semi-major axis at injection found by the optimization results in a mean semi-major axis of 7367.099 km, which is significantly lower than the result obtained for the J_3 case. As \bar{a} is significantly different from the previous case, the direct comparison for the increase in \bar{e} with respect to the previous case is not fully legitimate, but nevertheless satisfies the tendency earlier observed in Figure 4.2.

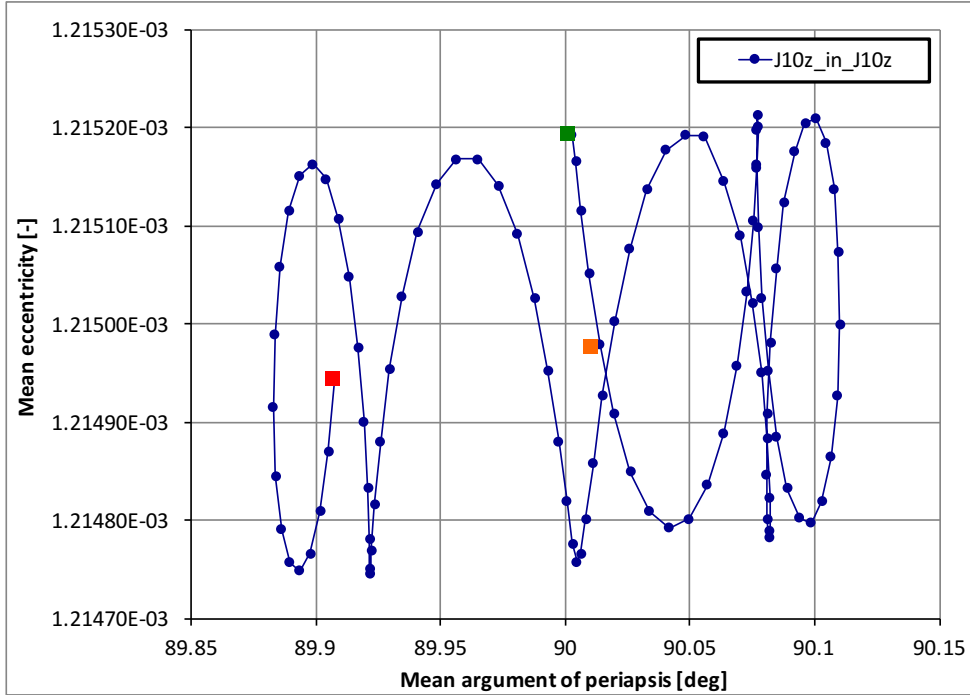


Figure 7.5: Evolution of \bar{e} and $\bar{\omega}$ found by propagating the J_{10} -optimal injection conditions in the same J_{10} geopotential, for a period of two years. Green, red and orange marks depict the start, end and averaged value, and the time between two marks is 1 week.

Up to degree 25

The final zonal model to be used for finding optimal injection conditions will be a geopotential complete up to degree 25. As in the previous paragraph, the evolution of the objective function, the initial conditions and the long-term stability are shown. Now, a more complex model zonal geopotential model is used to find optimal injection conditions. Subsequently, the stability is assessed over a longer period in the same manner as in the last paragraph. From the evolution of the objective function, as shown in Figure 7.4, it is clear that the first convergence criterion has been met.

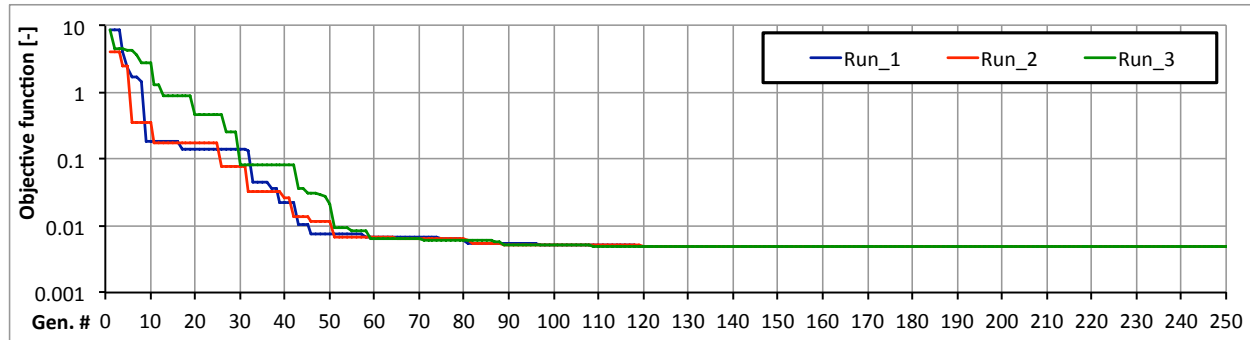


Figure 7.6: Objective function value for J_{25} zonal geopotential model.

From Figure 7.4, it is clear that no changes in the objective function have occurred in the final 50 generations of the optimization run. In addition, the obtained injection parameters in Table 7.6 are within the achievable accuracy shown in Table 7.3.

J₂₅	Run 1	Run 2	Run 3	Resulting mean el.
F [-]	0.004795	0.004809	0.004783	
a [km]	7358.367	7358.367	7358.368	$\bar{a} = 7367.250$
e [-]	0.002811873	0.002811796	0.002811902	$\bar{e} = 0.001205497$
ω [deg]	89.95373	89.95726	89.94904	$\bar{\omega} = 90.011$

Table 7.6: Optimized injection elements and resulting mean elements in a zonal geopotential of degree 25.

The long-term behavior of \bar{e} and $\bar{\omega}$, integrated in the same model as where the injection conditions were found, is shown in Figure 7.7. Again, the pattern resembles the behavior of \bar{e} and $\bar{\omega}$ in the two previous cases. The range in values for the mean argument of periapsis remains the same at about 0.25 degrees, and the range for the eccentricity has increased marginally to $\Delta\bar{e} = 6 \cdot 10^{-6}$ with respect to the J_{10} case.

It is noted that the two-year averaged mean eccentricity of Figure 7.7 ($\bar{e} = 0.001205497$) in this J_{25} -model matches the mean eccentricity that can be found in Figure 4.1, which is for the case of a zonal model complete up to degree 50. It is therefore observed that the found mean eccentricity in this case and the previous two cases converge to the value that can be found by inspecting Figure 4.1.

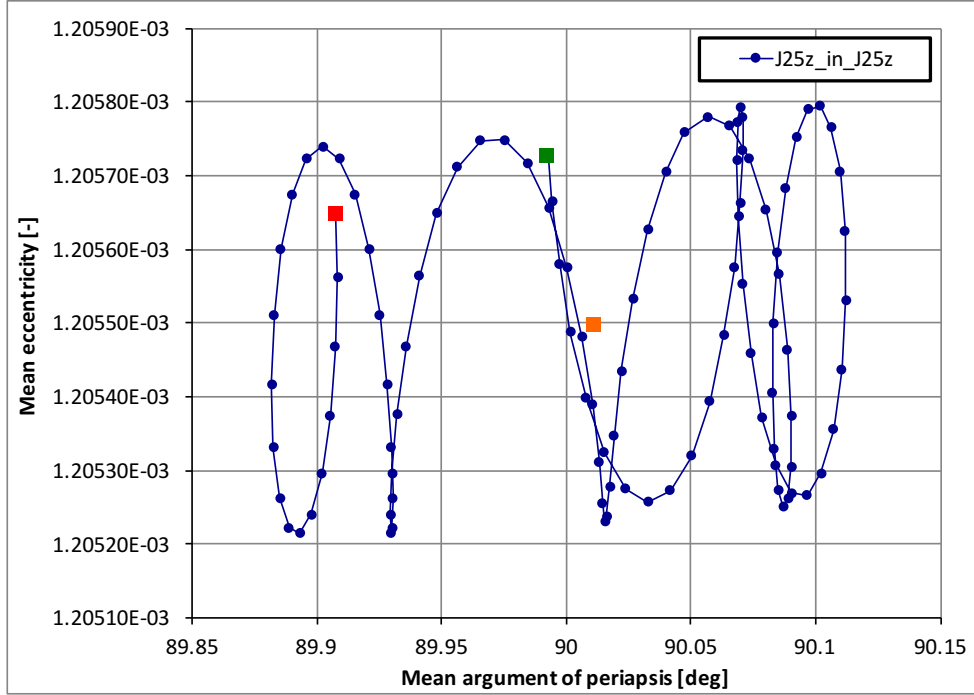


Figure 7.7: Evolution of \bar{e} and $\bar{\omega}$ found by propagating the J_{25} -optimal injection conditions in the same J_{25} zonal geopotential, for a period of two years. Green, red and orange marks depict the start, end and averaged value.

For the zonal models, it can be concluded that good long-term stability can be achieved over a period of two years by formulating the frozen orbit problem. It is observed that with increasing degree of the geopotential model, the frozen mean eccentricity seems to converge to a certain value, which for the specific case examined in this chapter lies between the values $\bar{e} = 0.00120$ and 0.00121 . This change is significant with respect to the simple J_2-J_3 and matches with the expected values in Section 4.2.

With the basis for the solutions of the numerical optimization process well established by investigating the zonal models for which analytic solutions are available, it is now time to use the method on more realistic models. The inclusion of sectorial terms in the geopotential will be the next step.

7.3 Influence of other perturbations

In this section, the effects of several perturbations on frozen orbits are investigated. The injection conditions found when optimizing for the J_{10} model in the previous section are used to propagate over a 2-year period to assess the stability of \bar{e} and $\bar{\omega}$. The stability is assessed in models that include one of the following:

- tesseral and sectorial gravity field terms
- third-body gravity from the Moon and the Sun
- radiation pressure
- atmospheric drag

In Figure 7.8, the effect of adding third-body gravity and atmospheric drag to the zonal potential complete up to degree 10 is depicted. The original evolution of \bar{e} and $\bar{\omega}$, as found in Figure 7.5, is shown in blue, and it is easily seen that the other perturbations cause a larger variation in \bar{e} and $\bar{\omega}$. Especially the third-body perturbation causes a complex pattern in the evolution of \bar{e} and $\bar{\omega}$, whereas the atmospheric drag produces a pattern that resembles the original one, yet with some more variation in both \bar{e} and $\bar{\omega}$. The effects are, however, rather insignificant when compared to the effects caused by the inclusion of tesseral & sectorial terms and radiation pressure, as becomes apparent from Figure 7.8.

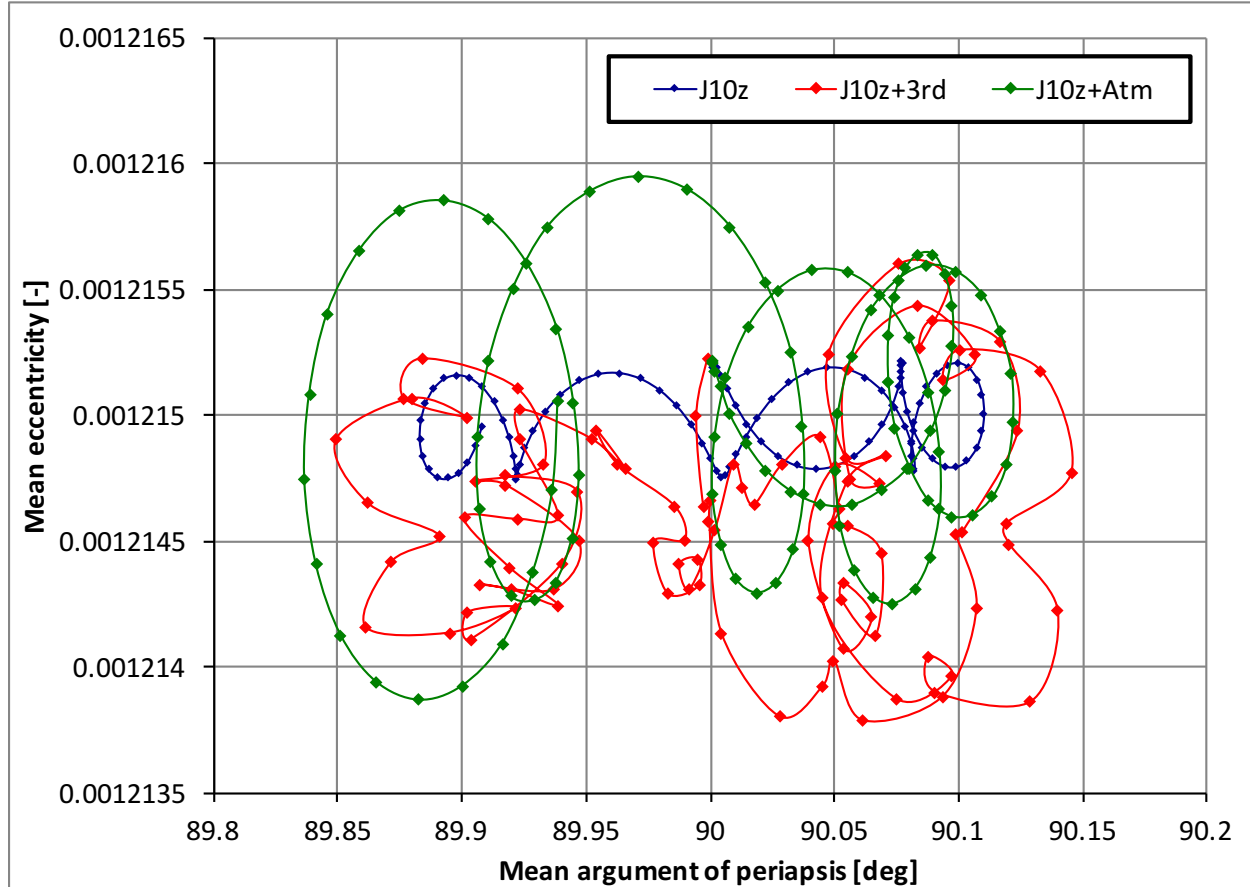


Figure 7.8: Evolution of \bar{e} and $\bar{\omega}$ as a result of numerical propagation of the injection conditions found in a J_{10} zonal model, over a period of 2 years, propagated in a J_{10} zonal model with various perturbations.

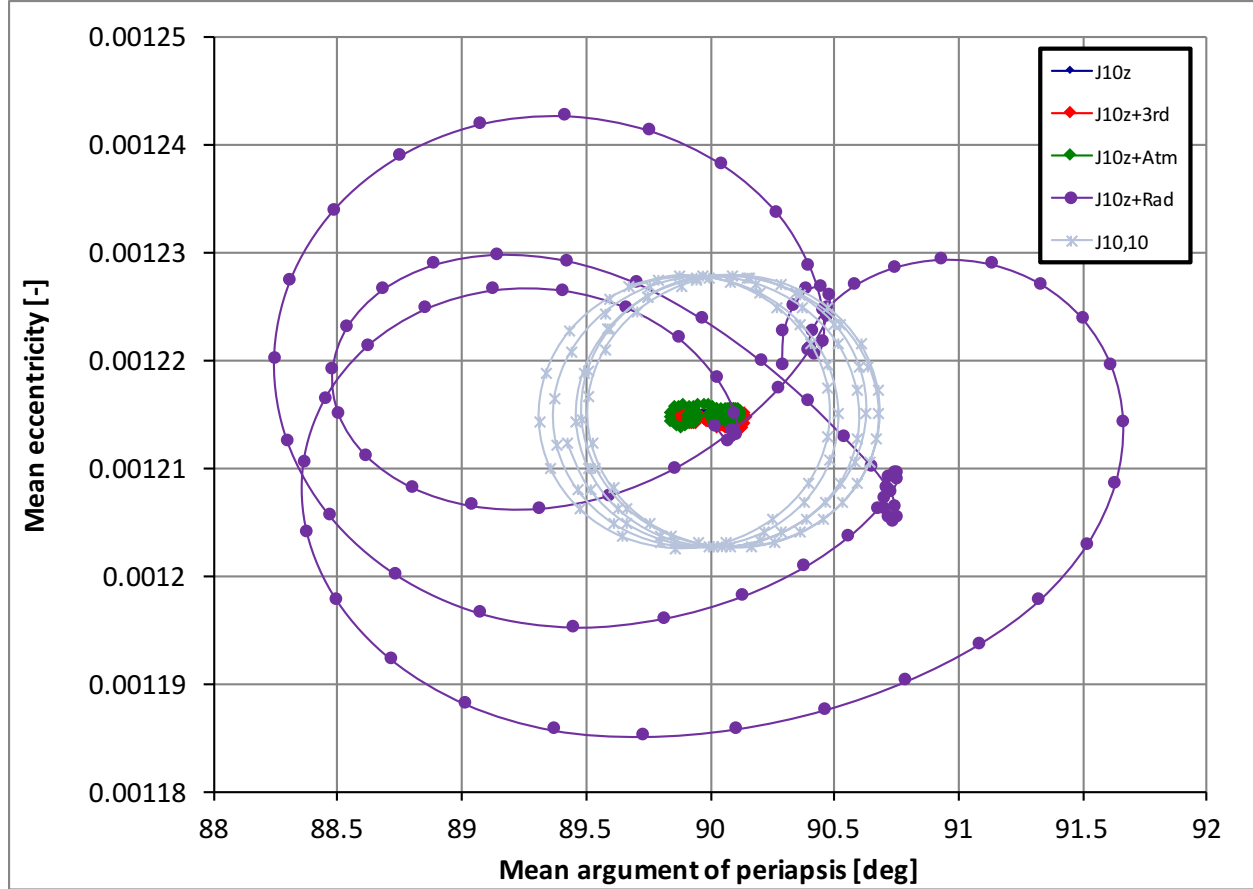


Figure 7.9: Evolution of \bar{e} and $\bar{\omega}$ as a result of numerical propagation of the injection conditions found in a J_{10} zonal model, over a period of 2 years, propagated in a J_{10} zonal model with various perturbations.

It becomes apparent from Figure 7.9 that for the mission case evaluated in this chapter, radiation pressure is the most influential perturbation. It causes the variation in mean eccentricity to reach values close to $\Delta\bar{e} = 6 \cdot 10^{-5}$, more than ten times than the variations caused by drag and third-body gravity. The variation caused by the radiation pressure decreases at some points during the simulation - which can be explained by the fact that orbit is not Sun-synchronous and therefore the angle between the orbital plane and the vector pointing towards the Sun continuously changes - this causes the variation to be more significant at certain times. The choice of a Sun-synchronous orbit (such as chosen for the ERS satellites) can thus be beneficial, provided that the fixed orientation of the orbital plane with respect to the Sun has a low secular impact on \bar{e} and $\bar{\omega}$.

Inclusion of other perturbations

In this paragraph, an attempt is made to integrate the sectorial and tesseral terms of the gravity field into the optimization problem, and to find ideal frozen conditions while taking this extra perturbation into account. Quite some research has been done on finding frozen orbit conditions in zonal geopotentials, but it is much more difficult to include sectorial and tesseral terms in an analytic fashion. However, the method described in this work is designed to work with all models that can be modeled numerically. The objective function value evolution is shown in Figure 7.10.

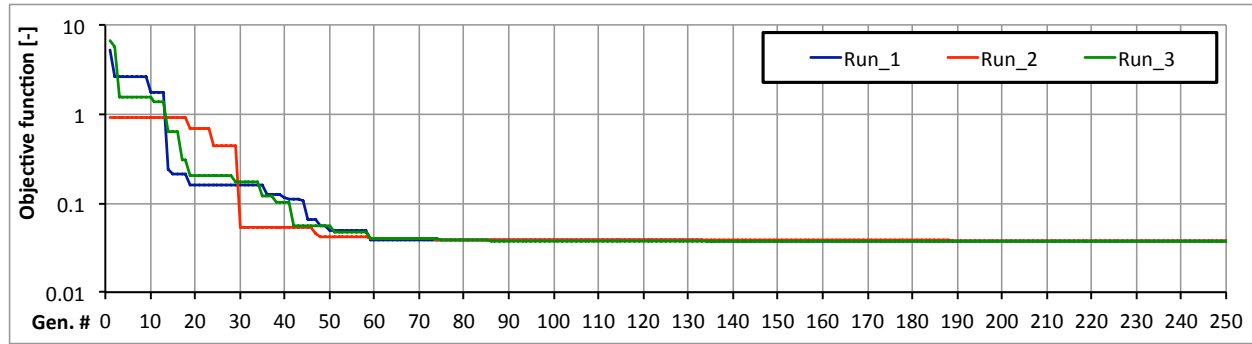


Figure 7.10: Objective function value for $J_{10,10}$ geopotential model.

Again, the convergence criteria that were specified in Section 7.1 are applied here, and from the objective function graph and the table with the results (Table 7.7) it can be verified that these three criteria apply within good margin.

J_{10,10}	Run 1	Run 2	Run 3	Resulting mean el.
F [-]	0.037530	0.037883	0.037549	
a [km]	7358.378	7358.685	7361.528	$\bar{a} = 7367.220$
e [-]	0.002820857	0.002820874	0.002819502	$\bar{e} = 0.001215123$
ω [deg]	91.88973	91.78907	91.74069	$\bar{\omega} = 90.007$

Table 7.7: Optimized injection elements and resulting mean elements in a geopotential of degree and order 10.

When comparing the optimum injection vectors found in the zonal J_{10} model with the findings in this $J_{10,10}$ model, it becomes clear that the differences in terms of optimal injection conditions are small, as is the case for the resulting mean elements. However, the objective function values have increased with a factor 8, and this observation rises the question on whether taking into account the sectorial and tesseral terms makes a difference with respect to the zonal solution. If the optimized injection vector is almost identical to the one in the simpler case, but yet the variations in \bar{e} and/or $\bar{\omega}$ have increased a tenfold ($\Delta\bar{e} = 3.5 \cdot 10^{-6}$, from Figure 7.11), then there is perhaps no benefit to include these the sectorial and zonal terms, and the larger variations have to be accepted regardless. However, the variations observed in Figure 7.11 are smaller than those observed when the injection parameters found in a zonal J_{10} model were propagated in a $J_{10,10}$ model (Figure 7.9), so there is some improvement possible.

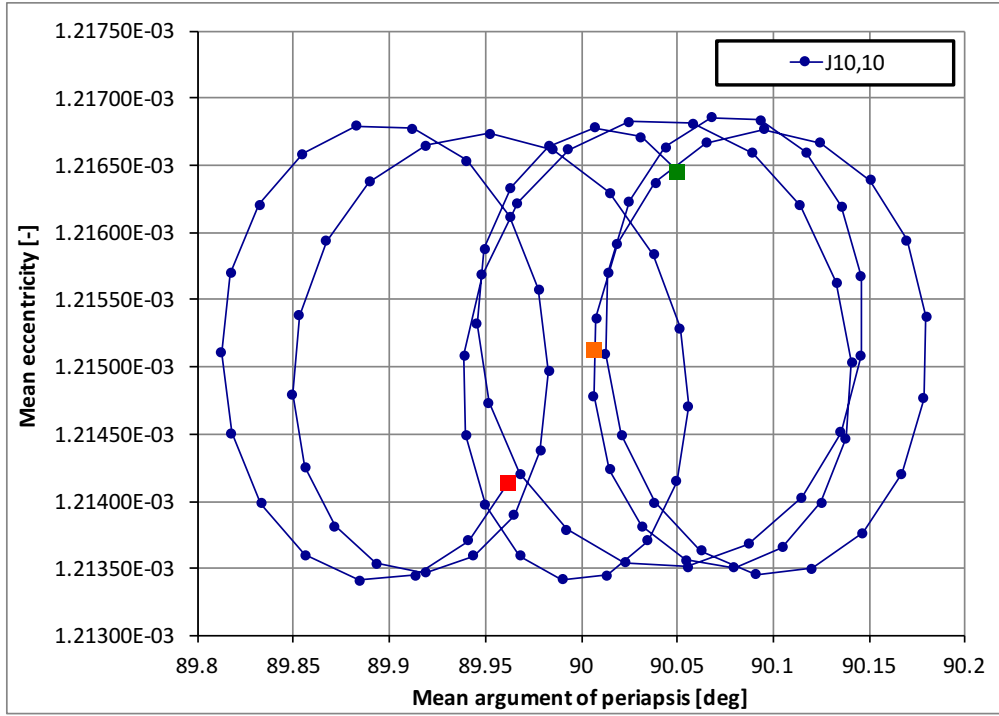


Figure 7.11: Evolution of \bar{e} and $\bar{\omega}$ found by propagating the $J_{10,10}$ -optimal injection conditions in the same $J_{10,10}$ geopotential, for a period of two years. Green, red and orange marks depict the start, end and averaged value, and the time between two marks is 1 week.

Optimization has also been done in J_{10} zonal models with radiation pressure / third-body gravity / atmospheric drag, and the results of these optimization runs in Table 7.8.

Model >	J_{10}	$J_{10} + \text{drag}$	$J_{10} + \text{radiation}$	$J_{10} + 3^{\text{rd}}$ body	$J_{10,10}$
F [-]	0.004679	0.005764	0.017050	0.027620	0.037530
Inj. a	7358.685	7374.506	7397.820	7376.126	7367.220
Inj. e	0.002820874	0.002810149	0.00279559	0.002808188	0.002820857
Inj. ω	89.97526	89.99841	90.71960	90.03010	91.88973
Res. \bar{a}	7367.100	7383.343	7406.658	7384.988	7361.528
Res. \bar{e}	0.001214977	0.001210768	0.001204747	0.001210001	0.001215123
Res. $\bar{\omega}$	90.011	90.010	89.95048606	90.00746664	90.007

Table 7.8: Optimized injection vectors in the J_{10} zonal model with various perturbations included.

From Table 7.8 it becomes clear that variations in both injection and mean parameters are limited to variations of at most $\pm 2\%$ with respect to the zonal case. It is therefore stated that for an integration period of 10 days, it is not possible to further optimize the frozen orbit solution by taking into account other perturbation models. Perhaps a longer integration time will yield better results, but at the expense of computational cost. However, for finding the most optimal scenario in the next section, all of these perturbations will be taken into account.

7.4 Complete set of perturbations

In this final section of this chapter, frozen orbit conditions are determined and tested for stability in the most complete model treated in this work. Gravity field model coefficients are taken into account up to degree and order 25, as well as atmospheric drag, third-body gravity of the Moon and the Sun and radiation pressure. Because of the long computation time required to solve this optimization problem, only two runs have been performed, and the results of those runs are shown in Figure 7.12.

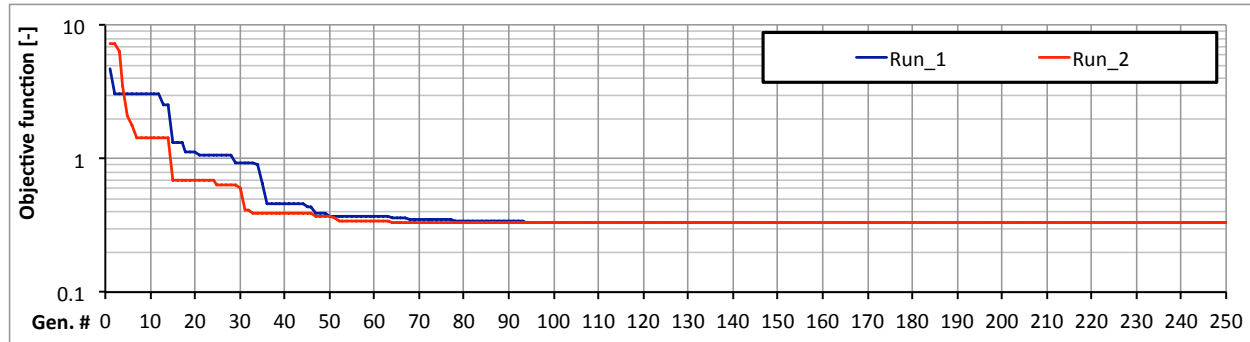


Figure 7.12: Objective function value for $J_{25,25}$ geopotential model with drag, radiation pressure and third-body gravity.

As for all the other optimization runs in this chapter, the results displayed in both Figure 7.12 and table 7.9 are conform with the convergence criteria that were discussed at the beginning of this chapter.

$J_{25,25}$	+ all	Run 1	Run 2	Resulting mean el.
F	[\cdot]	0.330665	0.329800	
a	[km]	7398.081	7398.076	$\bar{a} = 7406.829$
e	[\cdot]	0.002777762	0.002776902	$\bar{e} = 0.001195367$
ω	[deg]	92.60098	92.75148	$\bar{\omega} = 89.946$

Table 7.9: Optimized initial conditions in a geopotential complete up to degree and order 25 and including drag, radiation pressure and third-body gravity.

The long-term evolution of \bar{e} and $\bar{\omega}$, which is displayed in Figure 7.13, is obviously dominated by the effects of solar radiation pressure, as the pattern resembles the pattern that was found in Figure 7.9. The variation in \bar{e} and $\bar{\omega}$ has not changed with respect to the result in Figure 7.9, which again leads to believe that the zonal solution is good enough and that there is no other option to decrease the effect of the radiation pressure apart from adapting the design of the satellite or enforcing a Sun-synchronous orbit with the proper orientation with respect to the Sun. However, the effect of injection inaccuracies in e and ω leads to much more significant variations than those caused by radiation pressure, as will be discussed in the next paragraph.

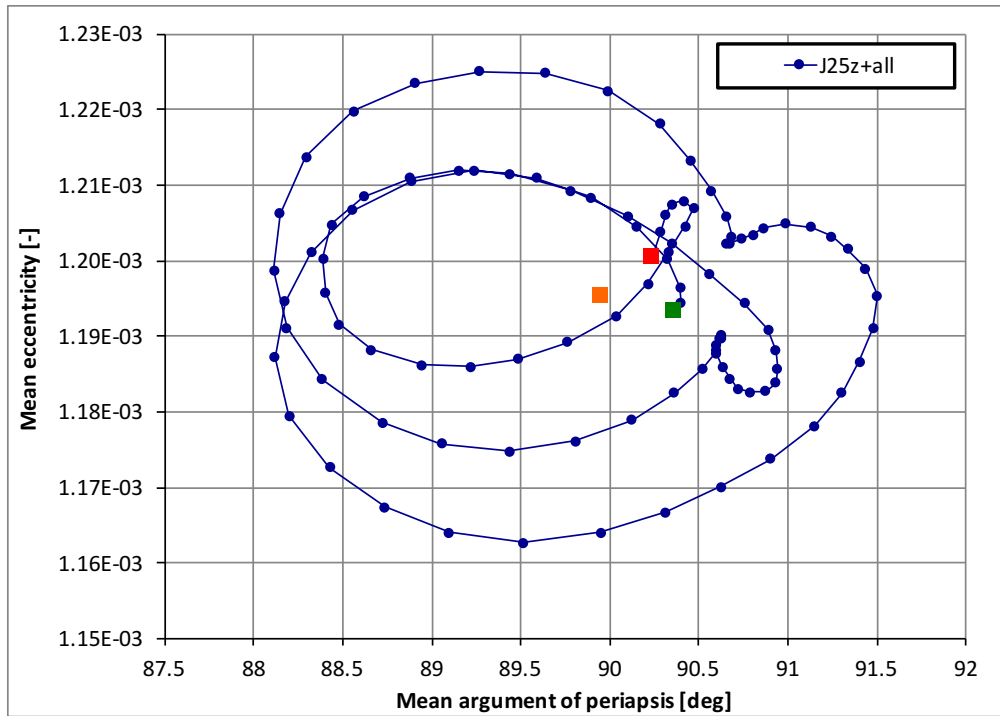


Figure 7.13: Evolution of \bar{e} and $\bar{\omega}$ as a result of numerical propagation of the injection conditions found in a $J_{25,25}$ geopotential including drag, radiation pressure and third-body gravity, propagated over a period of 2 years. Green, red and orange marks depict the start, end and averaged value, and the time between two marks is 1 week.

Injection inaccuracies

Earlier in this chapter, a set of convergence criteria for the optimization method were conceived, which were based on 1σ values of a modern Soyuz launch vehicle. The injection vectors found in this chapter were defined to a much higher precision than what would be achievable by probably any known launch vehicle, and because of this the satellite itself will need to carry out maneuvers to insert itself in the designed frozen orbit. However, the effects of injection errors on the long-term behavior of \bar{e} and $\bar{\omega}$ can be insightful, as with such information it is possible to estimate the expected errors that have to be compensated for by maneuvering. Figures 7.14 to 7.16 show the evolution of \bar{e} and $\bar{\omega}$ when the injection vector found in Table 7.9 is subjected to the inaccuracies listed in Table 7.3¹. The careful geometry required for a frozen orbit is underlined in these figures, at least in terms of the eccentricity and the argument of periapsis - the resulting errors for an inaccuracy in the injection semi-major axis is small, as the behavior of \bar{e} and $\bar{\omega}$ is nearly identical with respect to the original injection vector. Especially the eccentricity at injection requires great precision, as a 1σ inaccuracy gives rise to large variations in \bar{e} and $\bar{\omega}$, as shown in Figure 7.15.

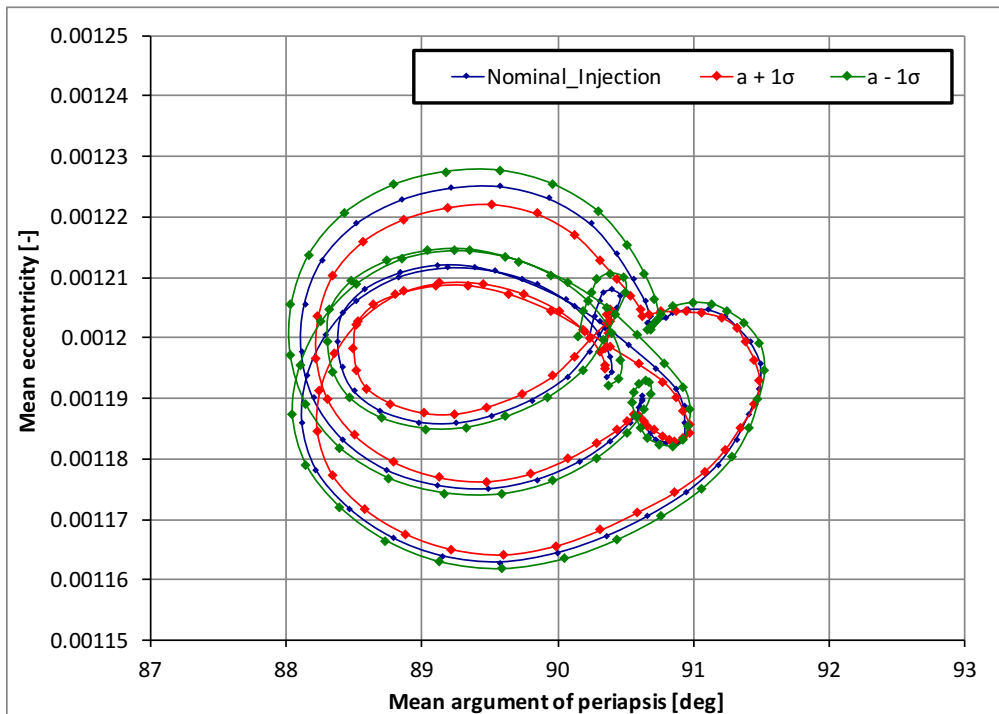


Figure 7.14: Evolution of \bar{e} and $\bar{\omega}$ over a period of two years, subject to a 1σ inaccuracy in the osculating semi-major axis at injection.

¹The inaccuracy in ω is hard to define for near-circular orbits and has been assumed to be ± 20 degrees.

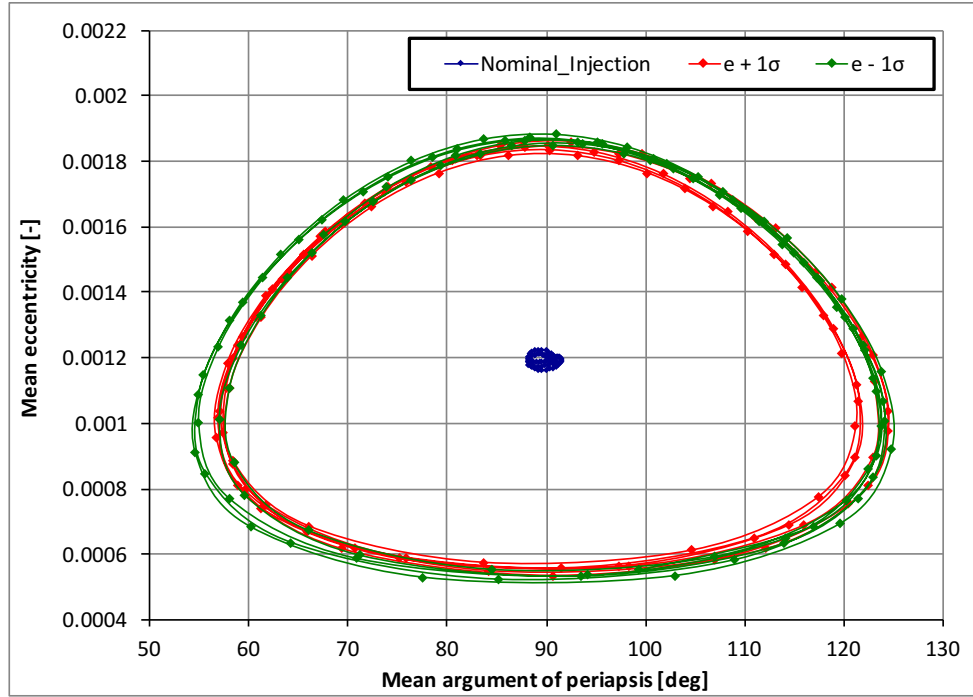


Figure 7.15: Evolution of \bar{e} and $\bar{\omega}$ over a period of two years, subject to a 1σ inaccuracy in the osculating eccentricity at injection.

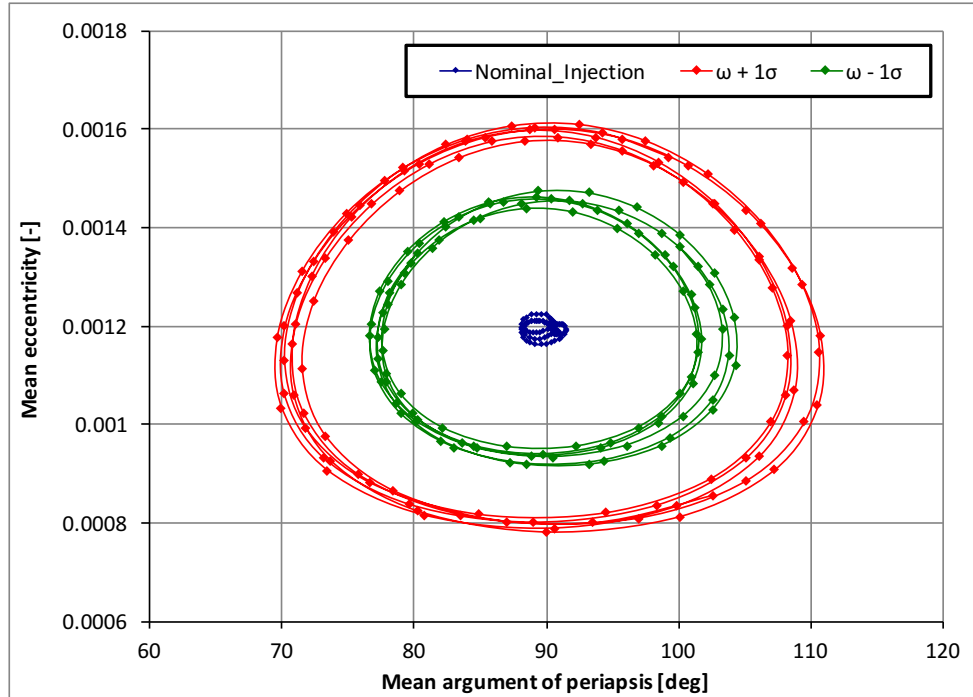


Figure 7.16: Evolution of \bar{e} and $\bar{\omega}$ over a period of two years, subject to an assumed 1σ value of 20 degrees inaccuracy in the osculating argument of periapsis at injection.

Satellite altitude

The most important design criterion for choosing a frozen orbit is the fact that by doing so the altitude of the satellite will be constant as a function of location, eg. during consecutive passes over a certain region, the altitude has not varied under influence of perturbations. This important feature can indeed be verified (in terms of latitude) for the injection conditions obtained in this section. The altitude (above the WGS84 reference ellipsoid) found by propagating the injection vector is shown in Figure 7.17. The altitude profile in Figure 7.17 has variations of roughly 400 meters around the equator, but data for different longitudes is plotted here - to actually assess the variations in altitude as function of both, these variations have to be assessed at cross-over locations.

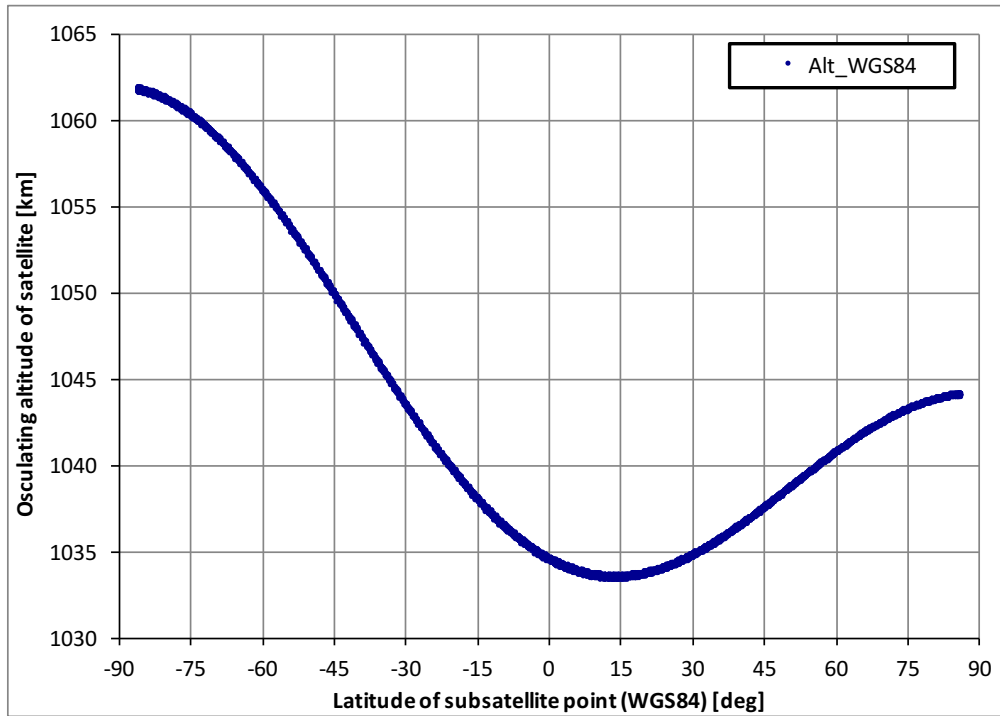


Figure 7.17: Osculating altitude of the hypothetical satellite from Section 7.4 as a function of latitude for a period of two days.

Conclusions and recommendations

This work ends with this final chapter. The aim of this last chapter is to present conclusions that can be drawn from this research, and to provide recommendations that may aid in further research on the topic of this work.

8.1 Conclusions

The focus of this work lies on the design of frozen orbits in a numerical fashion, so the limitations of the analytical solution in terms of zonal gravity field coefficients could be overcome, and on the subsequent investigation of the orbits that are designed in this way. In the introduction, this focus was cast into the form of three research goals, which are repeated here:

- Providing an analysis on the actual behavior of satellites that fly in a frozen orbit.
- Setting up a numerical method to find frozen orbit conditions in a complex dynamics model including **tesseral** gravitational potentials, **third-body** attraction, aerodynamic **drag** and solar **radiation pressure**.
- Subsequent evaluation of the method by simulating the behavior of satellites inserted into an orbit found by this numerical method.

With the methodology described in Chapter 5 and the subsequent verification of that method in both Chapters 6 and 7 the second research goal has been met. With this numerical method, subroutines could be used that have aided in meeting the first research goal in Chapter 4. The third and final goal is met in Chapter 7. The final conclusions to be drawn have been split up into two parts, where the first part focuses on the conclusions that can be drawn directly from Chapter 7:

- The numerical method for finding frozen orbits has been successful in identifying these orbits for the hypothetical satellite mission described in Section 7.1 for several orbital dynamics models. The evolution of the mean eccentricity and mean argument of periapsis over the two-year propagation does not diverge in any of the cases, and a stable altitude profile as function of latitude is achieved.
- For the ERS-2 type satellite considered in Section 7.1, it is found that radiation pressure is the most influential perturbation, causing eccentricity variations of up to $\pm 3\%$ of the averaged mean value. The other perturbations induce less significant secular effects.

- Taking into account other perturbations than zonal spherical harmonics terms during the optimization process does not lead to significant improvements in the variations in the mean argument of periapsis and the mean eccentricity. The analytical solution for higher order zonal terms is sufficient - corrective maneuvers will be necessary anyway.
- Maneuvering strategies after launch are necessary to achieve a frozen orbit, as injection inaccuracies are too significant to achieve the careful frozen geometry directly after launch.

Conclusions which are not directly related to the results of this work, but more to the methodology and the behavior of satellites that actually fly in frozen orbits, the following conclusions can be drawn:

- The combination of Eckstein-Ustinov transformation and numerical averaging is able to reconstruct mean elements orbital elements that match the design values of well-known missions to good extent.
- As expected from missions that fly in a frozen orbit, the mean elements of TOPEX/Poseidon and ERS-2 show little variation over time. Maneuvers clearly show as sudden jumps in the behavior of the mean elements.

8.2 Recommendations

Like all academic research efforts, this work has room for improvements, room for possible follow-ups and contains aspects that could have been approached in a different way. A list of recommendations regarding these points, sorted by the sub-topics of this work, are listed below.

Trajectory simulation

In this work, extensive use is made of the variable step size Runge-Kutta Dormand Prince integrator (RK8(7)), as it was found that it yielded the best speed/accuracy ratio of the available integration methods. Speed is an important factor in this work - the objective function evaluation has to be repeated many times, so every second that can be gained here will ‘optimize the optimization’. For sheer speed, multi-step methods should have been considered for this work. Some of them are quicker than the RK8(7) method, but on the downside these methods require multiple start-up points, and as such it becomes more difficult to readily define the injection parameters. A combination of RK8(7) and a multi-step method, using the single-step method to first solve for the first few points needed for multi-step integration, could reduce computational load.

Another recommendation can be found in the used models. For the simulations in this work, vital characteristics such as satellite mass, attitude and frontal surface area, are estimated, and their values remain constant throughout the simulation. This is of course quite a limited representation of the real world, and especially the influence of drag and solar radiation pressure is unpredictable. This means that long-term propagation of the injection conditions to investigate the stability can be insightful, but by all means will the actual trajectory diverge from the propagation as time progresses.

Optimization method and objective function

It is noted that the optimization method in this work (DE) is very suitable for astrodynamics problems, but perhaps the method is overkill for a problem with three decision vectors. While it is true that using this advanced method allows for the use of more complex problems (for example,

leaving the inclination and right ascension of the ascending node free during the optimization as well), it is not necessarily the most efficient at solving the three-dimensional problem in Chapter 7. The use of a gradient-based search method in combination with a global optimization method may very well lead to quicker convergence and could be researched to improve the efficiency of the developed software.

The options of enforcing a Sun-synchronous orbit or a repeating ground-track orbit are not yet part of this work. Perhaps an efficient method is to include this as a secondary (and tertiary) objective, transforming this single-objective optimization problem into a multi-objective problem. It is noted that a third objective may be added to minimize the offset between the mean semi-major axis and reference value, as this parameter governs the orbital period which is therefore a key parameter for designing a ground track repeat orbit.

The objective function that is used in this work is only used for minimizing the variations in \bar{e} and $\bar{\omega}$ at this point. However, by manipulating the weight factors it is possible to include other mean elements, such as \bar{a} or \bar{i} . The effects of changing these weight factors has not thoroughly been investigated in this work, apart from some tuning for performance reasons.

Eckstein-Ustinov transformation

In the used form of the Eckstein-Ustinov theory, simplifications have taken place in which the mean eccentricity of the final orbit is assumed to be in the order of J_2 , so that it can safely be assumed that $e^2 \approx 0$. Such an assumption is justified for frozen orbits with a high inclination, as apparent from Figure 4.1. However, from the same figure it is easily seen that for frozen orbits near the critical inclination, this assumption is no longer valid, and this may cause the reconstruction of mean elements to fail. A recommendation for future research is to further refine the transformation to mean elements and to try and make it free of such limiting assumptions. This can be done by using the complete method described by [39] (including Kaula's potential to transform from osculating to mean elements), but doing so will result in a large penalty in terms of computational effort.

Practicality

The method described in this work provides an osculating injection state vector, of which all of the parameters are computed to four or more significant digits. However, no launcher is able to inject a satellite into its orbit with such accuracy (Section 7.4), so a maneuvering strategy is required at the beginning of the mission. Such a strategy has not been investigated in this work, but this topic may be worth investigating in the future.

In addition, it is noted the method for finding frozen orbits described in this work is computationally expensive: finding frozen conditions in a simple J_2-J_3 model took 5 hours on a 2009 Macbook equipped with a Core2Duo processor at 2.26 GHz & 8 GB RAM. More realistic models required much more time, as especially the evaluation of the spherical harmonics functions becomes tedious for accurate geopotential models. The final run in Section 7.4 took three full days to complete.

Bibliography

- [1] M. Capderou. *Satellites: Orbits and Missions*. Springer, 2005.
- [2] V.A. Chobotov. *Orbital Mechanics 3rd Edition*. AIAA Education, 2002.
- [3] K.F. Wakker. *Astrodynamic-II course notes AE4-874II*. Faculty of Aerospace Engineering TU Delft, 2010.
- [4] E. Cutting, J.C. Frautnick, and G.H. Born. Orbit analysis for Seasat-A. *Journal of the Astronautical Sciences*, 26:315–342, 1978.
- [5] R. Scharroo. *A decade of ERS satellite orbits and altimetry*. PhD thesis, Delft University of Technology, Faculty of Aerospace Engineering, 2002.
- [6] NODC/NOAA. TOPEX/Poseidon Mission Overview. <https://directory.eoportal.org/web/eoportal/satellite-missions/t/topex-poseidon>, 2014. [Online; accessed 10-Mar-2015].
- [7] K. Kiedron and R. Cook. Frozen orbits in the J₂ + J₃ problem. In *AAS/AIAA Astrodynamics Conference*, pages 1273–1289. American Astronomical Society, 1992.
- [8] G.W. Rosborough and C.A. Ocampo. Influence of higher degree zonals on the frozen orbit geometry. In *AAS/AIAA Astrodynamics Conference*, pages 1291–1304. American Astronomical Society, 1992.
- [9] Earth Observation Portal. Seasat (Seafaring Satellite) mission. <https://directory.eoportal.org/web/eoportal/satellite-missions/s/seasat>, 2013. [Online; accessed 10-Sep-2015].
- [10] Earth Observation Portal. Earth Reconnaissance Satellites (ERS). <https://directory.eoportal.org/web/eoportal/satellite-missions/e/ERS-1>, 2013. [Online; accessed 10-Sep-2015].
- [11] Earth Observation Portal. TOPEX/Poseidon. <https://directory.eoportal.org/web/eoportal/satellite-missions/t/topex-poseidon>, 2013. [Online; accessed 10-Sep-2015].
- [12] Artist impression of Seasat in orbit. <http://eospso.nasa.gov/missions/seasat-1>. [Online; accessed 10-Sep-2015].

- [13] C. A. Jablonski. Application of semi-analytic satellite theory to maneuver planning. Master's thesis, Massachusetts Institute of Technology, 1991.
- [14] Artist impression of ERS-2 in orbit. http://www.redorbit.com/news/space/1853256/ers2_satellite_celebrates_15th_anniversary/. [Online; accessed 10-Sep-2015].
- [15] R. Scharroo and P.N.A.M. Visser. Precise orbit determination and gravity field improvement for the ERS satellites. *Journal of Geophysical Research*, 103:8113–8127, 1998.
- [16] Artist impression of TOPEX/Poseidon in orbit. <http://www7320.nrlssc.navy.mil/altimetry/>. [Online; accessed 10-Sep-2015].
- [17] B.D. Tapley et al. Precise orbit determination for TOPEX/Poseidon. *Journal of Geophysical Research*, 99 C12:24383–24404, 1994.
- [18] J. Guinn et al. TOPEX/Poseidon precise orbit determination using combined GPS, SLR and DORIS. Technical report, Jet Propulsion Laboratory, 1995.
- [19] A. Mazzoleni, C. D. Urgoiti, F. G. Meruelo, M. L Cerrón, P. Pisabarro, and F. Pirondini. Deimos-1 mid-life local time control strategy: analysis and operational implementation. In *International Symposium on Space Flight Dynamics Symposium*, 2015.
- [20] M. L. Cerrón, F. G. Meruelo, C. D. Urgoiti, A. Mazzoleni, F. Pirondini, and M. B. Mora. Deimos-2 initial orbit acquisition operations. In *International Symposium on Space Flight Dynamics Symposium*, 2015.
- [21] M. A. Martín Serrano, M. Carania, J. Sánchez, A. Vasconcelos, D. Kuijper, and X. Marc. Sentinel-1A flight dynamics LEOP operational experience. In *International Symposium on Space Flight Dynamics Symposium*, 2015.
- [22] M. Beckman and R. Lamb. Stationkeeping for the Lunar Reconnaissance Orbiter. In *International Symposium on Space Flight Dynamics Symposium*, 2007.
- [23] K.F. Wakker. *Astrodynamic-I course notes AE4-874I*. Faculty of Aerospace Engineering TU Delft, 2010.
- [24] H. Curtis. *Orbital Mechanics for Engineering Students*. Elsevier, 2013.
- [25] O. Montenbruck and E.K.A. Gill. *Satellite Orbits*. Springer Science & Business Media, 2000.
- [26] J. M. Picone, A. E. Hedin, and D. P. Drob. NRLMSISE-00 empirical model of the atmosphere: statistical comparisons and scientific issues. *Journal of Geophysical Research*, 2001.
- [27] Marshall Space Flight Center Solar Physics. Solar cycle prediction. <http://solarscience.msfc.nasa.gov/predict.shtml>, 2015. [Online; accessed 29-Sep-2015].
- [28] D. A. Vallado. *Fundamentals of Astrodynamics and Applications*. Kluwer Academic Publishers, 2001.
- [29] M. Lata, J. F. San-Juan, and L. M. López-Ochoa. Precise analytical computation of frozen-eccentricity Low Earth Orbits in a tesseral potential. *Mathematical Problems in Engineering*, 2013.

- [30] W.M. Kaula. *Theory of Satellite Geodesy*. Courier Dover Publications, 2000.
- [31] M. Rosengren. Improved technique for passive eccentricity control. In *Proceedings of the AAS/NASA International Symposium*, pages 49–58. American Astronomical Society, 1989.
- [32] ERS and Envisat Precise Orbit Determination. <http://www.deos.tudelft.nl/ers/precorbs/>. [Online; accessed 1-Sep-2015].
- [33] Description of LCA orbit series in SP3C format. <ftp://cddis.gsfc.nasa.gov/doris/products/orbits/lca/lca.sp3.readme>. [Online; accessed 1-Sep-2015].
- [34] H. Klinkrad. *Space Debris Models and Risk Analysis*. Springer-Verlag, 2006.
- [35] O. Montenbruck. Numerical integration methods for orbital motion. *Celestial Mechanism and Dynamical Astronomy*, 53:59–69, 1992.
- [36] E. Kreyszig. *Advanced Engineering Mathematics*. Wiley International, 2006.
- [37] M.R. Delgado. Modeling the Space Environment. <http://ocw.upm.es/ingenieria-aeroespacial/modeling-the-space-environment/lecture-notes>, 2014. [Online; accessed 1-Sep-2015].
- [38] S. Spiridonova, M. Kirschner, and U. Hugentobler. Precise mean orbital elements determination for LEO monitoring and maintenance. *International Symposium on Space Flight Dynamics*, 2014.
- [39] S. Spiridonova. Conversion of osculating orbital elements into mean orbital elements for orbit monitoring and precise maneuver planning. Master's thesis, Technical University Munich, 2012.
- [40] M.C. Eckstein and H. Hechler. *A reliable derivation of the perturbations due to any zonal and tesseral harmonics of the geopotential for nearly-circular satellite orbits*. ESRO/ELDO, 1970.
- [41] Z. B. Zabinsky. *Stochastic Adaptive Search for Global Optimization*. Springer Science and Business Media LLC, 2003.
- [42] R. Storn and K. Price. Differential evolution - a simple and efficient adaptive scheme for global optimization over continuous spaces. Technical report, International Computer Science Institute, 1995.
- [43] T. Weise. *Global Optimization Algorithms, Theory and Application*. No Publisher, 2006.
- [44] TU Delft Astrodynamics Toolbox (Tudat) website. <http://tudat.tudelft.nl/projects/tudat/wiki>. [Online; accessed 1-Sep-2015].
- [45] Parallel global multi-objective optimization toolbox website. <https://esa.github.io/pagmo/>. [Online; accessed 27-Oct-2015].
- [46] D. Izzo. PyGMO and PyKEP: Open source tools for massively parallel optimization in astrodynamics (the case of interplanetary trajectory optimization). Technical report, ESA/ESTEC, 2011.

- [47] R. Storn. On the usage of Differential Evolution for function optimization. In *1996 Biennial Converence of the North American Fuzzy Information Processing Society (NAFIPS)*, 1996.
- [48] Edouard Perez. Soyuz from the Guiana Space Centre - User's Manual. Technical report, Arianespace, 1995.